VILNIUS UNIVERSITY

Tadas Malinauskas

INVESTIGATION OF CARRIER DYNAMICS IN WIDE BANDGAP SEMICONDUCTORS BY LIGHT-INDUCED TRANSIENT GRATING TECHNIQUE

Doctoral dissertation

Physical Sciences, Physics (02 P), Semiconductor Physics (P 265)

Vilnius, 2009

Dissertation was prepared at the Institute Applied Research, Vilnius University in 2005 – 2009.

Scientific Supervisor:

Prof. Dr. Habil. Kęstutis Jarašiūnas (Vilnius University, Physical Sciences, Physics – 02P, Semiconductor Physics (P 265)).

VILNIAUS UNIVERSITETAS

Tadas Malinauskas

KRŪVININKŲ DINAMIKOS TYRIMAS PLAČIATARPIUOSE PUSLAIDININKIUOSE ŠVIESA INDUKUOTŲ DINAMINIŲ GARDELIŲ METODU

Daktaro disertacija

Fiziniai mokslai, fizika (02P), puslaidininkių fizika (P 265)

Vilnius, 2009

Disertacija rengta 2005 – 2009 metais Vilniaus universitete, Taikomųjų mokslų institute.

Mokslinis vadovas:

prof. habil. dr. Kęstutis Jarašiūnas (Vilniaus universitetas, fiziniai mokslai, fizika, – 02P, puslaidininkių fizika (P 265)).

Reziumė

III grupės nitridai bei deimantai tai platų draustinės energijos tarpą turintys puslaidininkiai, pasižymintys unikaliomis medžiagos savybėmis ir turintys didelį potencialą aukštų temperatūrų, didelių galių, opto/elektroniniams taikymams. Todėl šių medžiagų elektrinės bei optinės savybės pastaruoju metu yra intensyviai tiriamos. Šviesa indukuotų dinaminių gardelių (ŠIDG) metodas labai tinka tyrinėti krūvininkų dinamiką, kuri yra nulemta fundamentinių bei defektinių medžiagos savybių.

Pagrindiniai darbo tikslai buvo gauti naujų žinių apie krūvininkų dinamiką plačiatarpiuose puslaidininkiuose (GaN, InGaN bei deimantuose) naudojat bei plėtojant šviesa indukuotų gardelių metodiką. Ištirti didelio nepusiausvirųjų krūvininkų tankio rekombinacijos ir difuzijos ypatumus skirtingo defektiškumo GaN, InGaN sluoksniuose bei sintetiniuose deimantuose. Skaitmeniškai modeliuojant krūvininkų dinamiką nustatyti dominuojančius krūvininkų rekombinacijos mechanizmus bei krūvininkų gyvavimo trukmes, difuzijos koeficientus ir nuotolius.

Darbe pristatoma nauja ŠIDG eksperimento schema su holografiniu pluoštelio dalikliu, leidžianti supaprastinti eksperimentą. Ši schema taip pat įgalino heterodininį difrakcijos signalo detektavimą. Parodoma, kad fazės skirtumas tarp signalo ir foninės šviesos gali būti kontroliuojamas keičiant holografinio daliklio padėtį išilgai jo gardelės vektoriaus krypties.

Ištyrus didelį kiekį GaN sluoksnių, užaugintų skirtingomis technologijomis bei pasižyminčiu skirtingu dislokacijų tankiu, buvo nustatyti dominuojantys krūvininkų rekombinacijos mechanizmai. Parodoma, kad dislokacijų sąlygota nespindulinė rekombinacija dominuoja bandiniuose su dislokacijų tankiu didesniu nei 10^8 cm^{-2}, esant mažesniems dislokacijų tankiams krūvininkų gyvavimo trukmę lemia bimolekulinė rekombinacija. Atlikę ŠIDG tyrimus GaN sluoksniuose žemose temperatūrose bei krūvininkų dinamikos modeliavimą tiesiogiai nustatėme bimolekulinės rekombinacijos koeficientą plačiame temperatūrų intervale T = 9–300 K.

Eksperimentiškai nustatytas žymus (~3 kartus) krūvininkų difuzijos koeficiento padidėjimas didinant nepusiausvirųjų krūvininkų tankį GaN. Naudojant krūvininkų netiesinės dinamikos modeliavimą buvo patvirtinta, kad difuzijos koeficiento didėjimas yra sukeltas Fermi slėgio išsigimusioje krūvininkų plazmoje. Modelis buvo patvirtintas difuzijos koeficiento matavimais žemose temperatūroje.

Darbe parodyta, kad ŠIDG ir fotoliuminescencijos kinetikos storuose ir ilgą krūvininkų rekombinacijos trukmę turinčiuose GaN sluoksniuose yra skirtingos. Fotoliuminescencijos kinetikų pagreitėjimą lemia krūvininkų difuzijos į gylį nulemtas krūvininkų tankio mažėjimas. Difuzija į gylį neįtakoja ŠIDG kinetikų, todėl jos tiksliau parodo krūvininkų gyvavimo trukmę ir yra lengviau interpretuojamos.

ŠIDG tyrimai InGaN sluoksniuose parodė, kad In segregacija lokalizuoja krūvininkus taip mažindama jų difuzijos koeficientą, bei ilgindama krūvininkų rekombinacijos trukmę. Parodoma, kad InGaN kvantinėse duobėse bimolekulinė krūvininkų rekombinacija yra dominuojantis mechanizmas, o Ožė rekombinacija tirtame temperatūrų (9–300 K) ruože nėra stebima.

Pirmą kartą optiniu būdu nustatytos krūvininkų difuzijos koeficiento vertės sintetiniuose deimantuose. Krūvininkų rekombinacijos trukmių bei azoto priemaišų kiekio koreliacija parodė, kad su azotu susietos priemaišos yra pagrindiniai rekombinacijos centrai. Nustatyta, kad kambario temperatūroje deimanto monokristalams būdinga krūvininkų difuzijos koeficiento vertė yra $D_a = 9{,}7 \pm 0{,}5\ \mathrm{cm}^2/\mathrm{s}$.

Table of content

Introduction

III-nitrides (specially GaN), diamonds are extremely promising wide band gap semiconductor materials for optoelectronics and high temperature, high power electronics. Actually, GaN is likely the most important semiconductor since silicon. However, achievement of its full potential is still limited by a dramatic lack of suitable GaN bulk single crystals. Since there is no GaN bulk single crystal commercially available, the whole technological development of GaN based devices relies on heteroepitaxy.

Most of the current device structures are grown on sapphire or 6H-SiC. However, since their lattice parameters and thermal expansion coefficients are not well matched to GaN, the epitaxial growth generates huge densities of defects, with threading dislocations (TDs) being the most prevalent (10^9 to $10^{11}cm^{-2}$). Actually this large density of TDs in GaN drastically limits the performances and operating lifetime of nitride based devices. Therefore, there is currently a tremendous technological effort to reduce these defects.

Worldwide initiatives of technologically leading countries is focused on further development of III-nitride materials. Wide Bandgap Semiconductor Technology Initiative (WBSTI) program of the DARPA (USA), European technological centers (DENIS, EURONIM, ISCE-MOCVD) was aimed to achieving advances in bulk and epitaxial material quality, and by tying these to device performance, to developing low dislocation density gallium nitride substrates. The sophisticated buffer layers (LT-GaN, AlN, SL-AlGaN, SiO, etc), epitaxial lateral overgrowth (ELO, 2S-ELO, μ-ELO, and nano-ELO), modified MOCVD growth methods (PECVD, MEMOCVD) are introduced in minimize threading dislocation density (TDD) during MOCVD growth of GaN layers. While the reduction of TDD in the hydride vapour phase epitaxy (HVPE), which features high growth rate of ~50 μm/h, is achieved by increasing layer thickness up to several hundred of micrometers.

The InGaN/GaN system is used for current commercial LEDs and LDs for blue and UV spectral ranges. Nevertheless, the continuous optimization of

devices structure (well/barrier thickness, optimal doping, elimination of piezoelectric fields by growth on non-polar substrates) is taking place. Moreover, in the recent time the huge interest of GaN scientific community is focused on high power LED efficiency droop problem. The several controversial hypotheses are proposed, such as Auger recombination, over-barrier diffusion, filling of the electronic states.

The defect-free diamond is known to exhibit the largest values of heat conductivity and carrier mobility of all the wide-bandgap semiconductors. This makes the material attractive for production of high power devices, ultraviolet and ionising radiation detectors that could operate under extreme environmental conditions. However, the development of diamond electronics has been hampered by several problems, such as a lack of shallow dopants, heteroepitaxy for large single crystals, low crystal quality of synthetic diamonds. Synthetic diamonds has been for the past 50 years produced by high-pressure high-temperature (HPHT) and more recently by chemical vapor deposition (CVD). The deposition technique of high quality homoepitaxial diamond is not well established and it suffers from very slow deposition rate, inclusion of impurities (mainly nitrogen and silicon), etc. Thus the deposition of synthetic diamond free from morphological defects and impurity inclusions is still one of the major technological challenges, which the scientific community has to face.

Characterization studies of the advanced materials are of crucial importance to achieve the optimisation of the growth process of layers and heterostructures. The numerous devices and techniques are used to analyse structural quality of III-nitrides and diamonds, including electron microscopy, atomic force microscopy, X-ray diffraction, Raman spectroscopy as well as optical and electrical properties studied by photoluminescence (PL), cathodoluminescence (CL), electron beam induced current (EBIC), time of light (TOF) or charge collection (CCD) techniques. Time resolved techniques have been shown as a versatile tool for investigation of semiconductors, as they provide straightforward information on carrier dynamics as well as

important parameters such as carrier/exciton lifetime, diffusion coefficient and length.

The carrier recombination and diffusion is governed by defect density in a material, therefore knowledge of carrier dynamics enables characterization of samples, optimisation of growth technology. The lifetime of nonequilibrium carriers is very sensitive to existence of point and extended defects in a material. The ratio between radiative and nonradiative recombination rates determines the internal quantum efficiency and therefore has a key importance for light emitting devices efficiency. The carrier diffusion coefficient and diffusion length are crucial electronic parameters for optoelectronic devices operation.

For the carrier dynamics investigation in wide bandgap semiconductors we mainly used the time-resolved light induced transient grating technique (LITG). LITG is a nonlinear optical technique, which enables to monitor electronic, thermal, acoustic properties of semiconductor by optical means. The advantages of LITG lies in its: 1) contactless and nondestructiveness (ohmic contact is a big problem for many semiconductors), 2) sensitivity (high signal to noise ratio is ensured because the signal is measured in dark field), 3) separation of diffusion and recombination processes by varying the grating period; 4) a possibility to study processes in the surface region (of ~1 μm) or in the entire bulk crystal, 5) investigation of processes under various experimental conditions (temperature, excitation intensity and wavelength), 6) applicability to wide range of semiconductor materials, ranging from heavily doped to semi-insulating . Among the mentioned features, the most important advantage of LITG is the spatially modulated excitation, which enables to measure not only local decay of excitation, but also the transport of excited species (the diffusion of carriers or temperature, sound propagation, etc).

The main **goals** of the thesis were gain a new knowledge on carrier dynamics in wide bandgap semiconductors (namely GaN, InGaN, and diamonds) by using and developing light induced transient grating technique. The experimental studies on numerous samples, grown at different conditions,

combined with extensive measurements in a wide range of carrier densities (10^{16}-10^{20} cm^{-3}) and temperature (9-300K) was targeted to identify the interplay of radiative an nonradiative recombination mechanisms, to determine carrier lifetime dependence on the excess carrier density, to explain the carrier diffusion coefficient dependence on excitation intensity, to find the optimal materials growth conditions. By planning ahead these investigations, were set the following specific **tasks**:

1. Development and implementation of the LITG scheme with diffraction optical element as a holographic beam splitter, that significantly simplifies the grating recording/detection scheme and enables heterodyne detection of the signal.

2. Investigation of high-density excess carrier recombination and diffusion peculiarities in different structural quality GaN, InGaN layers, and InGaN MQWs structures. Modeling of carrier dynamics and recombination mechanisms in samples with different dislocation density for determination of carrier photoelectrical parameters, as radiative and nonradiative recombination times, diffusion coefficients, diffusion length.

3. Investigation of carrier dynamics in different types of bulk HPHT diamonds and CVD grown layers at various excitation conditions and evaluation of their optical/electrical parameters.

Scientific novelty and importance

Further development of time-resolved optical techniques and devices for nondestructive characterization of photoelectrical properties of materials for semiconductor optoelectronics is needed for *ex situ* evaluation of new growth methods and concepts of technological innovations.

Implementation of holographic beam splitters for LITG optical scheme provided possibility to simplify the grating recording. It also enabled a heterodyne detection of the signal, an elimination of detrimental signal and background interference effect for rough samples, via control of the phase

between the LITG signal and scattered light. On the basis of this scheme, the new version of HOLO-device may be engineered.

LITG measurements, performed on numerous GaN layers (which have been provided by world leading technological centers and companies) with very vide range of threading dislocation density, enabled us to identify carrier recombination mechanisms and determine dislocation-governed carrier recombination lifetime as well as bimolecular recombination impact in wide temperature range. The numerical modeling of experimental results obtained at high excitation level and low temperature revealed the intrinsic nature of carrier recombination and diffusion variation.

Investigation of InGaN layers and structures provided photoelectrical parameters in layers with different In content, revealed In segregation induced carrier localization. The measurements in InGaN MQWs showed longer carrier lifetimes and pronounced bimolecular recombination even at room temperature.

Determination of carrier diffusion coefficient and carrier lifetime in artificially grown diamond crystals was demonstrated for the first time by optical means (picosecond LITG technique) and holds high importance to the field, where electrical determination of these parameters encounters some difficulties.

Statements presented for defence

1. Nonradiative threading dislocation governed recombination dominates for GaN layers with dislocation density higher than 10^8 cm^{-2}. The dislocation determined carrier lifetime could be approximated in wide dislocation range ($10^6 - 10^{10}$ cm^{-2}) as: $\tau[ns] = \frac{2.6 \cdot 10^4}{\sqrt{N_{TD}[cm^{-2}]}}$.

2. Bimolecular recombination (with determined $B = 2 \cdot 10^{-11}$ cm^3/s) is a dominant recombination channel at high carrier densities (~10^{19} cm^{-3}) if dislocation density of GaN layers is lower than 10^8 cm^{-2}.

3. Increase of ambipolar carrier diffusion coefficient D_a in GaN and InGaN at high carrier densities ($N > 10^{19}$ cm^{-3}) and even stronger increase of D_a at low T is due to Fermi pressure at degenerate carrier plasma.

4. The nitrogen related defects are the main recombination centers in diamond and determine variations of carrier lifetime and diffusion in polycrystalline CVD grown layers, while in nitrogen-free HPHT and single crystal CVD diamonds these parameters peak up to 2.8 ns and 9.2 cm^2/s.

5. By movement of holographic beam splitter along its grating vector, the phase difference between the background and diffraction signal in LITG experiment is controllable, thus enabling heterodyne detection and determination sign's change of refractive index modulation.

Layout of the thesis

The thesis is arranged in the following way. The Chapter 1 gives overview of carrier dynamics in wide bandgap semiconductors. In the Chapter 2 the formation, detection and decay of light induced gratings is presented. The Chapter 3 describes the new scheme of LITG and original way of heterodyne detection of the signal. The details investigation of carrier dynamics in various GaN layers grown by different technologies, containing different amount of TTD is presented in the Chapter 4. Also this chapter contains numerical modeling of carrier dynamics at experimental conditions. In the Chapter 5 results obtained in InGaN layers and MQWs structures are presented. The Chapter 6 deals with nonequilibrium carrier dynamics in a diamonds grown by HPHT and CVD methods containing different amount of nitrogen related defects. The thesis is summarized by Concluding summary.

Author's contribution

The author carried out the majority of experiments described in the thesis. He wrote and used computer programs for modeling of carrier dynamics also

for PC control of experiments. The author was very active in interpretation of results and prepared several drafts of publications [A2, A5], also contributed to preparation process of others drafts.

List of paper related to the thesis:

[A1] K. Jarašiūnas, R. Aleksiejūnas. **T. Malinauskas**, V. Gudelis, T.Tamulevicius, S. Tamulevicius, A. Guobiene, A. Usikov, V. Dmitriev, H. J. Gerritsen, "Implementation of diffractive optical element in four-wave mixing scheme for *ex situ* characterization of hydride vapor phase epitaxy-grown GaN layers," Rev. Sci. Instrum. **78**, 033901 (2007).

[A2] **T. Malinauskas**, S. Nargelas, R. Aleksiejūnas, K. Jarašiūnas, "Heterodyne detection scheme for light-induced transient grating experiment," Opt. Commun. **281**, 6061-6064 (2008).

[A3] R. Aleksiejūnas, M. Sudzius, **T. Malinauskas,** J. Vaitkus, K. Jarašiūnas, S. Sakai, "Determination of free carrier bipolar diffusion coefficient and surface recombination velocity of undoped GaN epilayers," Applied Physics Letters **83** (6), 1157-1159 (2003).

[A4] S. Juršėnas, S. Miasojedovas, G. Kurilcik, A. Žukauskas, R. Aleksiejūnas, **T. Malinauskas**, M. Sudzius, K. Jarašiūnas, "Transients of carrier recombination and diffusion in highly excited GaN studied by photoluminescence and four-wave mixing techniques," Acta Physica Polonica **107** (2), 240-244 (2005).

[A5] K. Jarašiūnas, R. Aleksiejūnas, **T. Malinauskas**, M. Sudzius, E. Frayssinet, B. Beaumont, J.-P. Faurie and P. Gibart, “Characterization of differently grown GaN epilayers by time-resolved four-wave mixing technique”, Phys. Status Solid (a) **202**, 566 (2005).

[A6] **T. Malinauskas**, R. Aleksiejūnas, K. Jarašiūnas, P. Gibart, B. Beaumont, A. Kakanakova, E. Janzen, D. Gogova, B. Monemar, and M. Heuken, "All-optical characterization of carrier lifetimes and diffusion lengths in MOCVD-, ELO-, and HVPE-grown GaN", J. Cryst. Growth **300** (1), 223-227 (2007).

[A7] E. V. Lutsenko, A. L. Gurskii, V. N. Pavlovskii, G.P. Yablonskii, **T. Malinauskas**, K. Jarašiūnas, B. Schineller, M. Heuken, "Determination of carrier diffusion length in MOCVD-grown GaN epilayers on sapphire by optical techniques," Physica Status Solidi (c) **3**, No. 6, 1935-1939 (2006).

[A8] K. Jarašiūnas. **T. Malinauskas**, A. Kadys, R. Aleksiejūnas, M. Sūdžius, S. Miasojedovas, S. Juršėnas, A. Žukauskas, D. Gogova, A. Kakanakova- Georgieva, E. Janzen, H. Larsson, B. Monemar, P. Gibart and B. Beaumont, "Application of picosecond four-wave mixing and photoluminescence techniques for investigation of carrier dynamics in bulk crystals and heterostructures of GaN". Phys. Status Solidi (c) **2**, No. 3, 1006-1009 (2005).

[A9] **T. Malinauskas**, K. Jarašiūnas, R. Aleksiejūnas, D. Gogova, B. Monemar, B. Beaumont, and P. Gibart, "Contribution of dislocations to carrier recombination and transport in highly excited ELO and HVPE GaN layers", Phys. Status Solidi (b) **243**, No. 7, 1426-1430 (2006).

[A10] K. Jarašiūnas, **T. Malinauskas**, R. Aleksiejūnas, B. Monemar, V. Ralchenko, A. Gontar, and E. Ivakin. "Optical characterization of defect-related carrier recombination and transport features in GaN substrates and CVD diamonds, Mat. Sci. Forum **600-603**, 1301-1304 (2009)

[A11] **T. Malinauskas**, K. Jarašiūnas, M. Heuken, F. Scholz, and P. Bruckner, "Diffusion and recombination of degenerate carrier plasma in GaN", Phys. Status Solidi (c) **6**, No. S2, S743-S746 (2009).

[A12] **T. Malinauskas**, K. Jarašiūnas, S. Miasojedovas, S. Juršėnas, B. Beaumont, P. Gibart, "Optical monitoring of nonequilibrium carrier lifetime in freestanding GaN by time-resolved four-wave mixing and photoluminescence techniques," Appl. Phys. Lett. **88**, 202109 (2006).

[A13] K. Jarašiūnas, R. Aleksiejūnas, **T. Malinauskas**, M. Sūdžius, S. Miasojedovas, S. Juršėnas, A. Žukauskas, R. Gaska, J. Zhang, M. S. Shur, J. W. Yang, E. Kuokštis, and M.A. Khan, "Carrier diffusion and recombination in highly excited InGaN/GaN heterostructures", Phys. Status Solidi (a) **202**, No. 5, 820 (2005).

[A14] **T. Malinauskas**, K. Jarašiūnas, E. Ivakin, V. Ralchenko, A. Gontar, S. Ivakhnenko, "Optical evaluation of carrier lifetime and diffusion length in synthetic diamonds", Diamond and Relat. Mat. **17**, 1212-1215 (2008).

Publications not included in the thesis:

[B1] Z. Bougrioua, M. Azize, B. Beaumont, P. Gibart, **T. Malinauskas**, K. Neimontas, A. Mekys, J. Storasta, K. Jarašiūnas, "Photoelectric properties of highly excited GaN : Fe epilayers, grown by modulation- and continuous-doping techniques," J. Cryst. Growth **300** (1), 228-232 (2007).

[B2] K. Jarašiūnas, R. Aleksiejūnas, T. Malinauskas et al., "Nonequilibrium carrier dynamics in heavily p-doped GaAs," European Physical Journal-Applied Physics 27 (1-3), 181-184 (2004).

[B3] K. Jarašiūnas, E. Gaubas, R. Aleksiejūnas; R. M. Sūdžius, V. Gudelis, **T. Malinauskas**, P. Prete, A. M. Mancini, N. Lovergine, "Studies of carrier dynamics in epitaxial heterostructures by nonlinear optical and microwave techniques," Physica Status Solidi a-Applied Research 195 (1), 238-242 (2003).

[B4] K. Jarašiūnas, **T. Malinauskas**, and R. Aleksiejūnas, "Dislocation-density dependent carrier lifetime and stimulated recombination threshold in GaN," AIP Conference Proceeding **893**, 295-296(2007).

[B5] K. Jarašiūnas, **T. Malinauskas**, K. Neimontas, V. Gudelis, R. Aleksiejūnas, "Time-resolved transient grating spectroscopy for studies of nonequilibrium carrier dynamics in wide band-gap semiconductors," Acta Physica Polonica A **110** (2), 201-209 (2006).

[B6]. E. V. Lutsenko, V. N. Pavlovskii, A. V. Danilchyk, K.A. Osipov, N.V. Rzheutskii, V.Z. Zubialevich, A.L. Gurskii, G. P. Yablonskii, T. Malinauskas, K. Jarašiūnas, K. Kazlauskas, S. Juršėnas, S. Miasojedovas, A. Žukauskas, Y. Dikme, H. Kalisch, R.H. Jansen, B. Schineller, M. Heuken, "Optical properties and carrier dynamics in differently strained GaN epilayers grown on Si by MOVPE," Physica Status Solidi (a) **203** (7), 1759-1763 (2006).

[B7] B. Monemar, P.P. Paskov, J. P. Bergman, A.A. Toropov, T.V. Shubina, **T. Malinauskas**, A. Usui 'Recombination of free and bound excitons in GaN' phys. stat. sol. (b) **245**, No.9, 1723 (2008).

[B8] B. Monemar, P. P. Paskov, J. P. Bergman, T. Paskova, C. Hemmingsson, T. Malinauskas, K. Jarašiūnas, P. Gibart, and B. Beaumont 'Time-resolved spectroscopy of excitons bound at shallow neutral donors in HVPE GaN', Physica B-Condensed Matter, **376**, 482 (2006).

[B9] P. P. Paskov, R. Schifano, T. Paskova, **T. Malinauskas**, J. P. Bergman, B. Monemar, S. Figge, and D. Hommel 'Photoluminescence of a-plane GaN: comparison between MOCVD and HVPE grown layers', Physica B-Condensed Matter, **376**, 473 (2006).

[B10] P. P. Paskov, R. Schifano, **T. Malinauskas**, T. Paskova, J. P. Bergman, B. Monemar, S. Figge, D. Hommel, B. A. Haskell, P. T. Fini, J. S. Speck, and S. Nakamura 'Structural defect-related emissions in nonpolar a-plane GaN', Physica Status Solidi C, **3**, No 6, **3**, 1499 (2006).

[B11] K. Neimontas, T. Malinauskas, R. Aleksiejūnas, R. Yakimova, and K. Jarašiūnas "Temperature-dependent nonequilibrium carrier dynamics in epitaxial and bulk 4H- SiC", Lithuanian Journal of Physics **46**, No.2, 199 (2006).

Acknowledgements

First of all, I would like to give my special thanks to my supervisor prof. Kęstutis Jarašiūnas for his endless energy, inspiration and care.

My best thanks to laboratory colleagues for the finest atmosphere, fruitful discussions and assistance.

Finally, I would like to thank my family for tolerance and support.

1. Time resolved studies of wide bandgap semiconductors

1.1. Exciton and free carrier dynamics in GaN

The time resolved studies of semiconductors provide information about dynamics of various electronic transitions and recombination lifetimes of injected carriers. These studies are important and give information for fundamental material science as well as for practical use of materials in semiconductor industry, since determined quantities correlates with material quality, purity, doping level, etc. The investigation of carrier/exciton dynamics in III-nitrides is mainly done by time resolved photoluminescence (TRPL) spectroscopy [1-4], since it is versatile technique able to investigate excitation dynamics in very wide range of excitation and time delay. The time evolution of different spectral ranges provide information on a rate of different radiative and nonradiative transitions in excited semiconductor. The cathodoluminescence studies [5-7] features extremely high spatial resolution (several nm), since material is excited by very tightly focused electron beam, thus is used spatial mapping of carrier dynamics peculiarities. The other class of techniques used for time resolved measurements is pump probe techniques were usually carriers are excited by short pulse of UV light (via band-to-band transition) and probed by broadband white continuum [8], microwave absorption [9, 10], photoconductivity [9, 10], light scattering by induced transient lens [11], or by diffraction of probe beam (this work or [12]). If to compare mentioned techniques they differ by excitation (intensity, energy, duration), detection mechanism, and time-resolution. Therefore, observed physical process and decay constants are very different, ranging from stimulated recombination with decay time of ~10 ps [8] to low density carrier trapping with time constants in order of milliseconds [9].

Free excitons. If the quality and purity of a GaN are sufficiently high (low densities of defect and impurities), the photoexcited electrons and holes pair off into free excitons by Coulomb interaction, which recombine, emitting

narrow line with energy $h\nu = E_g - E_x$, where $E_x \approx 25–26$ meV is a binding energy of the free exciton in GaN. Due to high binding energy free exciton could be observed up to room temperature in GaN. Free exciton emission dominates in moderate densities, since at high density the Coulomb interaction is screened and excitons dissociated in electron hole plasma. At very low densities and temperature free-excitons become bind to neutral donors and/or acceptors. The decay time of TRPL from the A exciton (hole from A valance band) was varying from 10 –50 ps at low temperatures in thin samples due to the dominance of nonradiative transitions in heteroepitaxial samples[13, 14] and reached values of 90 ps in thick high quality HVPE GaN layers[1]. The authors showed that this PL decay time is not the radiative lifetime of the A free exciton, since corresponding PL signal is collected just from a thin near surface layer, and exciton diffusion to sample reduces exciton density near surface. Also this decay could be affected by surface recombination. The real lifetime of A exciton is obtained by analyzing phonon replica emission since it is not reabsorbed in material. The investigation showed that free exciton lifetime in bulk reaches values longer than 1.4 ns at 2K in best HVPE samples. Measurements of the free exciton lifetime with two-photon spectroscopy (what ensures flat excitation profile and therefore no in-depth diffusion) on free standing HVPE samples were recently reported, resulting in an estimated radiative lifetime of free excitons up to 2 ns at low temperatures [15].

Excitons bound to neutral impurities. At low temperatures PL spectra is dominated by transition of excitons bound to neutral donors (Si, O) and acceptors. Bound excitons are the prime optical signatures of the presence of impurities in semiconductors, and are thus of major importance for material characterization. The energy of transitions are lower than free exciton by binding energy - $h\nu = E_g - E_x - E_{bx}$. As temperature increases, the bound excitons become thermally ionized. From a simple theory predicting a so-called giant oscillator strength F_{DBE} [16], one can expect a constant radiative decay times ($\tau \sim 1/F_{DBE}$) of bound exciton. The PL decay of the DBE no-phonon line at low temperatures shows a non-exponential behavior, with a fast

initial slope corresponding to a decay time of about 300 ps, and a much slower tail towards longer times [1]. The no-phonon donor bound exciton decay is distorted by optical dispersion in the semiconductor medium with exciton resonances and surface effects, but the radiative decay times of 1.3 - 1.4 ns can be estimated from the decay of the respective phonon replicas and two electron transitions.

A nice exponential decay for acceptor bound exciton most probably associated to Mg is typically observed. The decay time varies for different samples, presumably due to a nonradiative contribution from excitation transfer effects. An upper value of 0.9 ns is found from low temperature data [1, 17, 18]. Presumably the radiative decay time exceeds 0.9 ns with a margin that is perhaps not accurately measured as yet.

Free carriers. Band-to-band emission of free carrier is observed in many TRPL experiments at room temperature and high excitation. At high carrier densities (10^{19} cm^{-3}) (which are above Mott density[19]) and higher than room temperature exciton system (excitation energy well above bandgap is used, therefore of carrier temperature becomes higher than lattice[2]) excitons are thermally ionized and/or screened by high carrier density. In this situation wide band of PL around GaN bandgap energy of 3.39 eV is observed. Experiment at these conditions allows materials characterization under conditions that are close to the semiconductor laser operation regime. Despite that the TRPL detects radiative recombination, the carrier recombination dynamics in majority experiments described in literature is determined by nonradiative recombination, thus these measurements very sensitively reflects material quality.

There is a limited number of reports related to the TRPL lifetimes of excess carriers in GaN at 300 K. Kwon *et al*[20] reported a biexponential decay with 150 and 740 ps time constants for high-quality Si-doped MOCVD-grown GaN/sapphire. Decay times between 205 and 530 ps were measured for thick HVPE-grown templates[21-23], and values ranging from 445 [2] to 506 ps [23] were reported for homoepitaxially grown GaN layers. In addition, Chichibu *et*

al.[24] and Izumi *et al*.[25] reported biexponential decays with lifetimes τ_1 and τ_2 of 130 and 400 ps, and 80 and 459 ps, respectively, for GaN/sapphire films grown using ELO. However, the same groups obtained longer biexponential lifetimes of 130 and 860 ps [24], and 98 and 722 ps [25]for bulk GaN.

TRPL studies in different quality GaN epilayers were described in [2]. Luminescence intensity transients under high excitation for estimation of the carrier capture time in GaN epilayers fabricated using various techniques is presented. Low-quality GaN epilayers exhibited the luminescence decay time below 10 ps, while good quality heterolayers of GaN of about 1-μm thickness grown by MOCVD over sapphire substrate showed the luminescence lifetime of about 100 ps. Meanwhile, a homoepitaxial GaN epilayer, grown under similar conditions by MOCVD shows the largest luminescence decay time τ_{LU} = 445 ps (carrier lifetime $\tau = 2 \cdot \tau_{LU}$ = 890 ps). Thick GaN epilayers (100 μm) grown by hydride vapor-phase epitaxy had a rather large luminescence decay time τ_{LU} = 205 ps. Authors concluded that in samples with a decreased number of dislocations, carrier recombination is still controlled by nonradiative traps but of different origin (point defects). Therefore, further improvement of the materials quality for purely radiative band-to-band recombination at room temperature can be achieved through mitigation of nonradiative traps originating from point defects.

Band-to-band luminescence decay versus dislocation density was investigated by TRPL[3]. The nonexponential TRPL transient were fitted by two exponential fit. The longer decay time values which was associated with carrier lifetime varied from 1 ns at dislocation densities of about $5 \cdot 10^5 cm^{-2}$ to 100 ps at $\sim 10^{10} cm^{-2}$. The weak dependence of carrier lifetime versus dislocation density (power index less than –1/4) was explained by presence of points defects (namely Ga vacancy and its complexes), which was proved by positron annihilation technique. The origin of nonexponential shape of TRPL transients was not addressed.

TRPL being as a tool to control the technological process of crystal growth was demonstrated in several papers [26-28]. In was shown that, growth of GaN thin films on SiN and TiN porous network templates significantly improved the structural quality and the radiative efficiency of the overgrown layer. In terms of the decay times, the samples with TiN network showed much better performance (almost two times increase in decay times) than the samples with SiN network. The slow decaying component for the 15 min nitridation sample had decay time constant τ_{LU} = 1.86 ns time constant that is comparable with the result of τ_{LU} = 1.73 ns from a 200 μm-thick freestanding GaN.

Most of above described room temperature high excitation TRPL transients revealed nonexponential decay. The authors fitted this decay with two exponential model, which can not be obtained from a single carrier continuity equation solution, therefore physical meaning of fit is doubtful. The reason for this nonexponential shape of TRPL transient were investigated in this work and explained as carrier diffusion into depth caused carrier density reduction and therefore PL intensity addition decay not related to carrier recombination. After publishing this work several papers[15, 29], appeared where in-depth diffusion was suppressed by exciting carriers in the whole thickness of the sample by below bandgap excitation with low absorption coefficient.

The low carrier density dynamics in GaN layers were investigated by contact photoconductivity (CPC) and microwave absorption techniques (MWA) [9, 10]. The time scale of the relaxation rate exhibited a crossover from picoseconds for stimulated emission to hundreds of nanoseconds for multitrapping. In the asymptotic part, a stretched-exponent decay on the millisecond scale was observed with the disorder factor of α =0.7. The asymptotic decay was explained by competition of centers of nonradiative recombination within bulk of the material and trapping attributed to the dislocations. Effects of disorder, which are inherent for as-grown material due to the high density of dislocations, manifest themselves in the long-tail CPC as well as MWA decays with a time stretching factor of 0.7.

1.2. Time resolved studies in InGaN

InGaN is a key material for many commercially available green-blue LEDs and LDs. Many investigation were carried out on InGaN-related epilayers and MQWs structures for identifying the nature of optical transitions at the fundamental absorption edge[30-32]. However, a few essential problems still remain unresolved, in particular, those regarding the emission spectral and temporal dynamics with temperature, nonequilibrium carrier density, quantum-well width, and In molar fraction. The investigation shows that in indium containing nitride compounds, indium atoms are nonhomogeneously distributed with pronounced In content fluctuations[30-32]. This inhomogeneity localize nonequilibrium carriers and therefore increases the quantum efficiency enhances of InGaN-based light-emitting devices][32]. However in InGaN MQWs due to strain-induced piezoelectric polarization at interfaces quantum-well potential is tilted (quantum confined Stark effect), which results in electron and hole wave function separation and reduction of radiative efficiency.

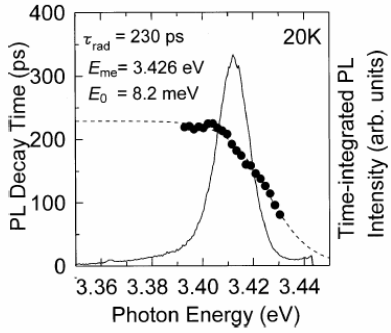

Fig.1.1. Time-integrated PL spectrum and the PL decay time as a function of monitored photon energy at 20 K of $In_{0.02}GaN_{0.98}$/GaN UV-LED (After ref.[33]).

In TRPL measurements In segregation caused carrier localization is observed as PL decay time dependence on emitted photon energy within wide band-to-band emission band [24, 33-35] (Fig.1.1). High energy PL corresponding to recombination of carriers/ excitons with higher energy has short PL decay time (~100 ps) since it is determined not only by radiative and nonradiative recombination rates, but also by migration of carrier to lower states. The low energy PL decay constants correspond to carrier/exciton lifetimes and vary in wide range from ~100 ps to nanoseconds

[24, 34, 36]. The nonexponential decay shape is also caused by screening of piezoelectric polarization induced fields. At higher carrier densities this field becomes fully screened and electron and hole wavefunctions overlap, thus increases probability of radiative recombination, and decay time shortens. During recombination carrier densities reduces, as well as screening effect, therefore overlap of wavefunctions decreases and decay becomes slower.

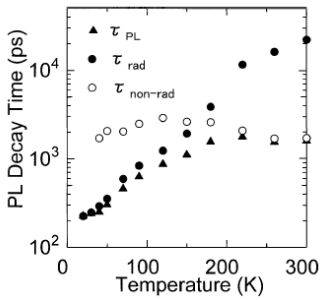

Fig.1.2. The temperature dependence of τ_{PL} , τ_{RAD}, and $\tau_{NON\text{-}RAD}$ in $In_{0.02}GaN_{0.98}$/GaN UVLED (after Ref. [33])

The Fig.1.2. shows the temperature dependence of radiative and nonradiative recombination lifetimes in the $In_{0.02}GaN_{0.98}$/GaN UV LED obtained from temperature dependence of the time integrated PL intensity and PL decay lifetimes . [33]. The radiative time increased gradually with temperature as $T^{3/2}$, which was suggested to be characteristic behavior of a nearly free 3D exciton. On the other hand the derived nonradiative time was almost constant at 2 ns. The authors concluded that nonradiative recombination rate was greatly suppressed by the addition of a small amount of In to the active layer.

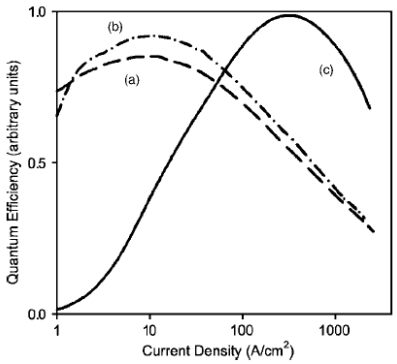

Fig.1.3. Relative quantum efficiency of two 2.5 nm QW (a), six 2.5 nm QW (b), and 13 nm DH (c) LEDs vs current density. All LEDs emit at λ=430 nm. Measurements are taken with pulsed drive at room temperature (After ref. [37, 38]).

In the development of InGaN-based light-emitting diodes LEDs, producers encountered reduction of internal quantum efficiency of LED at high current densities, which was called as a efficiency droop problem [39](Fig.1.3). Several carrier loss mechanisms to explain the droop phenomenon have been proposed such as carrier leakage [40, 41], carrier delocalization [42, 43], and Auger nonradiative recombination [44] [37, 38]. TRPL transients measured in set of InGaN samples with different In content was modeled with presence of Auger recombination and provided Auger coefficients in range from $1.4 \cdot 10^{-30}$ to $2.0 \cdot 10^{-30}$ cm^6 s^{-1}[37, 38]. Nevertheless, the clear nonexponential carrier dynamics with recombination rate increasing as squared carrier density was not yet shown.

1.3 Time resolved studies in diamonds

Diamond is a wide-band-gap semiconductor having a band gap energy of 5.47 eV at room temperature (RT). Although it is an indirect gap semiconductor, excitonic recombination emission has been observed in natural and high-pressure high-temperature (HPHT) diamonds by many groups using cathodoluminescence (CL), provided by the high (80 meV) binding energy for the free exciton [45]. In chemical vapor deposited (CVD) diamond, Collins et al. have observed this for the first time [46]. The crystallinity of CVD diamond film progresses extremely allowing for the observation of dominant free exciton emission, even at RT[47]. Nevertheless, just few optical time-resolved investigations were done in this field.

Hammesberg et al. [48] presented an experimental study of the mobility-lifetime products and free carrier lifetimes for CVD grown polycrystalline diamond samples of various qualities, with variations in average grain size and nitrogen content. The investigation showed carrier lifetime dependence on nitrogen content. Nitrogen free diamonds exhibit lifetime values up to 150 ns, while samples with nitrogen impurity density around 10^{15} - 10^{16} cm^{-3} had carrier lifetime shorter than 5 ns. Authors concluded that carrier lifetime is dominated by trapping and recombination at the grain boundaries, leading to a strong coupling to the average grain size in polycrystalline diamond. Salvatori et al.[49] also used the same technique for mobility and lifetime determination. The measurement showed that in polycrystalline CVD diamond carrier mobility is about 40 cm^2/Vs and carrier lifetime of about 100 ps, while in single crystal diamond theses values peak up to 2500 cm^2/Vs and 150 ns, correspondingly.

Fujii et. al.[50] and Chiorboli et. al.[51] measured TRPL transient at UV excitation in high quality HPHT and single crystal CVD diamonds. The 23 ns lifetime of exciton were reported for room temperature measurements, while at low temperature exciton decay was slower of about 52 ns.

Charge carrier dynamics in CVD homoepitaxial diamond thin films were evaluated using a fast TOF system with time resolution of 150 ps by Oshiki et al.[52]. The best values of lifetimes of electrons and holes in evaluated diamond films were 1.8 ± 0.3 ns for both charge carriers.

2. Light-induced transient grating technique

LITG technique was a tool for few decades to study dynamics of electronic, thermal, optical, and mechanical properties of materials[53]. The experiments were carried out on large variety of materials including solid, liquids and gases. The different optical nonlinearities were employed for grating recording such as free-carrier[54, 55], thermal[56, 57], electronic polarization[58], acousto-optic[59], and others.

LITG is one of many "pump-probe" techniques and therefore shares common benefits such as nondestructive, contactless, high spatial and temporal resolution, wide spectral and temperature tunability. On other hand nonhomogenous excitation of material during LITG experiment provides benefits such as high signal to noise ratio, ability to measure not only local decay of excitation (e.g. carrier/exciton recombination), but also transport properties of excitation (e.g. carrier and thermal diffusion, sound propagation, and others). Quite difficult experimental and interpretation procedures limit wide usage of this technique.

In this chapter light-induced transient grating technique is introduced. The three sections will describe how diffractive grating is created, how it decays and how experimentally these processes are observed.

2.1. Grating recording and optical nonlinearities

The main principle of light-induced transient grating technique is to excite transient grating in a material using the interference of two pump beams and to scan the decay of the grating measuring the diffraction efficiency of the third (probe) beam. For the grating recording two TEM_{00} beams, which are very closed to ideal plane waves, are used. The interference pattern of two planes (Fig.1) waves produces spatially periodic light intensity profile:

$$I(x) = I_0(1 + m\cos(K_G x)), \qquad (2.1)$$

where I_0 is $I_0 = I_1 + I_2$ a sum intensity of pump beams, $m = \frac{2\sqrt{I_1 I_2}}{I_1 + I_2}$ is modulation depth, $K_G = \frac{2\pi}{\Lambda}$ is a grating vector. Λ is a grating period which can be varied by changing incident angle of pump beams as $\Lambda = \frac{\lambda}{2\sin(\theta/2)}$.

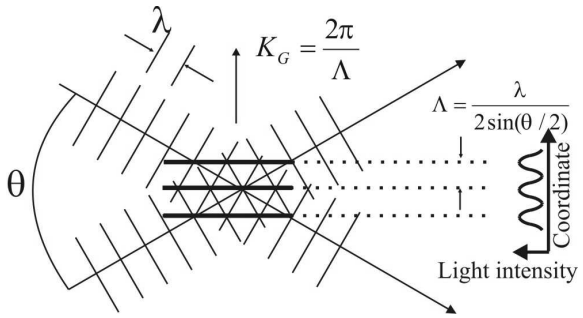

Fig. 2.1. Formation of transient grating by interference of two coherent laser beams [53].

When a material is placed into the interference region of the pump beams the spatial modulation (grating) of some material property, e.g. the conduction electron density (in a semiconductor), the space charges and their accompanying fields (in photo refractive materials), or the temperature, or the molecular orientation (fluids) is created and this leads to a change of optical material properties (e.g. refractive index and absorption coefficient).

In semiconductor the very wide variety of optical nonlinearities can be explored or used to study non optical properties of material because the dominant nonlinear mechanisms a dependant on the energy of pump and probe light quantum, on experimental configuration, on temperature, or the time scale used in the experiment.

In most of our experiments ***free-carrier*** nonlinearity is dominant mechanism formatting the diffraction grating. The free carriers are generated in a semiconductor if it is exposed to a light. If energy of light quantum is higher than the bandgap then electron-hole pairs are generated via band-to-band transitions, while if energy is lower than E_g the two-photon/two-step

absorption, or carrier generation from impurity levels dominates. The refractive index and absorption coefficient change can be calculated using Drude model, which treats electrons and holes classically as quasi-free particles (with effective masses m_e and m_h) oscillating in the light field. The induced optical dipole moment and polarizability of electrons and holes are calculated leading to the following expressions for the refractive and absorption index changes:

$$\Delta n = -\frac{e^2}{2n_0\omega^2\varepsilon_0}\left(\frac{\Delta N_e}{m_e}+\frac{\Delta N_h}{m_h}\right) = \Delta N n_{eh}, \tag{2.2}$$

$$\Delta \alpha = \frac{e^2}{n_0\omega^2 c\tau_d\varepsilon_0}\left(\frac{\Delta N_e}{m_e}+\frac{\Delta N_h}{m_h}\right) = \Delta N \sigma_{eh}. \tag{2.3}$$

Here ΔN is the density of the optically excited electron hole pairs, ω the circular frequency of probe light, τ_d electron impulse relaxation time, n the undisturbed refractive index of the material; n_{eh} gives the refractive index change for one electron-hole pair per volume element and σ_{eh} the absorption cross-section.

The free-carrier nonlinearity is dominant if energy of probe beam quantum is far from material resonance, i.e. at transparent region of material. Also it is seen that the electrons dominate in refractive and absorption index modulation since usually $m_e < m_h$.

Two processes generate the ***thermal gratings*** in semiconductor: hot carrier cooling or nonradiative recombination. Experimentally hot carriers are created then sample is excited with light quantum with energy much higher than E_g, then $(h\nu - E_g)/h\nu$ part of absorbed energy is transferred to phonon system during electron and hole cooling process. If a sample has initial high electron carrier density these carriers can be heated with interference pattern of two infrared beams, exciting them into higher energy states in the conduction band.

The thermal grating are also observed in samples with high nonradiative recombination centers concentration. The energy of electron-hole pair equal to Eg is transferred to phonon system during nonradiative recombination.

Experimentally the thermal grating is observed refractive index grating (phase grating) with positive thermo-optic coefficient:

$$\Delta n = \frac{\partial n}{\partial T}\Delta T \,. \qquad (2.4)$$

The thermal modulation become more pronounced at low temperatures since at low temperatures the material thermal capacity decreases, and the same excitation intensity generates higher thermal gradients.

Thermal gratings often couple to ***stress-strain grating*** because of thermal expansion of medium[60, 61]. The sudden spatially periodic thermal modulation creates standing ultrasound wave, which oscillates with period equal to $T = \Lambda/v$, where v is sound speed in a medium.

2.2. Diffraction - grating detection

The created spatial modulation of complex refractive index can be measured from the diffraction of probe beam. The diffraction is strongly dependent on the grating thickness *d*. A rough estimation of grating thickness is made from comparison with grating period: if *d* is of the order of Λ or smaller, the grating is called thin, otherwise it is called thick. The more precise condition for thin grating can be obtained dividing the whole grating to smaller elements of arbitrary thickness. The phase difference *Q* between beams diffracted at two neighboring elements is equal to[53]

$$Q = 2\pi d\lambda / \Lambda^2 n, \qquad (2.5)$$

here λ is the vacuum wavelength. If the phase difference is sufficiently small ($Q << 1$) the beams from all grating elements interfere constructively. If the phase difference is large ($Q >> 1$), destructive interference occurs and the total diffracted intensity becomes small. Only in the case of oblique incidence at an angle α and a diffraction angle $\phi = 2\alpha$, which can be considered as reflection of the incident beams at the grating plane, there is no phase difference between all the beams diffracted at the grating planes (Fig 2.2b). In such a case strong diffraction can be observed in a thick grating, too. Experiments results

reported in these thesis where obtained at a thin grating regime since typical Q value was around Q ~ 0.1 (d ~ 1 μm, λ ~ 1 μm, Λ ~ 5 μm, n ≈ 2.3).

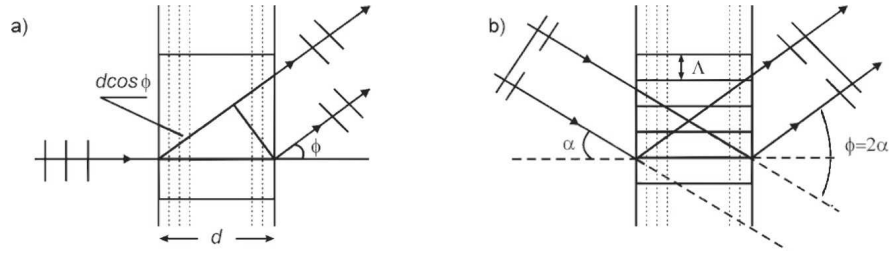

Fig. 2.2. Diffraction at a thick grating treated by successive diffraction of the incident beam at thin grating elements: (a) normal incidence, (b) Bragg diffraction [53].

The main experimental quantity which is measured during LITG experiment is diffraction efficiency η, which is ratio between transmitted and diffracted beams $\eta = I_D/I_T$. For thin absorption and refractive index grating the diffraction efficiency of the first diffraction order is given by [53]:

$$\eta = \left|J_1(\phi)\right|^2 \tag{2.6}$$

here J_1 – first order Bessel function, $\phi = 2\pi\Delta\tilde{n}d/\lambda$, $\tilde{n} = n + ik$ - complex refractive index, d – grating width, and λ – wavelength of the probe beam.

For $\phi << 1$ the following approximation hold:

$$J_1(\phi) \approx \frac{\phi}{2}, \tag{2.7}$$

and diffraction efficiency then is equal to:

$$\eta = \left|J_1(\phi)\right|^2 \approx \left|\frac{\pi\Delta\tilde{n}d}{\lambda}\right|^2 = \left(\frac{\pi\Delta nd}{\lambda}\right)^2 + \left(\frac{\Delta\alpha d}{4}\right)^2 \tag{2.8}$$

As a rule, in the spectral region below bandgap the absorption is weak and the Δn>Δk for free-carrier, thermal, and stress-strain gratings, therefore (2.8) absorption term can be omitted:

$$\eta = \left(\frac{\pi\Delta nd}{\lambda}\right)^2 \tag{2.9}$$

Equation (2.9) together with (2.2) and (2.4) allows the estimation of carrier and temperature dynamics in semiconductor from measured diffraction efficiency.

2.3. Grating dynamics

The dynamics of light-induced grating depend on physical processes, which take place during material relaxation to equilibrium state. The time-scale of the decay can be very wide: femtosecond domain – for coherent electronic excitation, picosecond/nanosecond domain – free-carrier recombination and diffusion, thermal diffusion can last up to several microseconds, the electro-optic gratings in materials like $LiNbO_3$ in dark could remain for days, as the relaxation of space charge field is limited by a slow movement of ionized ions. The decay of the grating can be exponential with characteristic decay time, but more often it is complicated nonlinear process, which has no analytic solution, and can be only described on by solving differential equations. In this section the main emphasis will be taken to free-carrier grating dynamics, but some peculiarities of thermal and stress-strain gratings will also be introduced.

The free-carrier grating is created by optical generation of free carriers, and its amplitude decays due two processes – carrier recombination and diffusion along grating vector.

Carrier recombination[62, 63]. Recombination of electrons and holes is a process by which both carriers annihilate each other: electrons occupy - through one or multiple steps - the empty state associated with a hole. Both carriers eventually disappear in the process. The energy difference between the initial and final state of the electron is released in the process. This leads to one possible classification of the recombination processes. In the case of radiative recombination, this energy is emitted in the form of a photon. In the case of non-radiative recombination, it is passed on to one or more phonons and in Auger recombination it is given off in the form of kinetic energy to another electron. Main processes of electron-hole plasma recombination are illustrated in Fig. 2.3.

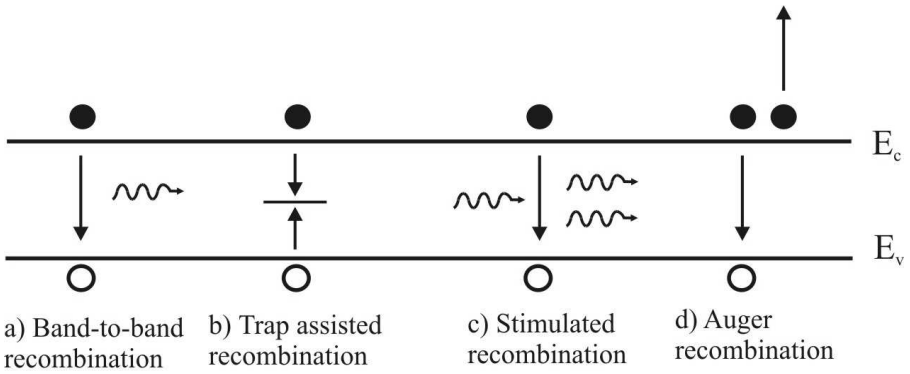

Fig.2.3 Mechanisms of electron-hole recombination in semiconductors: a) Bimolecular recombination, b) Shockley-Read-Hall recombination, c) Stimulated recombination, d) Auger recombination.

Band-to-band recombination (see Fig. 2.3a) occurs when an electron falls from its conduction band state into the empty valence band state associated with the hole. This band-to-band transition is typically also a radiative transition in direct bandgap semiconductors. Band-to-band recombination depends on the density of available electrons and holes. Both carrier types need to be available in the recombination process. Therefore, the rate is expected to be proportional to the product of *n* and *p*. Also, in thermal equilibrium, the recombination rate must equal the generation rate since there is no net recombination or generation. As the product of *n* and *p* equals n_i^2 in thermal equilibrium, the net recombination rate can be expressed as:

$$R = B\left(np - n_i^2\right), \tag{2.10}$$

here *B* is the bimolecular recombination constant.

Trap-assisted recombination occurs when an electron falls into a trap, an energy level within the bandgap caused by the presence of a foreign atom or a structural defect. The electron occupying the trap, in a second step, falls into an empty valence band state, thereby completing the recombination process. This process is called Shockley-Read-Hall (SRH) recombination. The net recombination rate for trap-assisted recombination is given by:

$$R_{SHR} = \frac{pn - n_i^2}{p + n + 2n_i \cosh\left(\frac{E_i - E_F}{k_B T}\right)} N_t \nu_{th} \sigma, \tag{2.11}$$

here E_i and E_F are intrinsic Fermi and trap energies, ν_{th} – thermal velocity, σ – the cross-section of carrier capture by defect state. For minority carrier case the above equation for recombination rate R simplifies to:

$$R_n = \frac{n - n_0}{\tau_n} \quad \text{for p >> n,} \tag{2.12}$$

$$R_p = \frac{p - p_0}{\tau_p} \quad \text{for n >> p,} \tag{2.13}$$

where

$$\tau_n = \tau_p = \frac{1}{N_t \nu_{th} \sigma}. \tag{2.14}$$

The special case of SRH recombination is the surface carrier recombination. Recombination at semiconductor surfaces and interfaces can have a significant impact on the behavior of devices. This is because surfaces and interfaces typically contain a large number of recombination centers because of the abrupt termination of the semiconductor crystal, which leaves a large number of electrically active dangling bonds. In addition, the surfaces and interfaces are more likely to contain impurities since they are exposed during the device fabrication process. The surface recombination mathematically is accounted using boundary conditions for differential continuity equation.

Auger recombination is a process in which an electron and a hole recombine in a band-to-band transition, but now the resulting energy is given off to another electron or hole. The involvement of a third particle affects the recombination rate so that we need to treat Auger recombination differently from band-to-band recombination. The expression for the net recombination rate is similar to that of band-to-band recombination but includes the density of the electrons or holes, which receive the released energy from the electron-hole annihilation:

$$R_{Auger} = C_n n\left(np - n_i^2\right) + C_p p\left(np - n_i^2\right). \quad (2.15)$$

The exact modeling of carrier dynamics requires set of continuity equations for electrons, holes, several different traps, also for internal field dynamics. Fortunately, the experimentally used high excitation conditions allow making several approximations. At intense band-to –band generation the equal number of hole and electrons are created, also at high carrier densities hole and electron recombination rates are equal [4]. The high carrier density screens internal fields and electron hole are bound together and diffuse at ambipolar diffusions conditions. The Auger recombination in direct wide bandgap semiconductors has very low probability compared to other recombination processes, therefore it can be omitted. These approximations allow using single particle model:

$$\frac{dn}{dt} = \nabla D \nabla n - \frac{n}{\tau_R} - Bn^2 + G, \quad (2.16)$$

with boundary condition

$$D\frac{\partial n}{\partial z} = -Sn, \quad (2.17)$$

where S is the surface recombination velocity. The linear term in right-hand side can be attributed to carrier capture to deep centers, the quadratic term describes the bimolecular recombination, while cubic term – Auger recombination. In LITG experiment all recombination processes could be involved, thus a decay of grating will be described by effective recombination time τ:

$$\frac{1}{\tau} = \frac{1}{\tau_R} + Bn \quad (2.18)$$

Carrier diffusion. The spatially non-homogeneous light pattern used in LITG experiment creates a spatially modulated carrier concentration, which gives rise to diffusion of carriers from illuminated areas to dark ones with low carrier concentration. The diffusion process is described by diffusion coefficient D related to carrier mobility μ via Einstein's relation:

$$D = \frac{k_B T}{e} \mu. \tag{2.19}$$

The mobility is defined from the proportionality of carrier drift velocity v_d vs. external electric field E, $v_d = \mu |E|$. μ is expressed in the following way:

$$\mu = \frac{e}{m^*} \langle \tau \rangle, \tag{2.20}$$

here ⟨τ⟩ stands for net drift momentum relaxation time, averaged over the distribution function of carriers. The momentum relaxation could be driven by several physical scattering processes at the same time. The main scattering mechanisms include carrier-phonon, carrier-carrier scattering, also scattering by neutral, charged and extended defects, as well as interfaces and grain boundaries. The dominant mechanism depends on carrier concentration, lattice temperature, defect concentration and other physical factors of the system.

When both types of carriers are photogenerated, electrons tend to diffuse away from holes due to higher mobility. This charge redistribution establishes the electric field called Dember field between electrons and holes. Dember field opposes the separation of carriers, so electrons and holes diffuse together with ambipolar diffusion coefficient D_a expresses as:

$$D_a = \frac{n + p}{\frac{n}{D_h} + \frac{p}{D_e}}. \tag{2.21}$$

If concentrations of nonequilibrium carriers are equal, $n = p$, (2.21) provides:

$$D_a = \frac{2 D_e D_h}{D_e + D_h} \tag{2.22}$$

In contrary, if $n << p$, then $D_a \approx 2 D_e$, or when $p << n$, then $D_a \approx 2 D_h$, in other words carrier diffusion in monopolar case is driven by minority carriers.

As one of the simplest LITG experiment configuration can be considered a thick volume grating in semiconductor, where dynamic grating is erased by diffusion and linear recombination and internal space charge field is absent. The spatio-temporal carrier dynamics in this system is described by equation [54]:

$$\frac{\partial n(x,t)}{\partial t} = G(x,t) + D\frac{\partial^2 n(x,t)}{\partial x^2} - \frac{n}{\tau_R}, \tag{2.23}$$

here G(x, t) is the generation rate of free carriers, describing the spatial and temporal profile of exciting light field, n stands for carrier density, and τ_R is the effective carrier generation rate. For Dirac pulse (2.23) has an analytical solution [64]:

$$n(x,t) = n_0\left[1 + \exp(-t/\tau_D)\cos(K_g x)\right]\exp(-t/\tau_R) \tag{2.24}$$

here $K_g = 2\pi/\Lambda$ is the grating vector, and diffusion decay time τ_D is given by:

$$\tau_D = \frac{\Lambda^2}{4\pi^2 D}. \tag{2.25}$$

The carrier grating amplitude Δn decays with the grating decay time

$$\frac{1}{\tau_G} = \frac{1}{\tau_R} + \frac{1}{\tau_D} = \frac{1}{\tau_R} + \frac{4\pi^2 D}{\Lambda^2}. \tag{2.26}$$

It is seen from (2.26) that the diffusion and recombination terms can be distinguished if function $1/\tau_G = f(\Lambda^{-2})$ is known. This relationship will be addressed many times and is used to find the diffusion coefficient D and recombination time τ_R.

We would like to stress once more, that analytical expression (2.24) is valid only in the simple case of one-dimensional volume grating, when internal electric field is absent as well. If more difficult systems are considered, e.g. photorefractive crystals or the case of strong light absorption in sample, what is related to subsequent carrier diffusion into the depth and strong surface recombination, the more complicated models have to be used. These models and results of numerical solution will be presented in Chapters 4.2 and 4.3.

The diffraction efficiency is proportional to the square of the modulation depth of the grating. Therefore, the diffraction efficiency decays at twice this rate, thus

$$\eta(t) \propto \exp(-2t/\tau_G). \tag{2.27}$$

3. Experimental setup and heterodyne detection scheme for light induced transient grating

In this chapter the two LITG experimental setups will be introduced. Firstly, standard LITG scheme will be presented. Secondly, the more attention will be given to recently installed LITG setup with holographic beam splitter which allows heterodyne detection of diffracted signal.

3.1. Standard LITG experimental setup

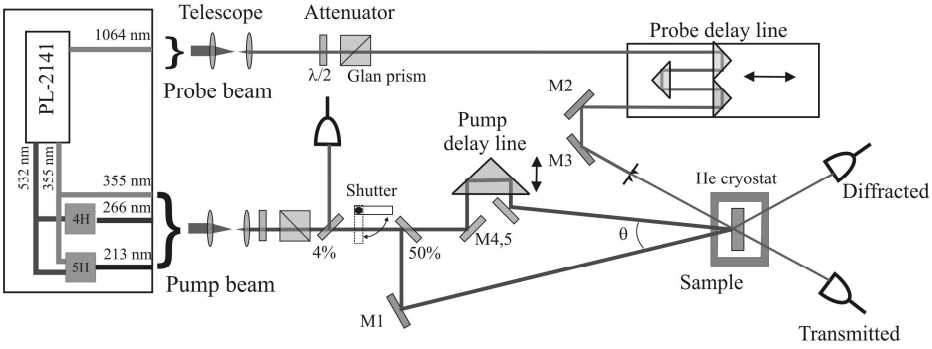

Fig. 3.1 Standard setup of LITG experiment with dielectric beam splitter.

In Fig. 3.1 the setup used for LITG experiment is depicted. It is based on mode-locked YAG:Nd laser PL-2141 provided by “Ekspla” company. It generates 22 – 25 ps duration pulses (the duration depends on modulation dye condition) at fixed 10 Hz repetition rate. The pulses feature good energy stability (< 1.5 % sd in fundamental harmonics at 1064 nm) and high polarization degree. Maximum pulse energy is ≈30 mJ in fundamental harmonic, ≈15 mJ at 532 nm and ≈10 mJ at 355 nm. An available wavelength range is further increased by using the nonlinear crystals for generation of fourth (266 nm) and fifth (214 nm) harmonics. The fifth harmonic is achieved in separated module by mixing second and third harmonics, and separated using quartz prism. The another equivalent experimental setup is based on YLF:Nd laser. The main difference of this setup is shorter pulse duration ~7 ps, a three time lower pulse energy – around 10 mJ in a fundamental

harmonic. The wavelengths of a fundamental harmonic and higher harmonics are slightly lower, namely 1054 nm, 527 nm, 351 nm.

The grating-recording beam of required wavelength is collimated using a telescope, which also decreases the beam diameter from ~ 6 mm at laser exit down to ≈1 – 2 mm. The energy of recording beams is attenuated either by polarization rotator (λ/2 plate) and polarizer (Glan prism) or by varying electronically the triggering time of amplifier flash lamp, what also results in altered output energy of the laser. In a standard LITG configuration, a dielectric beam splitter divides pump beam to two parts of approximately equal energies. These two recording beams are arranged to cross at sample position at an angle θ which is controlled by the reflection angle and position of mirror M1. The difference in travel paths of the beams is compensated using a pump delay line in one arm of recording beams. The shutter is used to close recording beams periodically, what allows an estimation intensity of scattered light, i.e background.

The probe beam in all experiments was of 1064 nm wavelength, because all investigated samples are transparent for the given wavelength. The probe beam is collimated using a telescope, which also decreased beam diameter from ≈ 6 mm at laser entrance to ≈ 2 mm. A λ/2 plate together with Glan prism is used to polarize the probe beam (linearly p-polarized probe was used in the most of experiments) and to attenuate it as well. For the delaying of probe a step-motor driven delay line of 150 mm travel length is used. It allows a maximum delay of ≈ 2 ns (taking into account a four-fold travel path) with respect to recording beams. A 0.3 – 0.5 mm diameter pinhole is installed at the close proximity to sample to decrease the diameter of probe and keep it 2 – 3 times smaller compared to the excited sample spot.

Energies of recording, diffracted and transmitted beams are measured using Si photodetectors controlled by data acquisition unit. The energies of all pulses were acquired at 10 Hz frequency. The energy of recording beams was calibrated to its absolute value using pyroelectric joulimeter. The data

acquisition unit is integrated with step motors by LabView software shell, which is used for automatic control of the experiment. During diffraction kinetic measurement, for every probe beam delay 30 - 50 laser pulses are recorded and afterwards discriminated and averaged.

3.2. Heterodyne detection scheme for light induced transient grating experiment

The standard LITG scheme (Fig. 3.1) was successfully used, regardless of experimental difficulty to make temporal and spatial overlap of three beams. The light pulse of 10 ps duration occupies 3 mm in space; therefore optical paths of both pump beams should coincide with this precision. The LITG experiment requires measurements at several grating periods, i.e. several pump beam intersection angles, and therefore experimental arrangements should be performed quite often, what to do in nonsymmetrical scheme is quite difficult.

In LITG experiment the diffracted beam propagates in different direction than other intense beams, what allows the detection of a signal in the "background-free" area, which is considered as a big advantage of the technique. However, there is always a background of light scattered from a sample and optics. Our experience suggests that majority of background illumination originates from the scattering in a sample. Particularly, this comes true for hard to polish materials like sapphire (most common substrate for nitrides), SiC, and diamond. Rough surface and large structural defects within samples result in a high optical background and, thus, low signal-to-background ratio. If degenerate LITG arrangement is considered, i.e. the common arrangement when pump and probe beams are of different wavelength, the background of pump beams can be easily eliminated using spectral filters, while the scattered probe is of the same wavelength and polarization as signal and is extremely difficult to get rid of it. Moreover, these light fields are coherent; therefore, they interfere in a detector. The detected signal becomes dependent on relative phase between diffracted signal and

background lighting. The phase-dependence has to be accounted for in order to obtain the correct decay times of transients.

Both problems can be solved using a heterodyne detection setup with holographic beam splitter (Fig.3.2), which allows a simple deconvolution of diffracted signal and interference term with a background and also makes very easy change of transient grating period Λ. The key element of the setup is a holographic beam splitter (HBS), which can be moved along its grating vector. The deconvolution is achieved by subtracting two decay kinetics, recorded at different HBS positions, which correspond to the opposite phases of interference term. The applicability of presented arrangement will be demonstrated for carrier lifetime measurement as well as for observation of free-carrier and thermal nonlinearities in diamonds grown by chemical vapor deposition (CVD).

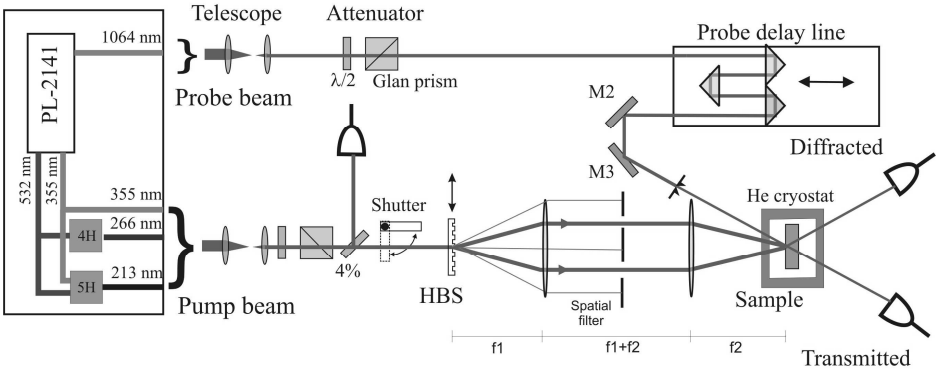

Fig. 3.2. Experimental scheme of LITG experiment using holographic beam splitter.

Scheme. The experimental setup presented in Fig. 3.2 differs from a standard scheme in the way how recording beams are a formed. The two pump beams are obtained using a holographic beam splitter [65]. We used the rectangular profile diffraction gratings etched in quartz and optimized so that the incoming beam is diffracted mainly into the firsts (±1) diffraction orders [66]. The telescope, comprised of two lenses with focal lengths *f*1 and *f*2, images the grating onto a sample, creating the spatially periodic excitation of nonequilibrium carriers and the subsequent modulation of refractive index, i.e. a transient grating. Higher diffraction orders are blocked with a spatial mask. A

period of the transient grating Λ is equal to $\Lambda = \Lambda_{HBS}/2 \cdot f_2/f_1$; here, factor 2 comes because ±1 diffraction orders are used instead of 0^{th} and 1^{st} orders. By using a permanent diffraction grating as the beam splitter, the temporal and spatial adjustment of the two interfering beams becomes quite easy. Moreover, the change of the dynamic grating period is performed by replacing the HBS with another one of a different period.

Transient grating is probed in same way as in standard scheme. A delayed probe beam partially diffracts on transient grating. Diffraction efficiency $\eta(\Delta t) = I_D/I_T$ is a quantitative measure of diffraction, where I_D and I_T stand for the intensities of diffracted and transmitted beams. Since η is proportional to the square of induce refractive index change Δn^2, which in turn is proportional to the modulated carrier density ΔN (i.e. $\eta \propto \Delta n^2 \propto \Delta N^2$), the kinetics of $\eta(\Delta t)$ directly reflect the carrier dynamics in nanosecond time scale.

The interference of signal and background. Heterodyne detection. The main part of background light, detected by detector which measures diffracted beam, comes probe beam scattered in a sample. Since diffracted beam and scattered light arises from the same beam they partly coherent and do *interfere*. The interference of diffracted beam and optical background alters light intensity measured by a photo-detector:

$$I_S(\theta, \Delta t) = I_D(\Delta t) + I_B + 2\gamma\sqrt{I_D(\Delta t) I_B}\cos(\theta) \qquad (3.1)$$

where I_D and I_B are intensities of the diffracted beam and background light, θ and γ are the phase difference and the degree of coherence between the respective optical fields. The coefficient γ accounts for the spatially uneven phase of a background within the cross-section of a detector. It is always less than 1 and decreases if detector aperture is increased. As a consequence, decreasing of a detector aperture (i.e. using a pinhole) leads to a better signal-to-noise ratio and the bigger amplitude of interference term in (3.1) (i.e. higher γ value) as the smaller area of scattered light has a better-defined phase. In our experiments, γ value was approximately equal to 0.3 for 0.5 mm diameter of the probe beam for many GaN, SiC, and diamond samples.

It is evident from Eq. (3.1) that heterodyning of diffracted signal and background, if neglected, can lead to the misinterpretation of LITG results. Usually, in the LITG experiment signal intensity (I_S) is measured first and then the background intensity I_B is estimated by closing one or two pump beams. The kinetics of diffraction intensity $I_D(\Delta t)$ is obtained plainly subtracting I_B from I_S for each Δt. However, if heterodyning takes place the kinetics will be distorted. In Fig.3.3. we show the calculated kinetics ($I_D(\Delta t) \propto \exp(-2\Delta t/\tau_G)$, τ_G = 500 ps) for three values of I_S / I_B and for two phases of interference term. For small I_S / I_B values (≤ 4 at peak), the kinetics are clearly non-exponential, which can be considered as an indicator of the possible heterodyning. On the other hand, even if the peak signal exceeds the background by 100 times and γ is as low as 0.3 the kinetics are different from $I_D(\Delta t)$, though in the presented time scale they strongly resemble an exponential decay.

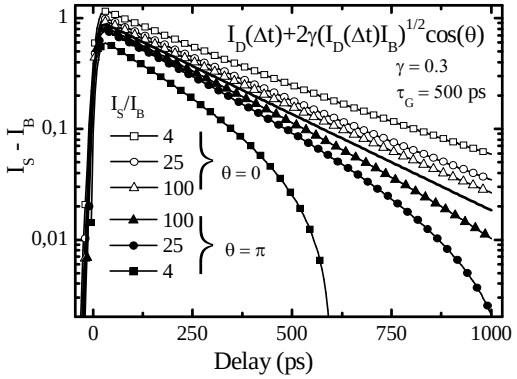

Fig. 3.3. The calculated LITG signal kinetics for I_S / I_B ratios of 4, 25, and 100 and for two phase values θ of 0 and π. The solid line indicates the kinetics of diffraction signal without interference $I_D(\Delta t) \propto \exp(-2\Delta t/\tau_G)$ [A2].

The deconvolution of I_D and $\sqrt{I_D}$ parts can be achieved via the control of the phase difference θ between the signal and the background. Even more, this would allow a determination of an instantaneous sign of the induced refractive index modulation, i.e. to distinguish between the cases $\Delta n < 0$ or $\Delta n > 0$. Such a control can be achieved varying the optical path Δx of either diffracted or background light fields. The diffracted beam can be considered as

a result of stimulated scattering from a periodical structure – transient grating, while the background arises from the light scattering from the sample imperfections. Optical path (and thus a phase) of diffracted beam in the setup with HBS can be changed moving the latter along it's grating vector, because this moves it's image on the sample and shifts the position of fringes of transient grating. Phase shift and gratings displacement are related as $\theta = 2\pi\Delta x/\Lambda$[53], here Λ stands transient grating period. Since the optical path of the scattered light remains constant, the variation of optical path of diffracted beam changes the phase difference θ and the signal measured by photo-detector. A shift by $\Lambda_{HBS}/4$ corresponds to phase shift by π; again, 4 in the denominator arises because a transient grating is recorded by ±1 diffraction orders. We found out that the opposite way of phase control is also experimentally possible, i.e. the average background phase at the detector can be changed simply moving a sample (i.e. moving the scattering centers) along the grating vector of transient grating; sample shift by Λ/2 corresponds to phase shift by π. In Fig. 3.4 we show photodetector signal as a function on sample (a) or HBS (b) position. We note, however, that sample movement in experiment is not desirable and should be avoided because of possible inhomogeneous distribution of its parameters.

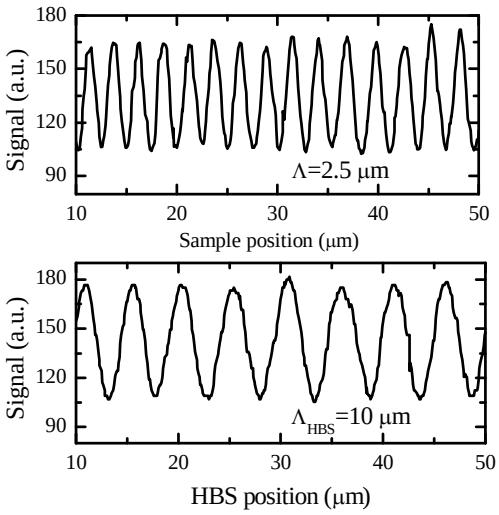

Fig. 3.4. The overall signal I_S as a function on sample(a) and HBS(b) position (Λ_{HBS} = 10 μm, f_2/f_1=0.5, Λ = 2.5 μm) [A2].

We employed the following procedure for LITG with heterodyne detection. We measure $I_S(\theta,\Delta t)$ kinetics at $\theta = \theta_0$ and $\theta = \theta_0 + \pi$. Averaging

these two signals we eliminated the interference term (see Eq. (3.1)), thus the unaltered dynamics of squared refractive index could be observed:

$$\Delta n^2(\Delta t) \propto I_D(\Delta t) = (I_S(\theta,\Delta t)\big|_{\theta=\theta_0} + I_S(\theta,\Delta t)\big|_{\theta=\theta_0+\pi})/2 - I_B. \quad (3.2)$$

Here, the background intensity I_B is a photodetector signal with pump beams closed. A dynamics of the sign of refractive index can be monitored calculating difference between $I_s(\theta_0,\Delta t)$ and $I_s(\theta_0+\pi,\Delta t)$:

$$\Delta n(\Delta t) \propto \sqrt{I_D(\Delta t)} \propto (I_S(\theta,\Delta t)\big|_{\theta=\theta_0} - I_S(\theta,\Delta t)\big|_{\theta=\theta_0+\pi})/\sqrt{I_B}. \quad (3.3)$$

We note that the presented technique generally allows no determination of the absolute value of Δn, since the absolute phase difference θ_0 is not known. But if the nature of an optical nonlinearity and the sign of Δn can be deduced for some delay time Δt_0, the kinetics of Δn can be measured without sign uncertainty.

Experimental demonstration. The presented technique was employed to monitor the dynamics of free-carrier and thermal optical nonlinearities in photo excited diamond crystals grown by chemical vapor deposition [67]. We studied two samples sample #1 and sample #2; sample #2 has about 5 times higher concentration of nitrogen which acts as nonradiative recombination centers [68]. The transient grating in the samples was recorded by frequency-multiplied 25 ps duration pulses of Nd:YAG laser at λ = 213 nm or λ = 266 nm wavelength. The telescope (see Fig. 2.1) was made of two spherical quartz lenses with focal distances f_1 = 300 mm and f_2 = 150 mm (magnification f_2/f_1=0.5). The pulses at 1064 nm was delayed up to 2 ns and used to probe the transient grating decay. The HBS was mounted on the computer-controlled translation stage with the minimal step of 14 nm.

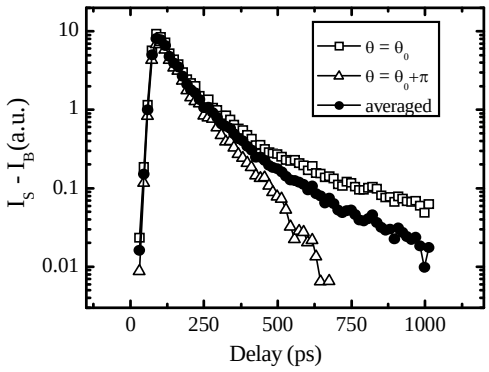

Fig. 3.5. Heterodyne signal kinetics measured for two opposite phase differences θ between the diffracted and scattered light (open symbols) and the extracted diffraction kinetic (filled symbols) [A2].

In Fig. 3.5 we show the kinetics of photodetector signal, obtained in sample #1 at $\lambda = 213$ nm excitation, which quantum energy is sufficient for carrier band-to-band generation. The kinetics were measured at two HBS positions, corresponding to a shift of the diffracted beam phase by π. Apparently different, these kinetics prove the heterodyning of diffracted beam and the background; the estimated γ value is 0.3. Kinetics of diffraction signal I_D (black dots in Fig. 3.5) represents a decay of the carrier grating and was obtained according to formula (3.2) by averaging the two kinetics (open dots).

Interplay of several optical nonlinearities of different physical origin using a heterodyne LITG was observed in the sample #2. In Fig. 3.6 we show LITG kinetics measured at below-bandgap excitation (266 nm). Strong interference between the background and diffracted light in this sample was indicated by large interference degree $\gamma > 0.4$. We observed rather complicated decay kinetics, with region where signal I_S dropped bellow the background level, which had been measured separately (this points out to a strong destructive interference). To exclude the interference effect, we applied (3.2) and (3.3) formulas and obtained kinetics of light induced refractive index change Δn and Δn^2 (Figs. 3.7a,b).

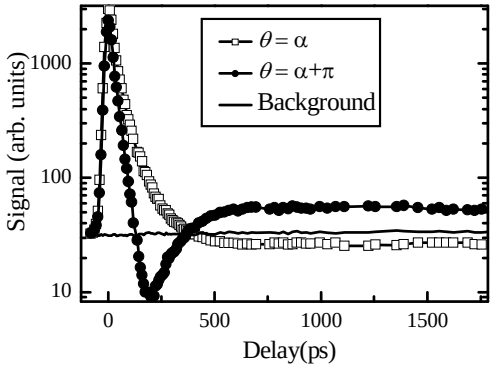

Fig.3.6. Heterodyne signal kinetics measured in CVD diamond sample at 266 nm excitation and at two different phase differences θ between the diffracted and scattered light [A2].

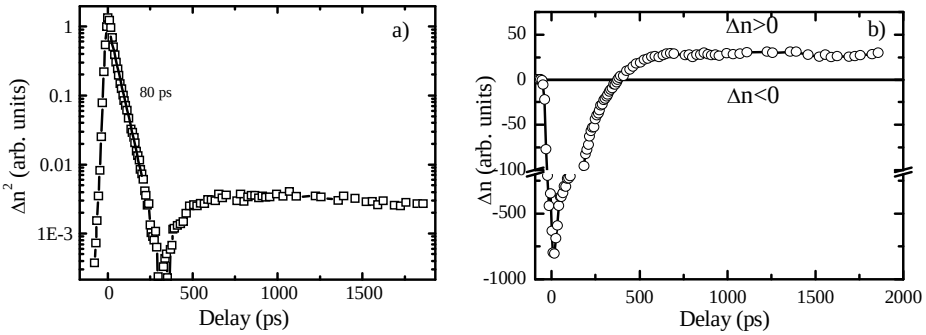

Fig.3.7. The kinetics of light induced refractive index modulation (Δn^2 (a) and Δn (b)) in CVD diamond, extracted from LITG kinetics (Fig. 2.6) [A2].

Figure 3.7a shows a dynamics of the grating diffraction efficiency $I_D(\Delta t)$, which is proportional to the index modulation squared. This type of characteristic can be obtained by the conventional LITG experiment, when no heterodyning is present. The fast exponential decay within 0 - 300 ps delay interval corresponds to the free-carrier nonlinearity and provides carrier lifetime of 80 ps. This value is >3 times smaller than the one in the sample #1 and confirms faster carrier trapping by abundant defect states in sample #2. At later delay times the signal reappears and decays with much slower time constant. The heterodyne detection enabled us to measure Δn dynamics, which is shown in Fig. 3.7b. It clearly shows that Δn sign changes a sign at ~380 ps.

Since Δn reaches zero we observe a dip in Δn^2 transient at this particular delay time.

The physical reason of Δn sign inversion is the competition of two coexisting optical nonlinearities with different Δn signs, generation and relaxation rates. The initial change of refractive index we attribute to the photogeneration of free carriers, which according to the classical Drude model lead to a reduction of refractive index $\Delta n_{eh} = -\frac{2\pi e^2}{n m^* \omega^2} \Delta N$. Therefore, we subtracted $I_s(\theta_0)$ and $I_s(\theta_0 + \pi)$ kinetics (Fig. 2.7b) in that way to obtain negative Δn in the initial stage of kinetic. The later positive change of refractive index we prescribe to the thermal optical nonlinearity. A nonradiative recombination of excited carriers locally heats the lattice. The change of lattice temperature modulates the refractive index $\Delta n_T = \frac{\partial n}{\partial T} \Delta T$. Taking into account that free carrier optical nonlinearity has a negative sign, heterodyne detection enabled us to deduce that thermo-optical coefficient $\frac{\partial n}{\partial T}$ in diamond is positive.

3.3. Summary

A novel heterodyne detection scheme for light induced transient grating technique is developed. The heterodyne detection is achieved coherently mixing the picosecond pulses of diffracted and scattered light. A phase difference between these fields is controlled by moving HBS along its grating vector. LITG signal decay kinetics, recorded at two HBS positions corresponding for phase difference of π, allow to separate Δn^2 and Δn kinetics, which is impossible in the convenient transient grating setup.

This approach was employed to study a competition of coexisting free carrier and thermal optical nonlinearities in CVD grown diamond films in sub-nanosecond time domain and to determine carrier parameters.

4. Carrier dynamics in GaN

4.1. Contribution of dislocations to carrier recombination

Group III-nitride semiconductors are the key materials for the next generation of electronic devices ranging from high power/ high temperature electronics to blue-UV emitters and sensors. One the most serious problem in development of III-N based devises is lack of suitable substrate material on which the latticed–matched layers can be grown. Currently, the nitride materials, grown on sapphire, SiC, or Si substrates, contain a large density of threading dislocation (up to 10^{10} cm^{-2}). It is well established that threading dislocations are degrading the performance and the operating lifetime of optoelectronic devices. Ongoing development of GaN optoelectronic device technology require innovative growth technologies as well as the relevant control techniques able to evaluate the electrical properties of the fabricated heterostructures in a fast and contactless way.

In this Chapter the LITG investigation on the wide spectra of GaN layers grown by various techniques on different substrates is presented, which allowed to confirm the detrimental effect of dislocation on nonequilibrium carrier lifetime. The LITG experiments were carrier out at condition close to real device operation (LD's, high power devices), i.e. high carrier concentration.

The carrier dynamics in GaN samples was investigated using LITG technique. The experimental schemes described in Chapter 3 were employed. The interference of two third harmonic Nd:YAG laser beams (λ = 355, pulse duration 25 ps) was used for band-to-band excitation of carrier and creation of free-carrier grating in material. The pulse of the first harmonic at 1064 nm was delayed up to 2 ns and was used to probe transient diffraction grating. The excitation fluence I_0 of grating recording pulses varied from ~0.1 mJ/cm^2 to 10 mJ/cm^2 and created electron-hole pair density in range of 10^{18} - 10^{20} cm^{-3} at the very surface (in a depth of ~0.2 μm), as the absorption coefficient at 355 nm was about 10^5 cm^{-1}. The steep gradient of carrier caused carriers to diffuse

into the bulk of sample increasing the excited layer thickness up to 2 – 3 μm in experimental time domain, thus decreasing the carrier density by order of magnitude in about 1 ns (See Chapter 4.2). The typical diffraction efficiencies values were $\eta = (\pi n_{eh} \Delta N d/\lambda)^2$ = 0.001 –0.1% (calculated according 2.9 equation).

4.1.1 Investigation of GaN layers grown on sapphire substrates

Table. 4.1. The list of MOCVD grown samples and their basic properties.

Sample No	Growth technology	Substrate	Epilayer thickness, μm	Interface	TDD, cm^{-2}	Ref.
1	Standart MOCVD	sapphire	2.6	LT GaN	~10^9	[69]
2	Standart MOCVD	sapphire	3-4	LT GaN	$5 \cdot 10^8$	[70-72]
3	μ-ELO	sapphire	10	Si/N treatment of sapphire	~$5 \cdot 10^7$	
4	MOCVD	sapphire	0.7-1.7etched in steps	Optimized	Not available	[73]
5	Hot-wall MOCVD	4H-SiC	0.75	AlN	>10^9	[74]
6		6H-SiC	1.9			
7			2.4			
8	MOCVD	Si	1.2	AlN-AlGaN	-	[75]
9	MOCVD	Si/SiO/Si	1.2	AlN-AlGaN	-	
10	MOCVD	Si	0.75	AlGaN, superlatice	-	

The sample #1 was grown by MOCVD on low temperature 25-nm-thick buffer layer. This sample represents early stage of GaN growth technology featuring large density of threading dislocation TDD~10^9 cm^{-2}. Grating decay kinetics in the sample #1 has been measured at various grating periods Λ (Fig. 4.1) and demonstrated the increasing contribution of diffusive decay at smaller grating periods. Grating decay time τ_G was determined at probe beam

delay Δt > 500 ps, when the decay rate became nearly exponential. The bipolar diffusion coefficient D_a = 1.7 cm^2/s and carrier lifetime τ_R = 670 ps were determined by procedure described in Chapter 2.1, i.e. by plotting an inverse grating time τ_G^{-1} vs square of the inverse grating periods Λ^{-2} (Fig 4.1b). The assuming that electron diffusivity is higher than holes ($D_n >> D_p$) and $D_a = 2D_nD_p/(D_n+D_p)$, we estimated the hole diffusion coefficient $D_a \approx D_a/2$ and hole mobility $\mu_h \approx 32$ cm^2/Vs [76].

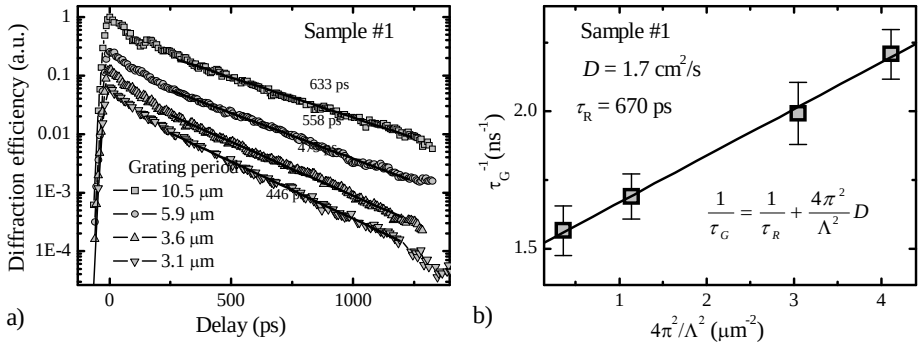

Fig. 4.1. Grating decay kinetics in 2.6 μm-thick GaN epilayer on sapphire (sample #1) at various grating periods(a), In (b), the plot of inverse grating decay time τ_G^{-1} as a function of Λ^{-2} is used to determine the values of ambipolar diffusion coefficient D_a and carrier lifetime τ_R by the linear fit according to Eq. 2.26 [A1].

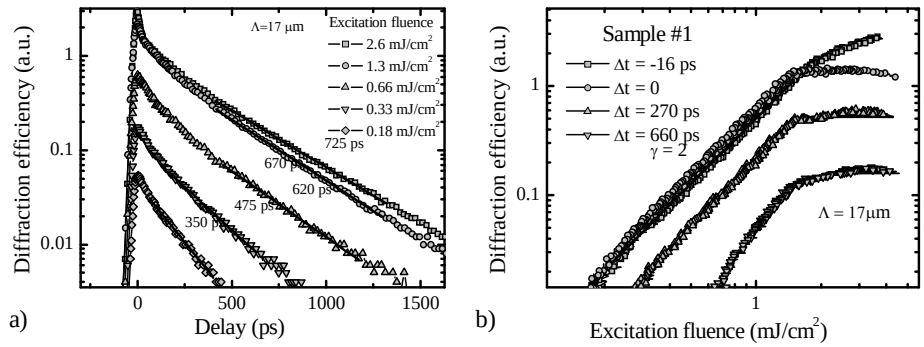

Fig. 4.2. LITG kinetics measured in sample #1 at different excitation fluences. The grating decay time values are plotted for each curve [A4].

Two features are characteristic for the kinetics measured at different excitation fluences (Fig.3.2) – the kinetics are slightly non-exponential and

carrier lifetime becomes longer at higher excitation (it varies from 350 ps at 0.18 mJ/cm^2 to 725 ps at 2.4 mJ/cm^2). This tendency is characteristic for low quality GaN layers and will be explained later.

An origin of very fast component in kinetics at high excitation fluence ($I_0 > 1.3$ mJ/cm^2) was attributed to stimulated recombination, as it was confirmed by time resolved PL measurements [A4]. The stimulated recombination acts as very fast recombination channel, which reduces carrier density to the threshold value, what can be easily seen in exposure characteristics (Fig.4.2b). The initial growth of signal at low excitation has slope equal to 2, which corresponds to linear band-to-band generation and quadratic dependence of signal on carrier density. At stimulated recombination onset the slope reduces to zero what shows that additionally created carriers momentary recombine, and therefore LITG signal does not rise.

The samples #2 and #3 are grown by company Lumilog [70-72]. The 5 μm-thick reference sample #2 was grown by conventional MOCVD process on sapphire. Sample #3 was grown by micro epitaxial lateral overgrowth (μ-ELO) technology. An amorphous silicon nitride layer is deposited using a SiH_4/NH_3 mixture prior to the growth of the low temperature GaN buffer layer. Such a process induces a 3D nucleation at the early beginning of the growth, resulting in a kind of maskless ELO process with random opening sizes. This produces a significant decrease of the threading dislocation density compared to the best GaN/sapphire templates. Ultra Low Dislocation density (ULD) GaN layers were obtained with TD density as low as ~5x10^{7}cm^{-2}.

LITG kinetics at large grating periods (>12 μm) reflects solely recombination processes, since diffusive decay of the grating is much slower compared to recombination one ($\tau_D = \Lambda^2/4\pi^2 D >> \tau_R$). The LITG diffraction kinetics measured at large grating period (Λ = 15 μm) in samples #2 and #3 for several excitation fluences (I_0 = 0.2 – 1.3 mJ/cm^2) are shown in a figure 3.3. For a standard sample #2 they exhibited singe-exponential decay in wide excitation range with grating decay time τ_R = 1.1 ns, what show nonradiative

character of recombination mechanism. Nevertheless the kinetics measured in ULD sample #3 in experimental time scale (up to 2 ns) look like single exponential, the stable decrease of grating decay time with increasing excitation could be observed (τ_G = 2.8 ns at 0.22 mJ/cm^2 and τ_G = 2.3 ns at 0.7 mJ/cm^2). This shows that at ULD sample #3 the probability of nonradiative recombination of carrier is reduced and intrinsic bimolecular recombination ($\tau_{radiative} = 1/BN$) mechanism is significant, but still nondominant since dependence of carrier recombination rate versus excitation is sublinear.

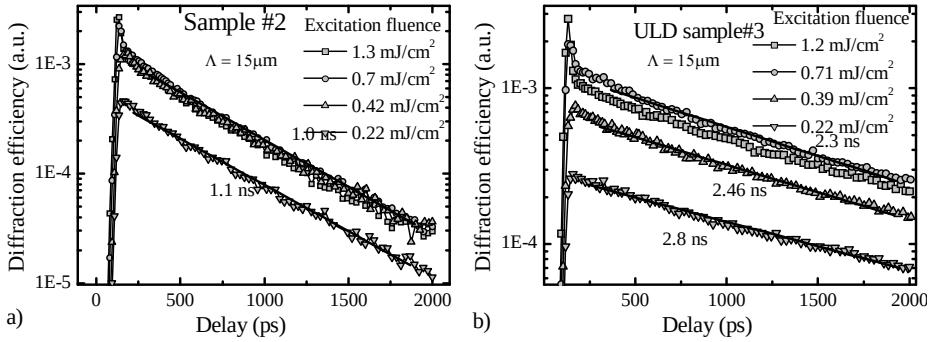

Fig. 4.3. LITG kinetics measured in samples #2 and #3 at different excitation fluences. The grating decay time values are plotted for each curve [A5,A6].

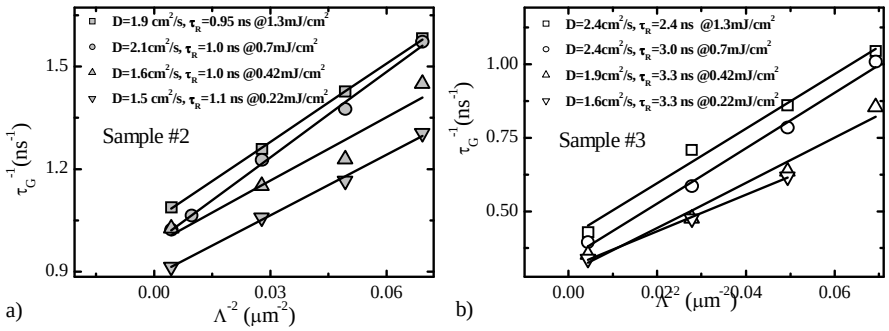

Fig. 4.4. The plots of inverse grating decay time τ_G^{-1} as a function of Λ^{-2} for several excitation fluences are used to determine the values of bipolar diffusion coefficient D_a and carrier lifetime τ_R by the linear fit according to Eq. 2.26 in standard MOVCD sample #2 (a) and μ-ELO ULD sample #3(b) .

For every excitation fluence the measurement at several grating periods (Λ = 3.8 – 15 μm) were performed in order to measure carrier ambipolar

diffusion coefficient and exact values of carrier lifetimes. The angular characteristics constructed by in Chapter 2 described procedure are shown in Fig. 4.4. As mentioned above carrier lifetime is almost constant for sample #2, and is equal to 1.1 at low excitation fluence, while carrier lifetime at sample #3 is dependent on carrier density and at lowest measured excitation is equal to 3.3 ns. This shows that reduction of threading dislocation density from 10^9 cm^{-2} down to $5 \cdot 10^7$ cm^{-2} leads to 3 times longer carrier lifetime. If take into mind that carrier lifetime in μ-ELO sample is influenced by radiative recombination, the nonradiave recombination is even longer.

The measurement shows that carrier diffusion coefficient is dependent on excitation intensity, namely, it increases with the increasing excitation. For the sample #2 the D value varies from 1.5 cm^2/s at $I_0 = 0.22$ mJ/cm^2 to 2.1 cm^2/s at $I_0 = 0.7$ mJ/cm^2. For the sample #3 the D values are slightly higher correspondingly 1.6 and 2.4 cm^2/s. We suggest that the increase of D value with excitation is due to degeneracy of distribution of carriers. A detailed analysis will be given is Chapter 4.3.

The previously described results were obtained exciting GaN layer from the front (growth) side. The carriers were excited by strongly absorbed light in thin layer of around 200 nm, but later diffusion of carrier expanded investigated region to 1-2 μm thick layer. Undoubtedly, the investigation of the top most layer of the grown GaN is of the prime importance, since electronic and opto-electronic devices are formed here, but also investigation of interface between substrate and GaN is interesting, since subsequent growth of active layer highly depends on interface properties. The LITG experiment allowed investigation of the backside of the layer (the interface region between substrate and GaN) by exciting carrier via transparent for UV light sapphire substrate. In this case the experimental results represent the properties of 1-2 μm thick interface layer of GaN (carriers do not diffuse into sapphire because of higher bandgap energy).

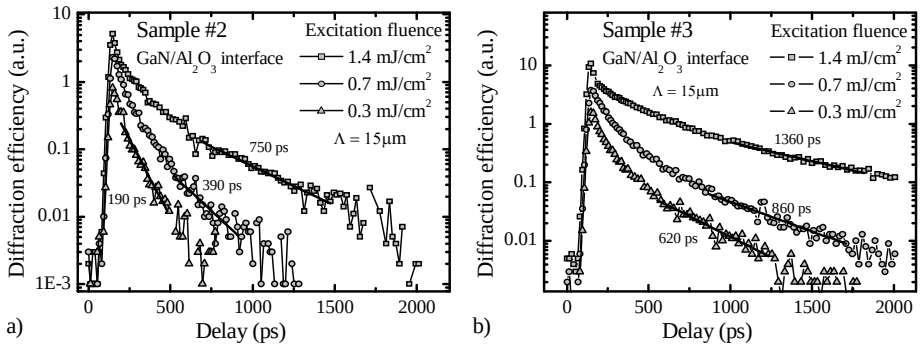

Fig. 4.5. LITG kinetics measured in samples #2 and #3 at different excitation fluences, exciting carriers at GaN/sapphire interface region. The grating decay time values calculated at slower part of kinetics are plotted for each curve [A5].

The LITG kinetics measured at GaN/sapphire interface of samples #2 and #3 were found to be strongly nonexponential, i.e. carrier lifetime becomes longer with increasing time after carrier excitation. Also, measurements at different excitation revealed that LITG kinetics become slower with increasing excitation fluence. We claim that the main reason for nonexponential character of kinetics is non-homogeneity of material properties in the investigated depth of sample. Non-uniform in-depth distribution of defects determines spatially varying carrier lifetime, what leads to the non-exponential character of observed kinetics. The faster parts of kinetics can be associated with recombination of carrier in the vicinity of interface, while slower kinetic parts correspond to layers that are away from the interface. The slower kinetics at higher excitation is observed since the more distant layers from GaN/sapphire interface are stronger excited. The deeper analysis and confirmation of the model that material properties are different at various distances from GaN/sapphire interface will be presented later for specially etched sample #4.

We calculated carrier diffusion coefficients using the slower parts (tails) of measured LITG kinetics in the vicinity of GaN/sapphire interface. For low excitation we observed low diffusivity ($D < 0.8$ cm^2/s) in standard grown sample #2. At higher excited carrier densities the value of carrier diffusion coefficient increased up to $D \approx 3$ cm^2/s (Fig. 4.6a). We explain this increase by

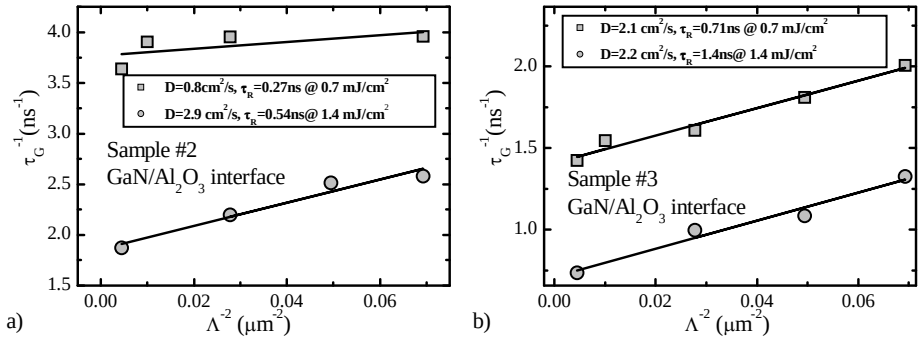

Fig. 4.6. The plots of inverse grating decay time τ_G^{-1} as a function of Λ^{-2} for several excitation fluences are used to determine the values of bipolar diffusion coefficient D_a and carrier lifetime τ_R by the linear fit according to Eq. 2.26. in standard MOVCD sample #2 (a) and μ-ELO ULD sample #3 exciting carrier at GaN/sapphire interface region [A5].

screening of potential barriers by generated free carriers. The initial growth of GaN has columnar manner, with typical dimension of grains of ~100 nm. The deep traps located on the boundaries traps electrons and creates space charged fields forms potential barriers. The potential relief reduces carrier ability to diffuse, therefore lower carrier diffusion coefficient. At high carrier excitation addition free carriers screens potential fluctuations and make carrier more mobile. The higher value of diffusion coefficient in the interface region than in front of the sample is observed due to fast electron trapping and therefore deviation from ambipolar carrier diffusion conditions. Since electrons are being trapped more efficiently than holes, electrons become minority carriers and therefore determine higher observed diffusion coefficient. The similar situation, when high carrier diffusion coefficient was deduced for samples with low carrier lifetime and low diffusion coefficient in samples with long carrier lifetime, was described in [77], but explained by different model. The above described feature is not observed in higher quality ULD sample #3 (4.6.b). The carrier lifetimes for the μ–ELO growth of sample #3 are 2.5 times higher compared to standard grown sample #2, what reveals better material quality of sample #3 starting from the first micrometers of sample growth.

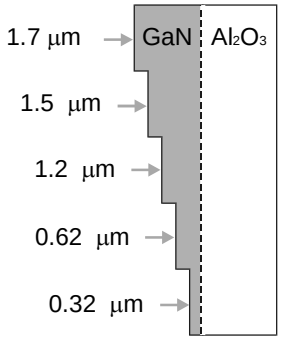

Fig. 4.7. The structure of sample #4.

A step-like etched sample #4 provided the possibility to measure in-depth distribution of samples defectiveness governed carrier lifetime, diffusion coefficient and diffusions length. This GaN/sapphire structure, grown by MOCVD Aixtron planetary reactor, was processed by reactive ion beam etching to obtain steps with different thickness of GaN layer, namely 1.7, 1.5, 1.2, 0.62, and 0.32 μm [73]. The carrier lifetime and diffusion coefficient was determined for each step. We found the carrier lifetime gradually decreasing from 400 ps to 60 ps with decreasing the layer thickness from d_0 to d_5 (Fig. 4.8a), while the diffusion coefficient was nearly constant, D = 1.6 - 1.8 cm^2/s. The resulting diffusion length L_D value varied from 0.26 μm for 1.7 μm-thick layer to 0.1 μm for 320 nm-thick sample (Fig. 4.8b), evidencing gradually improving GaN quality for thicker layers. Determined diffusion length values correlated well with those determined by PL technique for the thinnest steps[78]. The PL technique required measurements of PL intensity at front and back sides of epilayers, therefore it was applicable only for thin layers. These results confirmed that GaN material quality is not constant in the initial growth stage, which results in varying lifetime values what was proposed by early findings. Also it is important to stress that only carrier lifetime is significantly impacted by defect inhomogeneous distribution, while carrier diffusivity is almost constant at all layers.

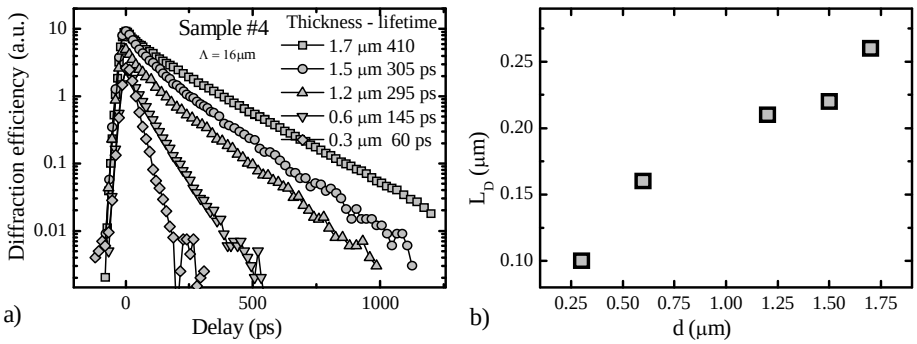

Fig. 4.8. LITG kinetics for GaN layers of different thickness. Grating decay time corresponds to carrier lifetime, as for given period the contribution of diffusion is negligible (a). The diffusion length versus samples thickness for step liked sample #4 (b) [A7].

4.1.2. Investigation of GaN layers grown on SiC and Si substrates

The lack of substrates suitable for GaN epitaxy inspires crystal growers to search for new materials, which could substitute mostly used sapphire. One of possible candidates is silicon carbide (SiC), which lattice constant differs from GaN lattice constant relatively not much. SiC could be suitable since it chemically and physically stable material with wide bandgap transparent for visible light. Unfortunately, there are a lot of difficulties up to now to produce large area crystals and this procedure is still expensive. These disadvantages are not present for silicon (Si). Silicon offers high quality, larger area, and what is most import - cheap substrates. Also the possibility to integrate GaN optoelectronics with matured Si electronics seams very attractive. The main problem of using silicon as substrate for GaN epitaxy is a huge difference in lattice constants. This leads to situation when GaN epilayers grown on Si suffer from huge strain, high density of defects. One of possible way to solve these problems is to use sophisticated buffer layers. In this chapter the results of LITG investigation of GaN grown on SiC and Si will be presented.

The set of analyzed GaN layers on SiC substrates (Samples #5, #6, and #7) was grown by hot-wall MOCVD at T = 1150 ^{o}C[74]. The layers have been produced in a two–step growth mode with 50 nm AlN buffer deposited on the

SiC substrate at slightly higher temperature. Growth parameters such as N-to-Ga gas flow ratio, SiC substrate polytype, and/or off-axis cut orientation have been varied. For this study, three samples of selected grown runs have been analyzed by LITG technique and photoluminescence (PL) techniques.

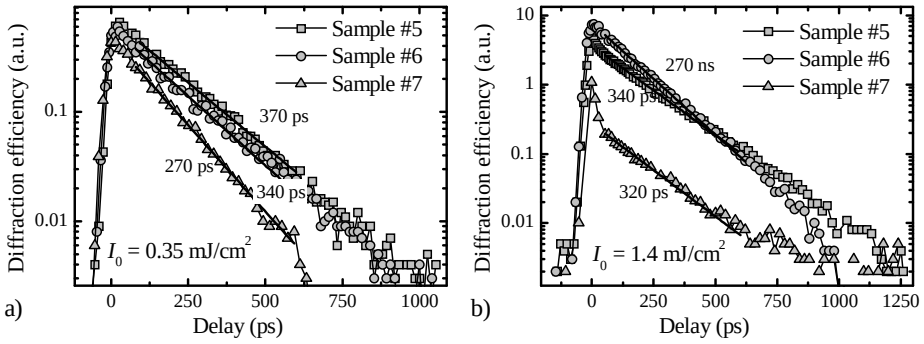

Fig. 4.9. LITG kinetics in three GaN/SiC layers at two different excitation fluences measured at large grating period Λ = 15 μm [A8].

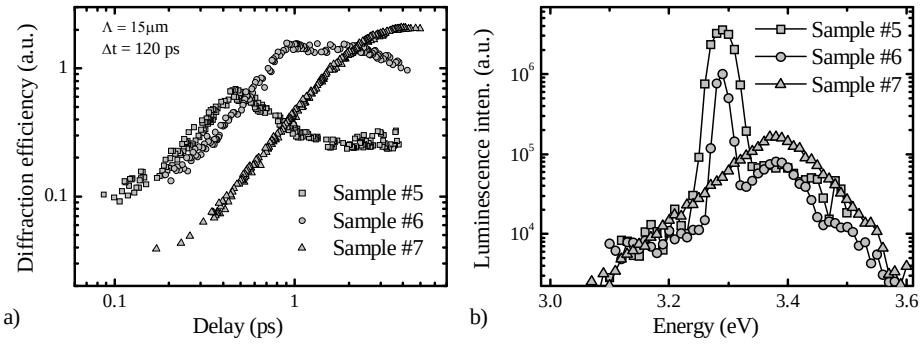

Fig. 4.10. Correlation between the threshold of saturation of diffraction efficiency (a) and photoluminescence intensity (b) in GaN/AlN/SiC heterostructures with varied growth parameters (results obtained by S. Juršėnas et. al.). Exposure characteristics in (a) were measured at 120 ps delay time [A8].

In Fig. 4.9.a,b free-carrier grating kinetics and decay times in three GaN layers of different thickness are shown for the fixed grating period of 15 mm (Samples #5, #6, and #7). Longer decay times usually indicate higher quality of the material, and for the given three epilayers the recombination times do not differ significantly (Fig. 4.9.a). The differences in layer properties are

better revealed at higher excitation fluence (Fig. 4.9.b) when the fast decay component appears in the sample #5 (and partially in #6).

Measurements of exposure characteristics (EC) of diffraction (i.e. dependence of diffraction efficiency η versus excitation fluence I_0 in a wide range of excitations) have shown the clear difference between the layers (Fig. 4.10.a). The substantial decrease of the EC slope indicates the threshold carrier density (or excitation fluence E_s) at which the carrier lifetime drastically decreases. The determined threshold energy values E_s were found to be different for the three layers and correlated well with intensity of stimulated recombination under pulsed excitation measured by PL (see Fig. 4.10b) [79]. This allowed to attribute the observed saturation effect to an onset of stimulated recombination in the degenerate electron-hole plasma. Moreover, the longest carrier lifetime corresponds to the lowest threshold values and indicates the optimized growth conditions for the sample #5, which has the lowest thickness (see Table 4.2.).

Table 4.2. The summary of GaN/SiC samples growth parameters and determined optoelectronic parameters.

No.	Sample	GaN, μm	N-to-Ga flow ratio	τ_R, ps	D_a, cm^2/s	E_S, mJ/cm^2
#5	4H-on axis	0.75	1600	375	1.8	0.5
#6	6H-off axis	1.9	3200	345	2.1	0.9
#7	6H-on axis	2.4	3200	275	1.5	3

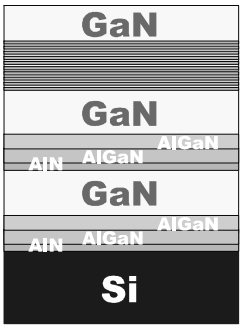

Fig. 4.11. The structure of sample #10.

The similar correlation between carrier lifetime and saturation threshold has been observed GaN layers grown on silicon by Aixtron reactors by MOCVD process. Several $Al_xGa_{1-x}N$ layers with decreasing Al content were used as a buffer layers for all three investigated samples (#8, #9, #10). The Si/SiO/Si structure was used as addition buffer for sample #9. The Sample #10 was grown on a very sophisticated buffer structure (Fig. 4.11.) which consisted of ten periods of GaN/AlN superlattice [75].

LITG kinetics revealed fast carrier recombination at all GaN layers grown on silicon (Fig.4.12). The carrier lifetime varied from 50 ps to 165 ps in investigated samples and was much shorter compared to values obtained for samples grown on sapphire or SiC. The investigations revealed positive effect of using complicated buffers. It was found that carrier lifetime in sample #9 with SiO interlayer is almost 3 times longer compared to sample #8 without with interlayer. Inserting superlattice for strain relaxation further decreased defect density in sample #10, which features the longest carrier lifetime of about 160 ps.

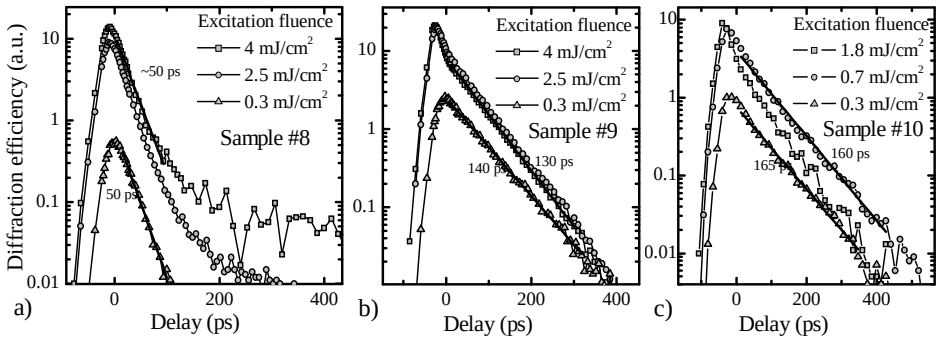

Fig. 4.12. LITG kinetics measured in GaN layers grown on Si at three different excitation levels (Λ= 9 μm).

In spite of the poor crystal quality of GaN/Si samples, the saturation of EC at relatively low excitation fluences showed good conditions for stimulated recombination (Fig.4.13.). The lowest stimulated recombination threshold value of E_s = 0.8 mJ/cm^2 was determined for sample #10 with longest carrier lifetime. On other sample #8 with the simplest buffer structure exhibited highest E_s value around 2 mJ/cm^2. It is worth to note that like for GaN/SiC case the lifetime has tendency to correlate with stimulated recombination threshold.

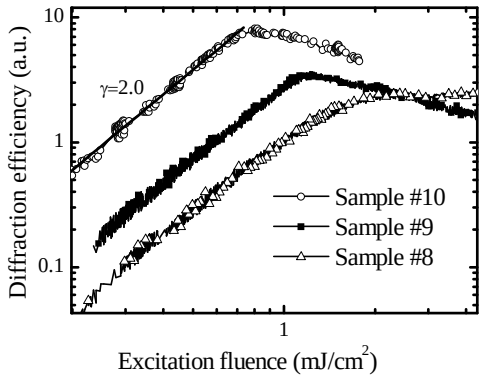

Fig. 4.13. Exposure characteristics measured in GaN/Si samples #8, #9, and #1 measured at 30 ps delay time.

4.1.3. Investigation of HPVE grown GaN

The wider applicability of GaN devices for optoelectronics and electronics limits the lack of native substrate for GaN epitaxy. The layers grown on SiC and Si suffer from high density of defects and stress. The best quality of layers is obtained using growth on sapphire and employing sophisticated ELO technologies. But these layers are still not very suitable for production laser structures. The ultimate goal is to have bulk GaN growth, which unfortunately is up to not reached. The thickest quasi-bulk layers are obtained by using HVPE growth of GaN. HVPE has already proved itself as economically efficient way to grow large volume of material. HVPE layers are grown on sapphire. The freestanding layers are obtained by removing sapphire by laser lift-off technology.

Table. 4.3. The list of HPVE grown samples and their basis properties.

Sample No.	Growth technology	Substrate	Epilayer thickness, μm	TDD, cm^{-2}	Ref.
11	HVPE	Sapphire (removed), free-standing	270	~$2.5 \cdot 10^7$	[80]
12			400	~$5 \cdot 10^6$	[81]
13		Sapphire	10	Not available	
14			17		
15			41		
16			90		
17			145		

The conventional methods of reducing dislocations by thickening in heteroepitaxial system like SiGe/Si were found to be inefficient for GaN/sapphire. The thickness of HVPE grown GaN varies from tens of hundred of micrometers. In this way the HVPE method allowed to reduce dislocation density just by growing thick layers, what allows more self-destructive interaction of dislocations.

The LITG investigation of seven HVPE samples grown by Lumilog, Linkoping University and TDI Inc is presented in this section. 270 mm thick GaN layer (sample #11) was grown on two-step ELO epitaxial lateral overgrown (2S-ELO) GaN template on sapphire. The high structural and optical quality of the grown free-standing crystal was confirmed by a number of characterization techniques and provided the dislocation density of $2.5 \cdot 10^7$ cm^{-2} on Ga-polar face (growth side) [80]. The sample #12 is the thickest and features the lowest dislocation density ($5 \cdot 10^6$ cm^{-2}) of all investigated by our laboratory GaN samples. The set of different thickness samples #13-17 was grown by private company TDI, and was ideal to make investigation on the dependence of material properties versus layer thickness.

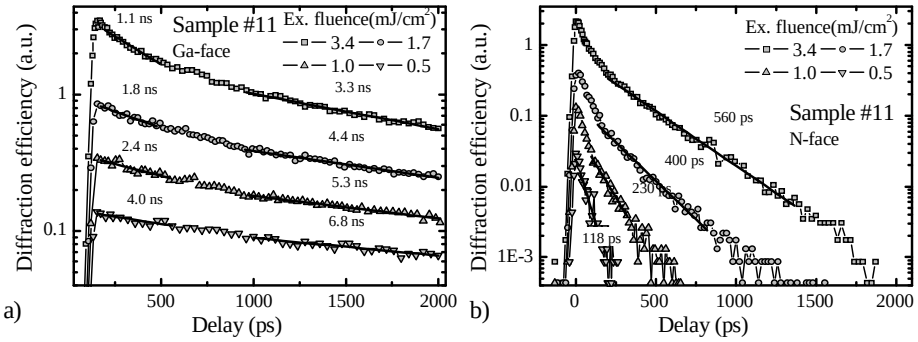

Fig. 4.14. LITG kinetics measured from both sides of HVPE grown GaN sample #11 at several excitation fluences [A6].

LITG kinetics measured in 400 thick HVPE free-standing GaN layer (sample #11) are clearly nonexponential (Fig. 4.14a). The grating decay time become longer with delay time, what means that carrier recombination rate become lower at lower carrier density. At highest used excitation (3.4 mJ/cm^2) the initial grating decay time is around 1.2 ns and it changes to 3.3 at the end of kinetic. The same tendency is valid for all used excitation fluences. Also carrier recombination time is very sensitive to used excitation power. The initial decay time of 4 ns at lowest excitation shortens to 1.1 ns at the highest one, correspondingly in kinetics "tails" grating time changes from 6.8 ns to 3.3.ns. This data indicates that bimolecular recombination is a significant recombination channel in this sample. The exact contribution of bimolecular and linear recombination terms can be calculated only using carrier dynamics modeling, what will be described in Chapter 4.2. Nevertheless, the longest measured carrier lifetime and bimolecular recombination features clearly indicate the superior quality of this sample.

The opposite tendency - carrier lifetime increase with excitation was observed on backside of sample #11(Fig.4.14.b). The same feature was observed in investigation of backsides of several GaN layers grown on sapphire (Fig.4.2, Fig.4.5). Ten times shorter lifetime compared to the growth side of the layer and nonlinear behavior indicates the high defect density at

early stage of growth. It can be deduced that the supreme quality of the front layer is due to large thickness (400 nm) of layer.

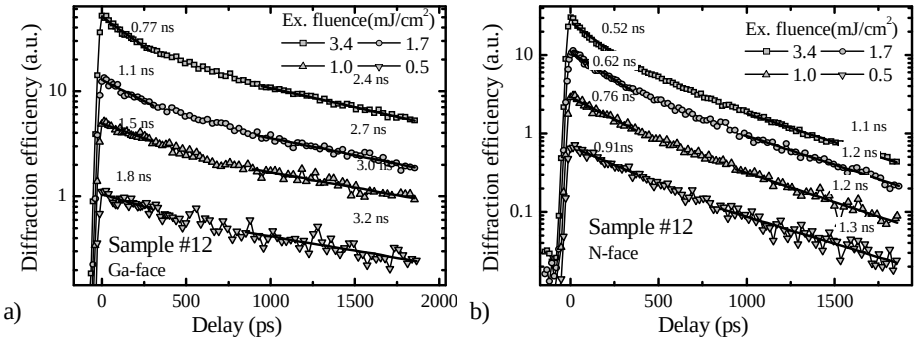

Fig. 4.15. LITG kinetics measured from both sides of HVPE grown GaN sample #11 at several excitation fluences [A6].

Another approach was used for growing sample (#12). To obtain the better initial crystal quality sophisticated 2S-ELO template was grown on sapphire. The results are obvious if to analyze LITG kinetics – both sides of layer have less different carrier recombination lifetime values (difference only 2-3 times) and both sides have features of bimolecular recombination. Since the overall carrier lifetime (~3 ns) of sample #12 is less compared to sample #11(~6 ns) the bimolecular recombination is less pronounced, i.e. carrier lifetime values change with is excitation is smaller. Nevertheless, the crystal quality of initial layer is better for sample #12, the thicker sample #11 has higher carrier lifetime values and lower dislocation density at the front side. This suggests that for HVPE growth reduction of dislocation with layer thickness is important.

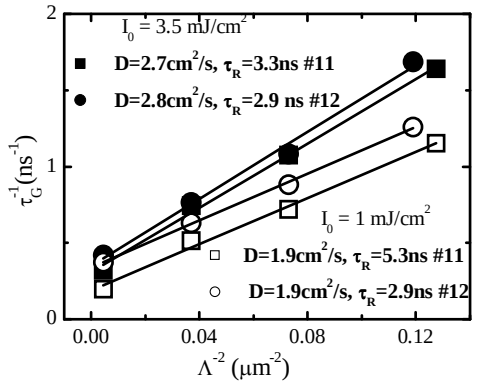

Fig 4.16. The "angular" characteristics measured in samples #11 (squares) and #12 (circles) for high (full points) and low excitation (open points). The calculations of *D* and τ_R are made according formula 2.25.

The measurement of ambipolar diffusion coefficient (Fig.4.16) shows two important features. Firstly, the ambipolar diffusion coefficient value for both HVPE samples is the same for both used excitation fluences, while carrier lifetime and dislocation density differs substantially. This imposes the experimental fact that dislocations are not dominant scattering centers for carriers, at least at room temperature. Secondly, the clear growth of ambipolar diffusion coefficient with excitation fluence can be observed (1.9 cm/s^2 at 1 mJ/cm^2 and 2.8 cm/s^2 at 3.5 mJ/cm^2). This growth was already mentioned for samples #2 and #3 (Fig. 4.4.) and explained as a raise of carrier diffusivity due to degeneracy of distribution of carriers (detail analysis will be given is separated chapter 4.3).

The exposure characteristics measured in samples #11 and #12 showed the decrease of slope with increasing delay time of the probe (Fig.4.17). At zero probe delay the slope of EC was 1.9 indicating band-to-band generation of carriers. At longer delay time slope decrease till 1.5 at 0.5 ns delay, and down to 1.3 at >1 ns delay. This tendency confirms the dominance of bimolecular recombination in these layers.

The important observation is that exposure characteristics do not reach saturation at zero delay what was observed for all MOCVD layers. This means that condition for stimulated recombination are not met at these excitation

levels. The later measurements revealed that values of stimulated recombination in theses layers are about 10 mJ/cm^2. This observation is not expected since experimentally proved high material quality of HVPE layers should be favorable for accumulating high carrier density.

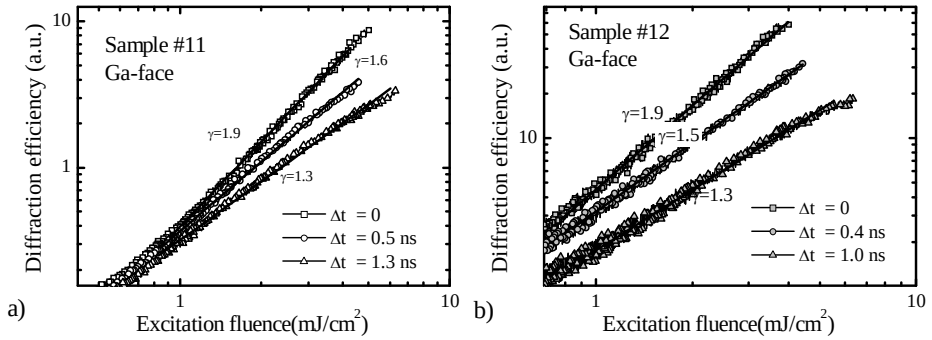

Fig.4.17. Exposure characteristics measured in HVPE grown 400 μm and 270 μm thick GaN layers at three different probe delay values. The gradual decrease of slope γ with time indicates dominance of bimolecular recombination.

The high stimulated recombination threshold in HPVE layers together with high carrier lifetime values allows to reach higher carrier densities compared to MOCVD grown layers, and consequently to observed intrinsic high density regime features such as bimolecular recombination and the increase of diffusivity.

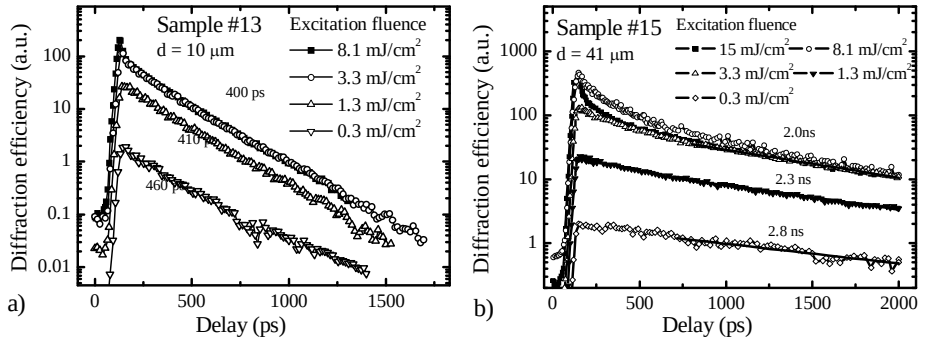

Fig. 4.18. LITG kinetics measured in HVPE grown samples with different layer thickness: (a) – d = 10 μm, (b) – d = 41 μm. Large grating period Λ = 11 μm was used [A1].

The investigation of a set of samples (#13-17) with different samples thickness (10 – 150 μm) provided by one company was excellent possibility to explore how photoelectrical parameters depend on HPVE sample thickness. Firstly, LITG kinetics at high grating period was measured at several excitation fluences in order to investigated carrier recombination mechanisms (Fig.4.18). The thinnest layer #13 exhibited quite short carrier lifetime values (~400 ps) for all used excitation and stimulated recombination features at 3.3 mJ/cm^2. These results would be typical for MOCVD grown layers, but are quite low for HVPE grown sample (stimulated recombination was not observed for previously explored HPVE at all), but low quality of this sample was could be explained due to small layers thickness. The kinetics in 41 μm thick sample shown that carrier lifetime in this layers is ~5 time longer compared to sample with d = 10 μm. The clear bimolecular recombination features could be observed (nonexponential kinetics with decreasing lifetime at higher excitation). Also, trace of fast stimulated recombination at the beginning of kinetic is observed only for highest I_0 = 15 mJ/cm^2 excitation. This shows that stimulated recombination threshold is higher compared to sample #13.

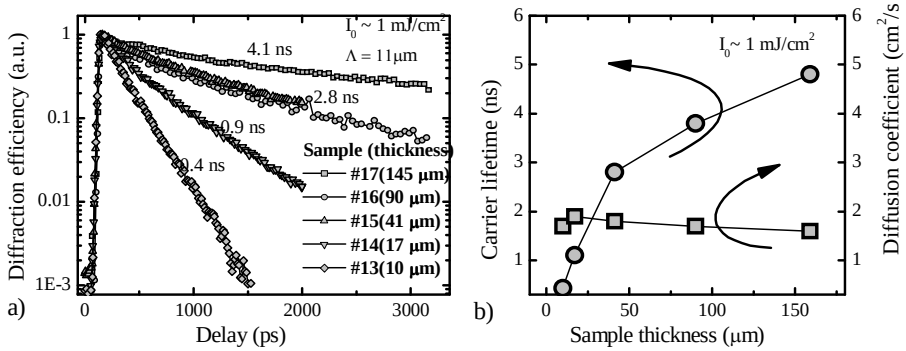

Fig.4.19. LITG kinetics measured in a set of different thickness HVPE grown samples (a). The dependence of carrier lifetime and ambipolar diffusion coefficient on sample thickness [A1].

In Fig.4.19 a and b one can see how carrier lifetime increases with sample thickness. The carrier lifetime difference is ten times if to compare the thickest and thinnest samples. This supports the approach of reduction of dislocation

density by increasing thickness of HVPE layers. On other hand, this set of data also shows that carrier diffusion coefficient is not sensitive to change of dislocation density, since it is constant for all five layers. Most probably the lattice scattering is a dominant mechanism at room temperature, and dislocation related scattering is relevant only at lower temperatures (See Chapter 4.2).

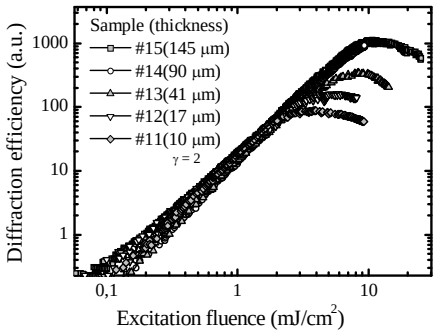

Fig.4.20. The exposure characteristics measured in a set of different thickness HVPE grown samples. The delay of probe versus excitation pulse was ~30 ps.

Finally, the measurements of exposure characteristics revealed that stimulated threshold correlates with sample thickness (Fig.4.20). The thicker the sample the higher stimulated threshold is observed.

4.1.4. Concluding summary

Table. 4.4. Summary of dislocation density dependent photoelectric parameters of GaN layers.

Sample No	Growth technology	Thickness (μm)	N_{TD} (cm^{-2})	τ_R (ns)	D_a (cm^2/s)	L_D (μm)	E_S (mJ/cm^2)
1.	MOCVD/Al_20_3	2.6	10^9	0.7	1.7	0.34	~1
2		3-4	$5\cdot10^8$	0.9 - 1.1	1.7-1.8	0.42	2
4		0.3 .. 1.7	N/A	0.06 -0.42	1.7-1.8	0.1..0.26	1.5
5-7	MOCVD/SiC	0.75-1.9	$>10^{9}$ *	0.37- 0.34	1.8-2.1	~0.25	~1
8-10	MOCVD/ Si	0.75-1.2	$>10^{9}$ *	0.05-0.16	~1.6	0.16	~1
3	μ-ELO	10	$5\cdot10^7$	2.7	1.8-2.4	0.8	3
11	HVPE	270	$2.5\cdot10^7$	2.9	1.9-2.9	0.7 - 0.9	~10
12		400	$5\cdot10^6$	3.3 - 5.2	1.9-2.7	0.94 -1	~10
13-17		10 .. 150	~10^{7} *	0.4 - 4.8	1.8-2.5	0.27..0.93	3..10

*The typical TTD values for corresponding growth technology.

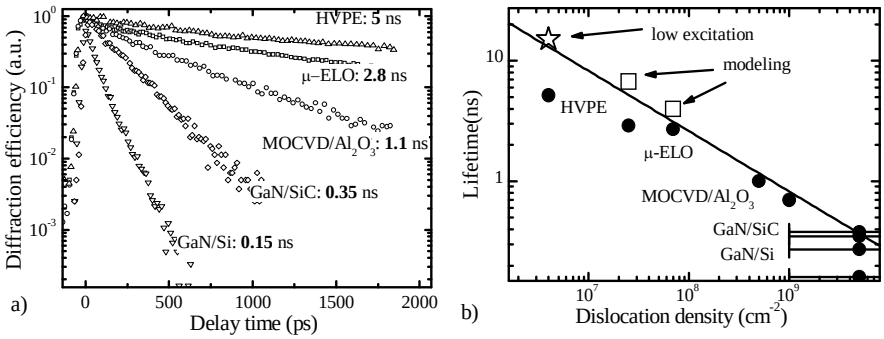

Fig.4.21. The LITG kinetics measured in GaN layers show how carrier lifetime changes with growth technology (measurements were done at large grating period, $\tau_R << \tau_D$) (a). Carrier lifetime as a function of threading dislocation density in GaN layers in high excitation (full points). The open points are obtained by low excitation (star) or discrimination of radiative and nonradiative lifetime by carrier dynamics modeling (squares) (b) [A6, A9].

The table 4.4. summarizes the photoelectrical parameters of differently grown GaN layers, determined by the LITG technique. It shows that carrier lifetime is varying by two orders of magnitude (50 ps to 5.2 ns), carrier diffusion coefficient being almost constant and consequently carrier diffusion length in rage of 0.1 – 1 μm for samples with varying dislocation density. This investigation confirms the role of dislocation as carrier recombination centers, and shows that carrier lifetime very sensitively reflects material quality (Fig.4.21a). Using these data, the dependence of carrier lifetime versus dislocation density has been plotted (Fig.4.21b). In high TD range ($N_{TD}>10^8$ cm^{-2}) the carrier lifetime is governed by nonradiative recombination at dislocation, thus the dependence is strong $\tau_R \propto (N_{TD})^{-0.5}$. In a low TD range ($N_{TD}<10^8$ cm^{-2}), the dependence is weaker. The saturation is caused by intrinsic bimolecular carrier recombination mechanism, which shortens carrier lifetime in samples with low dislocation density if carrier densities are high.

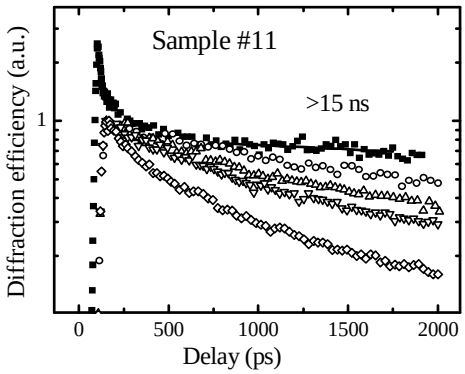

Fig. 4.22. Normalized LITG kinetics measured in HVPE grown GaN sample #11 at high excitation (open points, the same as in Fig. 4.12) and low excitation kinetic (full points) measured at two photon excitation by 532 nm light [A10].

To avoid the presence of bimolecular recombination the low excitation LITG measurements were carried out on thickest #11 sample. The grating was recorded by two-photon absorption of 532 nm light and created carrier density around 10^{16} cm^{-3}, thus, decreasing the probability of bimolecular recombination. The LITG kinetics at large grating period (Fig.4.22) revealed large than 15 ns grating decay time which we assign to dislocation governed

carrier lifetime. The value of 15 ns prolongs the strong dependence of carrier lifetime versus dislocation density observed in high TD range (Fig.4.21 opens star). Moreover, by carrier dynamics modeling described in Chapter 4.2 we discriminated the impacts of radiative ant nonradiative carrier lifetimes. After we put nonradiative recombination lifetime (Fig. 4.21 open squares) values into plot the dislocation determined nonradiative recombination can be described by empirical function $\tau[ns] = \frac{2.6 \cdot 10^4}{\sqrt{N_{TD}[cm^{-2}]}}$ in whole investigated dislocation density range . Since the average distance between dislocations is proportional to $1/\sqrt{N_{TD}}$, the obtained result shows that carrier recombination time is proportional to the average distance between dislocation, and this confirms the model of dislocation governed carrier recombination.

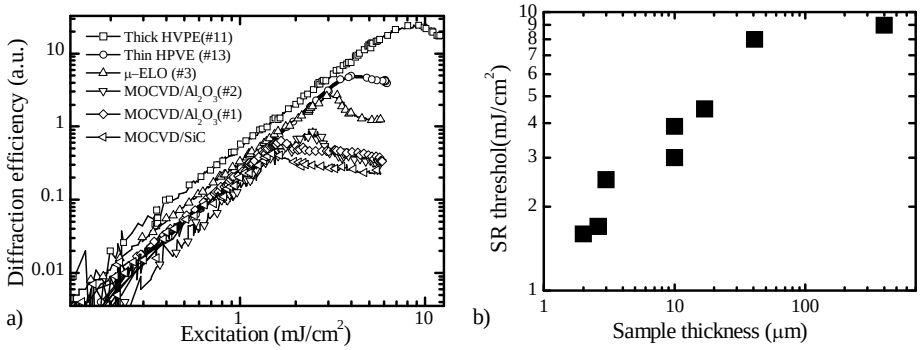

Fig. 4.23. The exposure characteristics of LITG measured in differently grown GaN layers with 30 ps delay of the probe beam (a). The dependence of stimulated recombination threshold on sample thickness (b) [A6].

The measurements of LITG exposure characteristics (Fig.4.23a) showed that stimulated recombination threshold correlates with samples thickness (Fig.4.24b) as well as with dislocation density. The lowest stimulated recombination threshold value of about 1 mJ/cm^2 was observed for thinnest GaN/sapphire, GaN/SiC, and GaN/Si layers, while with increasing layer thickness stimulated recombination threshold increased up to 10 mJ/cm^2 for several hundred μm thick HVPE grown layers. The exact reason is not discovered, but preliminary we attribute this effect to light propagation

properties rather than to carrier dynamics. The thin layers of GaN are optically more homogenous, therefore, scatters the light less. Also, the energy density of stimulated emission is higher in thin layer rather than in a thick one, since optical mode spread into bulk of the sample.

Investigations described in this Chapter 4.1 opened two questions concerning the carrier density dependent recombination and diffusion. The deeper analysis of bimolecular recombination and diffusion at high carrier densities will be given in the next two Chapters.

4.2. Low temperature studies of carrier dynamics in GaN

The given Chapter extends the investigation of nonequilibrium carrier dynamics in GaN layers to low temperatures, where a number of processes (e.g. bimolecular recombination rate, carrier scattering) are temperature dependent and contribute, in addition to dislocation related defects, to the carrier plasma parameters in highly excited GaN layers. The low temperature investigations were stimulated by observation of bimolecular recombination features at room temperature. According to the theory, the bimolecular recombination coefficient rises with decreasing temperature as $B \propto T^{-1.5}$[82], therefore radiative recombination should be more efficient channel than the defect related nonradiative one at low temperatures.

4.2.1 Experimental results

For low temperature studies three samples #2, #3, and #12 (see Table 4.1) with different dislocation density were chosen. A 3 μm thick sample #2 with dislocation density around $5 \cdot 10^8$ cm^{-2} was grown by standard MOCVD process. Sample #3 - a 10 μm thick μ–ELO layer with dislocation density of about $N_D \leq 5 \cdot 10^7$ cm^{-2}, and 400 μm-thick freestanding HPVE layer with very low dislocation density in mid-10^6 cm^{-2}. As was shown in a previous Chapter these three layer exhibited different recombination time values ranging from 1.2 ns in the sample #2 to 5.2 ns in HVPE layer #12.

The LITG experiment were carried out in the temperature range T = 9 - 300 K. Low temperatures were achieved by closed cycle helium cryostat. Nonequilibrium carrier gratings ($\Delta N \sim 10^{19}$ cm^{-3}) have been created by interband transitions under excitation at 351 nm by 7 ps duration laser pulses and probed at 1054 nm. The grating kinetics at its various periods Λ and excitation energy I_0, as well the exposure characteristics of LITG ($\eta = f(I_0)$) have been measured in order to study defect-density and carrier-density dependent carrier recombination peculiarities and transport in a wide temperature range.

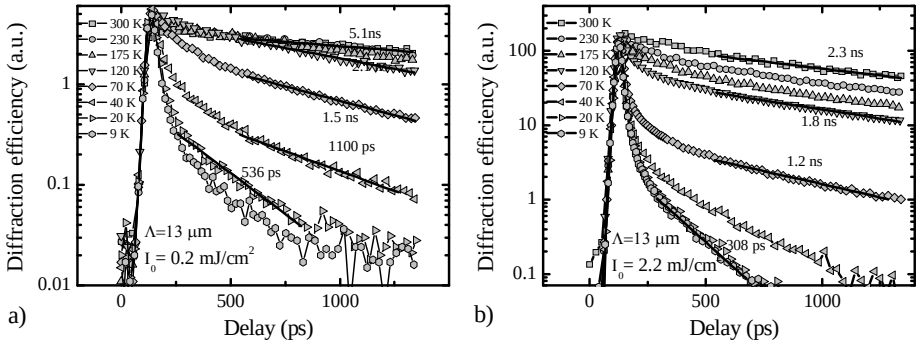

Fig. 4.24. LITG kinetics in low dislocation density HVPE sample #12 measured in temperature range form 9 K to 300 K at low (I_0 = 0.2 mJ/cm^2) (a) and high (I_0 = 2.2 mJ/cm^2) (b) excitation fluence [A9].

The set of kinetics in sample #12 in temperature range from 9 K to 300 K is shown in Fig.4.24. It can be seen that lowering the temperature increases the recombination rate of excited carriers, and, therefore, LITG kinetics become faster. At lower temperatures (T < 120 K) the kinetics shape becomes strongly nonexponential, indicating the dominance of bimolecular recombination, as it is expected since bimolecular recombination coefficient sharply increases while lowering the temperature $B \propto T^{-3/2}$ [82]. These features are observed for both high and low excitation for HVPE sample #12. Of course, for lower excitation the clear nonexponential shape is observed for lower temperatures compared to high excitation case, where it is seen already at room temperature.

The non-exponential shape of measured diffraction kinetics is caused not only due to nonlinear recombination but also due to carrier diffusion into bulk of sample. The in-depth diffusion flattens carrier density profile therefore reduces average carrier density and recombination rate of bimolecular recombination. Therefore, quantitative description of carrier dynamics is possible only by solving two dimensional carrier continuity equations.

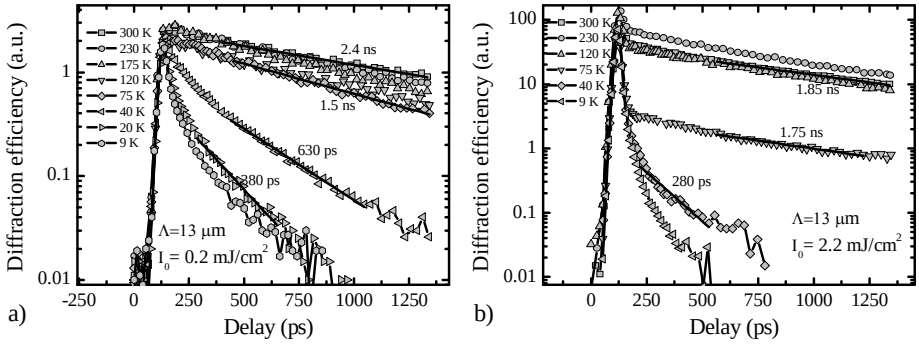

Fig. 4.25. LITG kinetics in μ-ELO sample #3 measured in temperature range form 9 K to 300 K at low (I_0 = 0.2 mJ/cm^2) (a) and high (I_0 = 2.2 mJ/cm^2) (b) excitation fluence [A9].

A little bit different situation is in the μ-ELO sample (Fig.4.25). At high excitation the fast component caused by stimulated recombination is observed, while reducing the temperature this fast part of kinetic becomes more pronounced what shows that stimulated recombination threshold is lower at low temperatures. The stimulated recombination reduces (limits) carrier density and, therefore, kinetics are not so non-exponential as in HVPE sample case. Nevertheless, low excitation kinetics exhibit gradual decrease of lifetime with lowering the temperature and nonexponential kinetic shape, what shows that bimolecular recombination is present in this sample also.

The kinetics measured in standard high dislocated MOCVD layer #2 (Fig.4.26) are single exponential for all measured temperatures and excitation fluences. The features of bimolecular recombination can be seen only in tendency of a slight decrease of carrier lifetime with lowering the temperature, but nonradiative recombination mechanism is a dominant and therefore decay

kinetics are single exponential in measured time domain. The stimulated recombination threshold decreases with temperature similarly to μ-ELO sample, what can be seen in increasing amplitude of the fast part of kinetics and also more evidently from exposure characteristics measured just after excitation pulse (Fig. 4.27a).

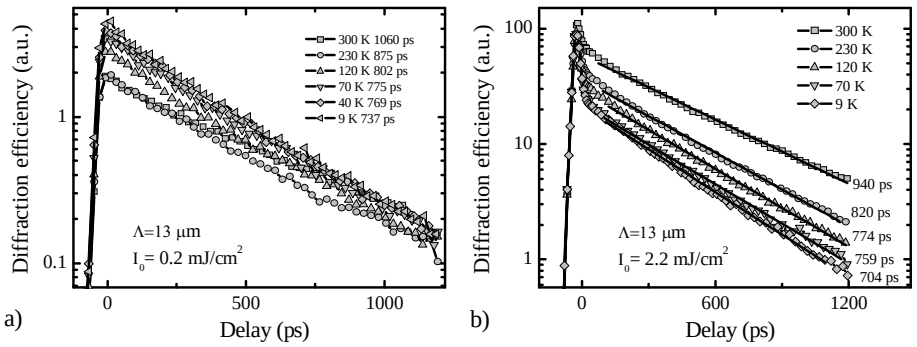

Fig. 4.26. LITG kinetics in standard MOCVD sample #2 measured in temperature range form 9 K to 300 K at low (I_0 = 0.2 mJ/cm^2) (a) and high (I_0 = 2.2 mJ/cm^2) (b) excitation fluences.

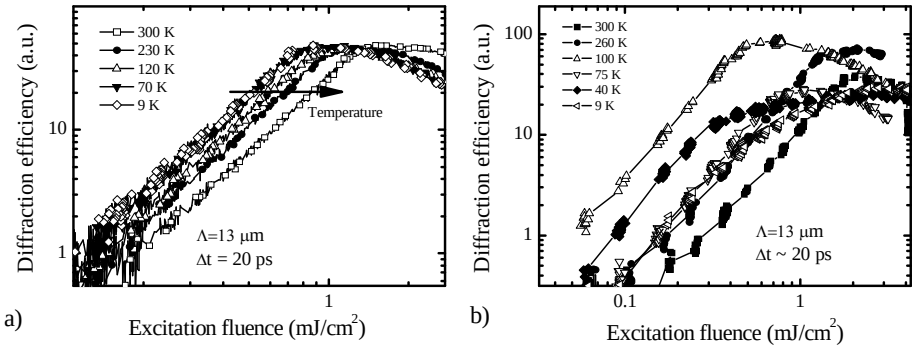

Fig. 4.27. LITG exposure characteristics measured in standard MOCVD sample #2 (a) and μ–ELO sample #3 (b) in temperature range form 9 K to 300 K [A9].

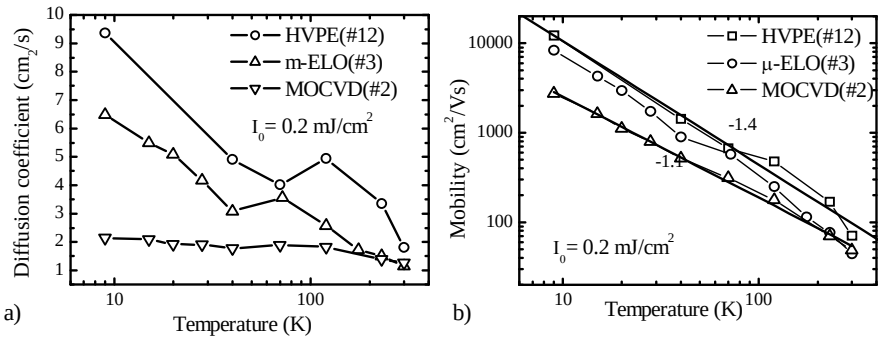

Fig. 4.28. The dependence of carrier ambipolar diffusion coefficient (a) and mobility (b) in temperature range form 9 K to 300 K measured in samples #2, #3, and #12 [A9].

The LITG kinetics at several grating periods were measured and ambipolar diffusion coefficient was determined for temperature range 9 –300 K (Fig.4.28a). Using determined diffusion coefficient and Einstein relationship $\mu = De/kT$ the carrier mobility was calculated for three samples (Fig.4.28b). The slope value -1.4 for HVPE and μ-ELO samples indicates that carriers are scattered mainly by acoustic phonons[83] in all investigated temperature range. The standard MOCVD sample with higher dislocation density exhibit lower slope and lower absolute mobility values, indicating enhanced carrier scattering probability.

4.2.2 Modeling

We performed numerical modeling of carrier dynamics and were able to fit the measured LITG kinetics and exposure characteristics. In this way we confirmed the simple model of carrier recombination, which includes linear (defect related) and quadratic (bimolecular) recombination terms. The numerical modeling allowed experimentally to determine bimolecular recombination coefficient and its temperature dependence. Also, numerical solution of carrier continuity equation illustrates how carriers diffuse into bulk of the sample during experimental time domain, and, therefore, illustrates which depth of the sample is investigated.

The carrier dynamics in photoexcited by interference pattern semiconductor crystal is well described by *one*-dimensional model, if the in-depth distribution of carriers is negligible, i.e bulk excitation. However, under the strong absorption the carrier density profile has large gradients along the sample thickness, therefore, a *two* dimensional model has to be employed [84]. According to this model, the two-dimensional carrier density N(x,z,t) in a layer of finite thickness d is described by the equation:

$$\frac{\partial N(x,z,t)}{\partial t} = \nabla\left[D\nabla N(x,z,t)\right] - \frac{N(x,z,t)}{\tau_R} - BN^2(x,z,t) + G(x,z,t), \qquad (4.1)$$

with boundary conditions:

$$\left.\frac{\partial N(x,z,t)}{\partial z}\right|_{z=o} = \frac{S_1}{D}N(x,0,t), \qquad \left.\frac{\partial N(x,z,t)}{\partial z}\right|_{z=d} = -\frac{S_2}{D}N(x,d,t), \qquad (4.2)$$

where B is the bimolecular recombination rate, S_1 and S_2 are surface recombination velocities at the front and back surfaces. G(x,z,t) is carrier generation function, which is equal to

$$G(x,z,t) = \frac{I_0\alpha}{h\nu}(1-R)(1+\cos(2\pi x/\Lambda))\exp(-\alpha z)\cdot\frac{2\sqrt{\ln(2)}}{\tau_{las}\sqrt{\pi}}2^{\frac{-4(t-t_0)^2}{\tau_{las}^2}} \qquad (4.3)$$

where α is absorption coefficient for excitation beam, I_0 – excitation fluence, $h\nu$ – the energy of exciting photon, R – reflection coefficient, and τ_{las} –duration of laser pulse at FWHM. The carrier continuity equation (4.1) is solved by numerical finite difference time domain procedure and provides the spatial-temporal distribution of carriers N(x, z, t).

Since during LITG experiment the first order of diffraction is detected the first harmonic of carrier modulation is calculated:

$$N_1(z,t) = \frac{2}{\Lambda}\int_{-\Lambda/2}^{\Lambda/2} N(x,z,t)\cos\left(\frac{2\pi x}{\Lambda}\right)dx. \qquad (4.4)$$

Using harmonically modulated carrier density the refractive index modulation $\Delta n(z,t) = n_{eh}N_1(z,t)$. By integrating over sample thickness the total phase modulation and instantaneous diffraction efficiency η is calculated:

$$\eta^*(t) = \left(\int_0^d \frac{\pi \Delta n(z,t)}{\lambda} dz \right)^2 \qquad (4.5)$$

Since the probe is not delta function, but has finite duration of (τ_{las} = 25 ps), the fast part of carrier kinetics is slightly averaged by probing. Therefore, integration over probe duration should be performed:

$$\eta(t) = \frac{2\sqrt{\ln(2)}}{\tau_{las}\sqrt{\pi}} \int_{-\infty}^{\infty} \eta^*(t - tt) 2^{\frac{-4tt^2}{\tau_{las}^2}} dtt \,. \qquad (4.6)$$

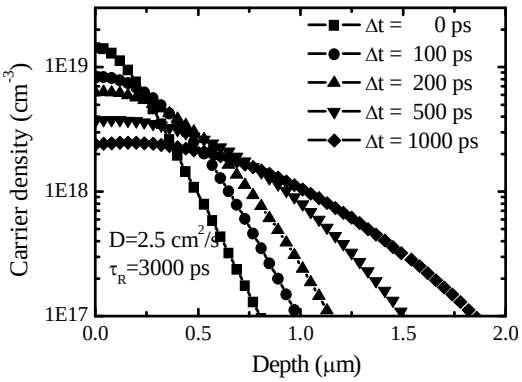

Fig. 4.29. The calculated in-depth profiles of carrier density at grating peaks are shown for several delay times, indicated on the plots. The parameters used for calculations are the following: D =2.5 cm^2/s, τ_R = 3 ns, I_0 = 1 mJ/cm^2, Λ = 10 μm, α = 7·10^4 cm^{-1}, d = 10 μm.

The Fig. 4.29 illustrates the calculated carrier density in-depth profiles. As one can see the decay of carrier density (also recombination rate, if bimolecular recombination is considered, since τ_{Rad} = 1/BN) is governed not only by carrier recombination, but also because of diffusion-governed in-depth carrier redistribution, which increases excitation depth and decreases carrier density. Therefore the complete two-dimensional modeling should be accounted in order to model observed non-exponential kinetics. Another important information, which follows from the modeling, is thickness of investigated layer by LITG. From calculated profiles it is clear that diffusion increases the excitation depth up to 1 – 2 μm during experimental time domain (2 ns).

The fitting procedure of measured LITG kinetics was performed by varying only bimolecular recombination and linear recombination lifetime values, since others parameters were estimated experimentally (D, I_0, R, $h\nu$, etc) or taken from the published papers in a literature (α). The value of the surface recombination velocity was kept equal to zero, since LITG experiments exhibit single exponential kinetics for many GaN samples, which means that surface recombination is negligible. Using described model and varying with temperature only bimolecular recombination coefficient we were able to fit the measured diffraction kinetics for HVPE at 0.2 and 0.7 mJ/cm^2 excitation fluences (Fig. 4.30).

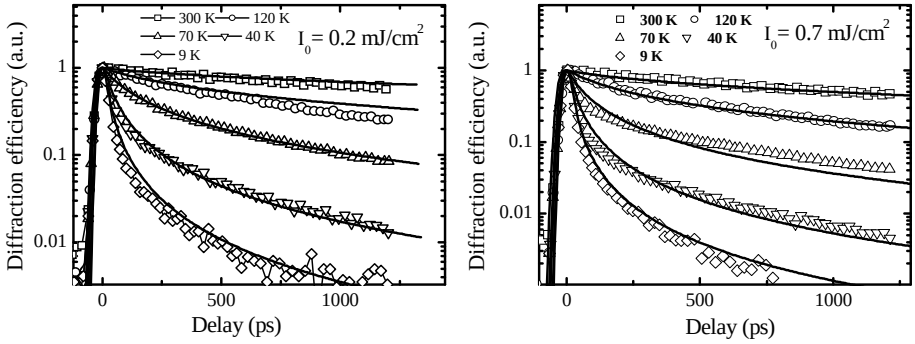

Fig. 4.30. LITG kinetics in low dislocation density HVPE sample #12 measured in temperature range form 9 K to 300 K at low (I_0 = 0.2 mJ/cm^2) (a) and middle (I_0 = 0.7 mJ/cm^2) (b) excitation fluence. Points correspond to experimental data, and lines – to numerical fitting [A9].

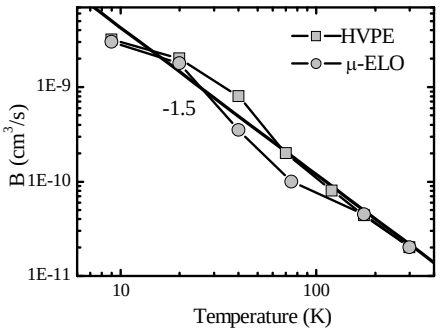

Fig. 4.31. The determined bimolecular recombination coefficient values for GaN. The fitting curve shows the slope value of –3/2, predicted theoretically [A9].

In Fig.4.31 the dependence of bimolecular recombination coefficient B is presented, which we obtained by numerical fitting. The slope B versus T dependence is equal to –1.5 and confirms the theoretically predicted law $B \propto T^{-1.5}$ [82, 85]. The fitting provided values of B at room temperature $B = 2 \cdot 10^{-11}$ cm^3/s at 300 K and $3.2 \cdot 10^{-9}$ cm^3/s at 10 K. The B value at 300 K is very close to the one determined by TRPL technique, $B = 2.4 \cdot 10^{-11}$ cm^3/s[86], which was derived from excitonic lifetime measurements. Nevertheless, it is worth to stress that LITG technique allowed straightforward determination of B from the measured nonexponential carrier recombination kinetics in wide temperature range and it is done for the first time in GaN.

The similar independent fitting was done with the data obtained for the μ-ELO sample (Fig.4.32). The B values obtained by fitting these data (plotted in a Fig. 4.31) are very closed to values obtained from previous measurements. We note that the taking into account the bimolecular recombination process allowed us to estimate more correct values of nonradiative recombination time in μ-ELO sample $\tau_R \approx 4$ ns.

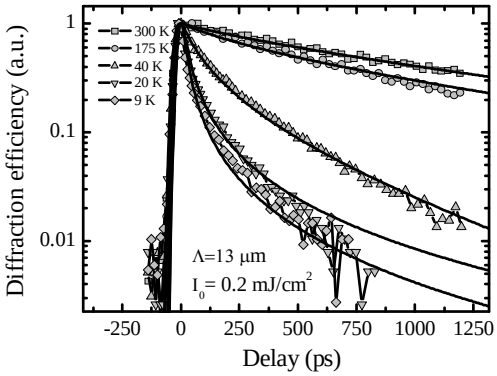

Fig. 4.32. LITG kinetics in μ-ELO sample #3 measured in temperature range form 9 K to 300 K. Points correspond to experimental data, and lines – to numerical fitting [A9].

The model was also explained the exposure characteristics measured in HVPE sample (Fig.4.33). The experiments showed the gradual decreases of exposure characteristic slope from $\gamma = 2$ at room temperature to $\gamma = 1$ at low

temperatures. The modeling curves nicely fitted with experiment and confirmed that bimolecular recombination is responsible for reduction of the slope.

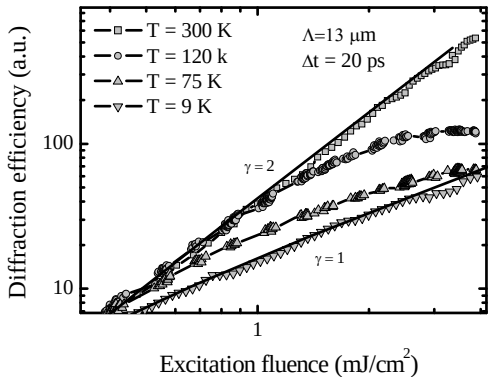

Fig. 4.33. LITG exposure characteristics in low dislocation density HVPE sample #12 measured in temperature range form 9 K to 300 K at probe delay time equal to 20 ps. Points correspond to experimental data, and lines – to numerical fitting [A9].

4.2.3 Conclusions

It has been shown that LITG at low temperatures and subsequent modeling allowed us to determine directly the values of the bimolecular recombination coefficient *B* and its temperature dependence, to separate radiative and nonradiative recombination. The measurements of diffusion coefficient in wide temperature range allowed to identify carrier scattering mechanisms.

4.3. Diffusion of carriers in GaN at high excitation conditions

The light induced transient grating technique is used to study carrier dynamics in semiconductors since it provides a unique possibility to separate carrier diffusion and recombination processes. The carrier dynamics at low excitation energy density or in highly-dislocated GaN provided nearly exponential grating decay times, determined by linear carrier recombination and in-plane diffusion [87]. The nonlinear transients in GaN are caused due to nonhomogenous distribution and/or saturation of traps [88], bimolecular

recombination at high carrier densities or low temperature [89]. In this Chapter the LITG measurements in high structural quality GaN layers which reveals the features of an intrinsic crystal - carrier-density dependent recombination and *diffusion will* be presented. The carrier density dependent diffusion was observed in GaAs an explained with the assumption of Fermi pressure as the dominating driving force for plasma transport[84, 90]. These experiments for the first time directly show the carrier diffusion with non constant diffusivity in GaN.

The experimental details were the same as in experiments described in previous Chapter 4.1 and 4.2. For determination of carrier density dependent diffusion, LITG experiments were carried out at different excitation fluences (0.34 –2.7 mJ/cm^2) and grating periods Λ values (2.7 to 11.4 μm). The small grating period 2.7 μm ensures the fast diffusion process $\tau_D = \Lambda^2/4\pi^2 D < 1$ ns for typical diffusion coefficient value in GaN. As recombination time of carriers in high quality GaN layers are higher than several ns, thus LITG kinetics at such low grating periods corresponds to diffusive decay of the grating. The detailed analysis was done for measurements obtained at room temperature, but proposed carrier dynamics model was confirmed by measurements made at low temperatures (9 – 300 K). Carrier dynamics was studied in HVPE grown 80 μm thick GaN layer on sapphire [91] .

4.3.1 Experimental results

The modulated part of free carrier concentration ΔN decays because of carrier recombination and in-plane diffusion by exponential law with characteristic grating decay time [53]:

$$\frac{1}{\tau_G} = \frac{1}{\tau} + \frac{1}{\tau_D} = \frac{1}{\tau} + \left(\frac{2\pi}{\Lambda}\right)^2 D \qquad (4.7)$$

Therefore, measurement of grating decay times τ_G at several different grating periods Λ allows independent measurement of carrier lifetime τ and diffusion coefficient *D*. The measured LITG kinetics (Fig. 4.34a) was non-

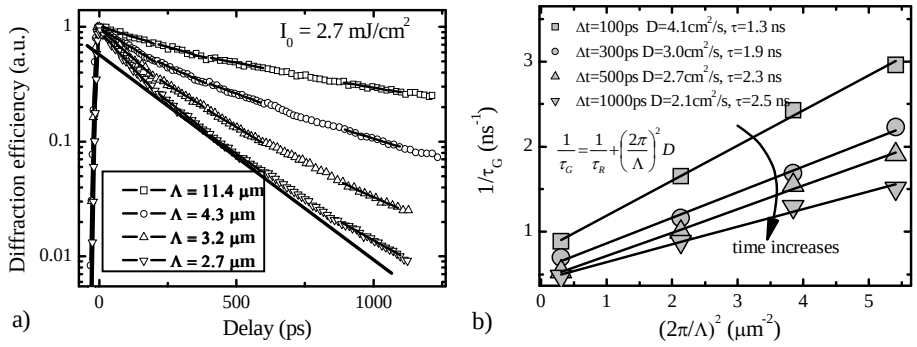

Fig. 4.34. The *non-exponential* LITG kinetics at different grating periods (a) at the largest excitation used (2.7 mJ/cm^2). Open points correspond to experimental data, the lines – exponential fit for determination of grating decay times at different periods and different delay times. The straight line shows nonexponential shape of small grating period kinetic indicating non-constant value of carrier diffusion coefficient. The angular characteristics at different delay values are shown in figure (b). The determined instantaneous values of carrier lifetime τ and ambipolar diffusion coefficient D at different delay values Δt are shown in a legend [A11].

exponential at large and at small grating periods suggesting non-constant carrier recombination and diffusion rates. Therefore we calculated grating decay time τ_G at several delay values Δt and plotted the inverse decay time $1/\tau_G$ versus $(2\pi/\Lambda)^2$ (Fig. 4.34b) according (4.7) relationship. We note that for the fixed time intervals we assume the nearly exponential decay, therefore, a linear fit provided the instantaneous D and τ values. We found that the instantaneous values of ambipolar diffusion coefficient D and lifetime τ were varying during grating decay. For the largest used excitation fluence I_0 = 2.7 mJ/cm^2, the D value varied from 4.1 cm^2/s (at the highest carrier density) till 2.1 cm^2/s at 1 ns time delay (Figs. 4.34b, 4.35). At these conditions, the instantaneous recombination time was also varying with time, from 1.3 ns to 2.5 ns (Fig. 4.34b). To verify if this is a dependence on carrier density the similar measurements were carried out at lower excitation energies (down to 0.34 mJ/cm^2). The experiments confirmed that at lower carrier density the ambipolar diffusion coefficient D becomes smaller, while carrier lifetime increases (Table 4.5). At the lowest excitation intensity LITG kinetics become exponential, therefore we observed constant D and τ values (Fig.4.35a and b).

These findings pointed out that carrier diffusion coefficient and lifetime depend on the carrier density in highly excited GaN, if these processes are not masked by fast nonradiative recombination.

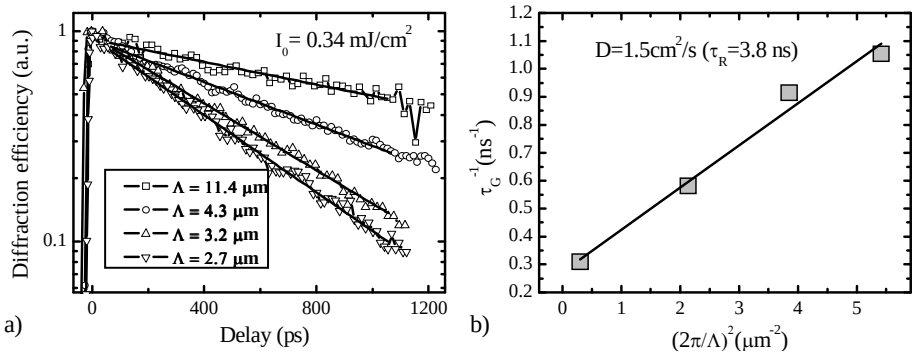

Fig. 4.35. The *exponential* LITG kinetics at different grating periods at the *smallest* excitation used (0.34 mJ/cm^2) (a). The plot of inverse grating decay time versus the square of inverse grating period was used to calculated carrier lifetime τ and ambipolar diffusion coefficient D at small carrier density (b) [A11].

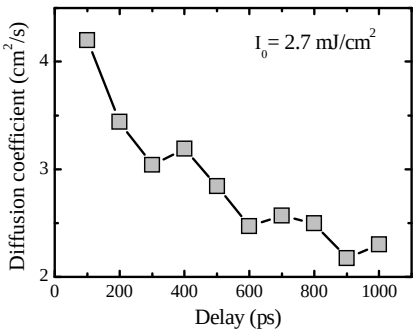

Fig. 4.36. The ambipolar diffusion coefficient value determined at various delay times after photoexcitation of carriers at the largest fluence used I_0 = 2.7 mJ/cm^2 [A11].

Table 4.5. Carrier diffusion coefficient and lifetime values at different excitation fluences. The arrows (→) indicate the gradual change of value with delay time increasing.

Excitation (mJ/cm^2)	$D(cm^2/s)$	τ(ns)
0.34	1.5	3.8
0.7	1.8→1.6	2.4→3.7
1.4	2.6→1.8	1.7→2.7
2.7	4.1→2.1	1.3→2.5

4.3.2 Modeling

The dependence of carrier lifetime on carrier density in GaN at high excitation condition was observed and explained in a previous Chapter as bimolecular recombination [89], while the dependence of diffusion coefficient on carrier density was observed for others samples (see Chapter 4.1, samples #3,#11,#12 and others) but analyzed yet. As the main effect resulting in a density-dependent diffusivity, we consider the so-called *Fermi pressure*. It originates from the fact that for sufficiently high densities, i.e., with the onset of degeneracy, Pauli's exclusion principle needs to be considered and the free energy is significantly higher than it would be in a classical gas. The enhancement of free energy Φ depends on the carrier density *n* and therefore on the volume V. This can be interpreted as a pressure: $p = \partial\Phi/\partial V$. The quantitative description [92,] [83, p. 29] could be summarized to generalized Einstein relation:

$$D(N) = \frac{\mu kT}{e}\frac{F_{1/2}(\eta)}{F_{-1/2}(\eta)} \qquad (4.8)$$

At high carrier density ratio between carrier diffusion coefficient and mobility depends on carrier density since Fermi integrals does not cancel each other like in classical (non-degenerated) electron/hole gas case.

During the LITG experiment the excited carrier density is nonhomogenous (both into samples depth, and along grating vector), therefore

measured diffusion coefficient values at different delays can not be assign to a certain carrier density values. To verify if carrier degeneracy can explain the observed diffusion coefficients variation we performed numerical modeling of carrier dynamics at experimental excitation conditions. We solved the two-dimensional carrier continuity equation, which includes interband photoexcitation, linear and nonlinear (bimolecular) carrier recombination with coefficient *B* (the same equation as Chapter 4.2) and diffusion at degenerated plasma regime, i.e. carrier density dependent diffusion coefficient:

$$\frac{\partial N(x,z,t)}{\partial t} = \nabla\left[D(N)\nabla N(x,z,t)\right] - \frac{N(x,z,t)}{\tau_R} - BN^2(x,z,t) + G(x,z,t) \quad (4.9)$$

We assumed that carrier mobility is non-dependent on carrier density, and *D* varies solely due to degeneracy, i.e. variation of Fermi integrals ratio:

$$D(N) = D_0 \frac{F_{1/2}(\eta)}{F_{-1/2}(\eta)} \quad (4.10)$$

To simplify the calculation we expanded this expression by the Taylor series:

$$D(N)=D_0(1+N/N_0), \quad (4.11)$$

and used it for numerical modeling. Using calculated carrier density profiles at different time moments we calculated dependence of diffraction efficiency on time witch was observed experimentally. Using this model with one set of parameters (D_0, N_0, τ_R, B, α, etc) we were able to fit all measured LITG transients at four different excitation intensities and four grating period values (Fig. 4.37.a,b,c,d solid lines). We deduced that at low carrier density the ambipolar diffusion coefficient equals to $D_0 = 1.5$ cm^2/s in the 80 μm-thick HVPE GaN sample.

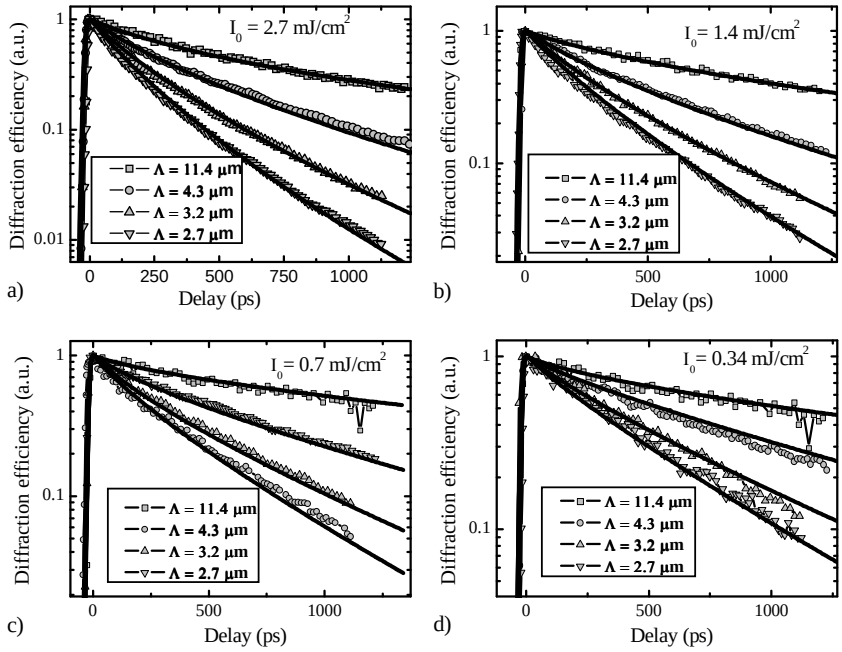

Fig. 4.37. Measured (gray points) and modeled (lines) LITG kinetics at different grating periods at four different excitation fluences in HPVE GaN (a,b,c and d) [A11].

Using the determined fitting parameter $N_0 = 2.2 \cdot 10^{19}$ cm^{-3} we calculated the dependence $D(N)$ around the degeneracy threshold (Fig. 4.38), according to Eq. 4.11. We also checked if Taylor expansion of $D(N)=D_0(1+N/N_0)$ is valid in investigated carrier density range. As Fig. 4.38 shows the approximation with $N_0 = 2.2 \cdot 10^{19}$ cm^{-3} corresponds to exact calculation of $D(N)$ (using Fermi integrals) with effective mass of $0.4m_e$. During intense band-to-band excitation equal number of electrons and holes are created therefore LITG experiment provides ambipolar diffusion coefficient. Since ambipolar diffusion coefficient $D=2D_hD_e/(D_h+D_e)$ depends both D_h and D_e the obtained effective mass value of $0.4m_e$ is reasonable, i.e. average value of hole and electron masses in GaN. The modeling also provided the value of the bimolecular recombination coefficient $B = 1 \cdot 10^{-11}$cm^3/s, which was very close to B value determined from LITG transients in μ-ELO and freestanding GaN [89].

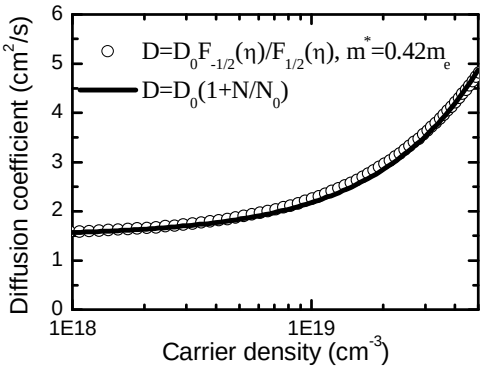

Fig. 4.38. The dependence of carrier diffusion coefficient on carrier density. Open points – calculations using Fermi integrals, line –Taylor expansion of Eq. (4.7) used in numerical modeling [A11].

4.3.3 Temperature dependence

At low temperatures the carrier plasma becomes more degenerated at the same carrier density, as effective density of states decreases. The calculations show (Fig.4.28) that at temperatures lower than 50 K the Fermi integrals ratio sharply increases and this according to Eq. 4.10 should lead to the increase of carrier diffusion coefficient.

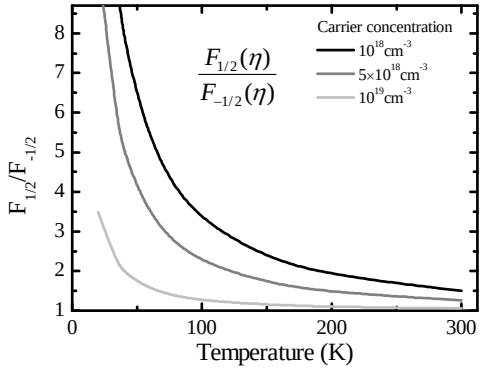

Fig. 4.39. Fermi integral ratio dependence on temperature for different carrier concentration, calculated for $m=0.4m_e$ [A11].

We put GaN sample in closed-cycle helium cryostat and performed LITG measurements at several grating periods at temperatures down to 10 K. In this way we measured the temperature dependence of ambipolar diffusion

coefficient of carrier for two excitations. The common situation is that a carrier mobility and *D* decreases in low temperatures due to impurity or dislocation scattering [93], while we observed sharp increase of diffusion coefficient value below 50 K and this effect was more pronounced for higher excitation conditions. This situation supports the model of increase of diffusion coefficient due to carrier degeneration.

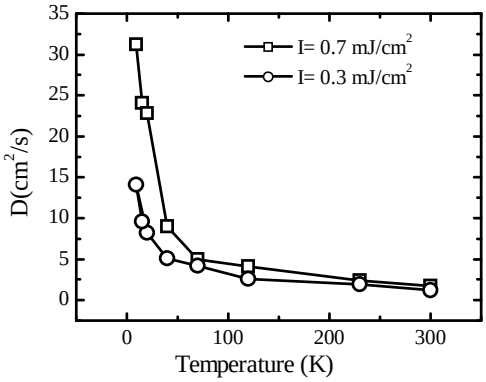

Fig. 4.40. Carrier diffusion coefficient dependence on temperature in HVPE GaN measured by LITG [A11].

4.3.4 Conclusions

We investigated carrier dynamics in highly excited HVPE GaN using LITG technique and observed carrier density dependent carrier diffusion and recombination processes. Using numerical modeling of carrier dynamics the increase of diffusion coefficient at high carrier density was explained as a Fermi pressure at degenerate carrier plasma The low temperature measurements confirmed the suggested model. The ambipolar diffusion coefficient value of D = 1.5 cm^2/s was determined as the low carrier density value for HVPE GaN crystals. This investigation proved that variation of diffusion coefficient described in Chapter 4.1 is ruled by carrier density. The samples with longer carrier lifetime and larger stimulated recombination threshold values exhibit higher carrier densities during experiments therefore large values of ambipolar diffusion coefficient is obtained.

4.4. On optical monitoring of carrier lifetime in GaN by LITG and TRPL techniques

Determination of electrical parameters of the advanced III-nitride materials requires innovative measurement techniques that enable a straightforward control of carrier lifetimes and diffusion lengths with respect to defect density and their electrical activity. The photoluminescence (PL) technique is commonly used to evaluate the quality of materials by analysing origin of excitonic and high carrier density related features in PL spectra [2, 94]. Surprisingly, the increasing quality of GaN layers was not always confirmed by an increasing carrier lifetime if measured by time-resolved photoluminescence (TRPL) techniques. The PL decay in high quality GaN layers revealed fast transients in subnanosecond time domain[95-97]. The luminescence decay time varied from 0.2 ns in HVPE grown heterostructures[95] to 0.44 ns in homoepitaxial ones][96], and were attributed to spontaneous luminescence at conditions of deep trap saturation regime. In the epilayers with improved structural quality and radiative efficiency (due to presence of TiN interlayer), the fast TRPL transients of 0.3 - 0.6 ns were followed by a slower decay component of 1.3 - 1.8 ns, and the non-exponential of decay was ascribed as nonradiative recombination processes in multilevel defect system [97]. Our measurements have also indicated the different values of carrier lifetimes in 270-μm thick freestanding GaN layer (of $\tau_R \approx 2 \cdot \tau_{PL}$ = 0.7 ns by TRPL[79] and τ_R = 2.9 ns by LITG[79]). Thus, the experimental data pointed out to steadily lower τ_R values and non-exponential transients in high quality thick GaN layers if measured by TRPL techniques.

In this Chapter we report experimental and numerical studies of nonequilibrium carrier dynamics in 400 μm-thick free-standing HVPE grown GaN crystal (Sample #11, Table 4.3) by using picosecond TRPL and LITG techniques. The results are compared with similar measurements in MOCVD-grown ~4 μm-thick GaN epilayers with few orders of magnitude higher dislocation density (Sample #2, Table 4.1). These studies, followed by a

numerical analysis of carrier spatial-temporal redistribution after their interband excitation by a short laser pulse, allowed us to attribute the origin of the fast initial PL transients mainly to the diffusion-governed carrier in-depth redistribution in a nonhomogeneously photo excited thick layer. We also verify that single exponential kinetics of LITG, being insensitive for carrier in-depth redistribution, directly and reliably provide carrier lifetimes in a wide range of magnitudes.

4.4.1 Experimental

Carrier dynamics in GaN samples was investigated at 300 K by using picosecond LITG and TRPL techniques. The TRPL was studied under 266 nm excitation (using a pulse duration of 25 ps, a spot size of 1 mm, and pump fluence up to 0.5 mJ/cm^2) and collected in a backward geometry via 0.4-m grating monochromator [95, 96]. An optical Kerr shutter ensured temporal resolution of ~20 ps. The band-to-band spontaneous PL transients were measured at ~3.4 eV. The LITG experiments experimental details are described in Chapter 4.1. We like to stress that LITG and TRPL measurements were carried out at very similar excitation conditions, nevertheless different excitation wavelengths were used (266 nm for TRPL and 355 nm for LITG), since both cases are band-to-band recombination and absorption coefficient is similar (α ~10^5 cm^{-1}). Also similar excitation fluences were used by both experimental techniques (~0.5 mJ/cm^2).

Carrier diffusion was investigated measuring diffraction efficiency kinetics at various grating periods, according to the relationship $1/\tau_G = 1/\tau_R + 1/\tau_D$, where $\tau_D = \Lambda^2/4\pi^2 D$ is the diffusive grating decay time, and τ_R is the average carrier lifetime in the excited region. The plot of inverse grating decay time vs its period (Fig.4.41) provided the values of the carriers ambipolar diffusion coefficient and lifetime – D = 1.9 cm^2/s and τ_R = 5.4 ns, in the thick HVPE sample. Similarly, the D = 1.6 cm^2/s and τ_R = 1.1 ns values for the standard MOCVD sample were determined. The bipolar carrier diffusion

lengths were found equal to 1 μm and 0.4 μm, and correspond to carrier plasma density of (1-5)·10^{18} cm^{-3} at conditions of the given LITG experiments.

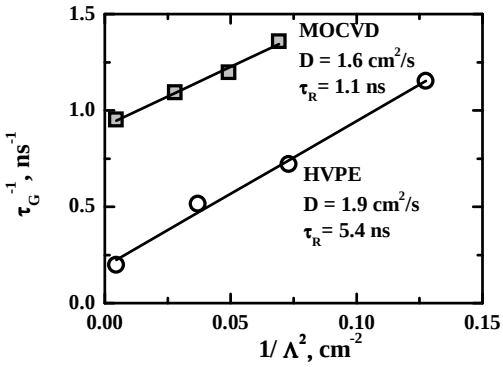

Fig.4.41. The inverse grating decay time τ_G^{-1} as a function of the grating period Λ^{-2} for HVPE and MOCVD grown samples. The determined values of ambipolar diffusion coefficient D and carrier lifetime τ_R are shown in the figure [A12].

The measured photoluminescence PL spectra of GaN samples consist of one broad emission band peaked in the vicinity of the bandgap energy (~ 3.4 eV). The observed spectra are typical for the radiative recombination of high-density electron-hole plasma that occurs under intense photoexcitation with the excitonic states screened by the free carriers [19, 95]. The estimated initial carrier density was of ~ 5·10^{18} cm^{-3}, being below the threshold of stimulated emission, and the initial carrier heating was insignificant.

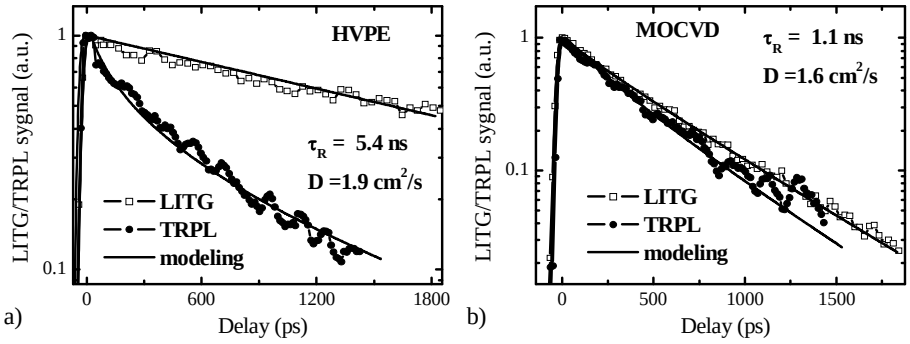

Fig.4.42. Comparison of the calculated curves (lines) and experimental data (points) of TRPL and TR LITG kinetics in the HVPE-grown free standing 400-μm thick layer

(a) and in the standard ~3.5-μm thick MOCVD-grown GaN layer (b). TRPL measurements were conducted by group leaded by prof. S. Juršėnas [A12].

Fig. 4.42 compares the LITG kinetics and spontaneous TRPL emission decay (at the peak position of the PL band) in the GaN layers with essentially different TD density. The PL decay is nearly exponential in subnanosecond time domain with constant of τ_{L1} = 680 ps and τ_{L2} = 460 ps for the HVPE and MOCVD grown layers, correspondingly. We note that the value of PL decay time in the free-standing layer (or the corresponding carrier lifetime of ($2\cdot\tau_{L1}$ = 1.4 ns) is, to our knowledge, the largest one observed in GaN at room temperature[2]. However, the LITG decay indicated much longer carrier lifetime in the free standing layer, while the PL and LITG decay constants were found quite similar for the MOCVD layer (Fig 2b).

4.4.2 Modeling

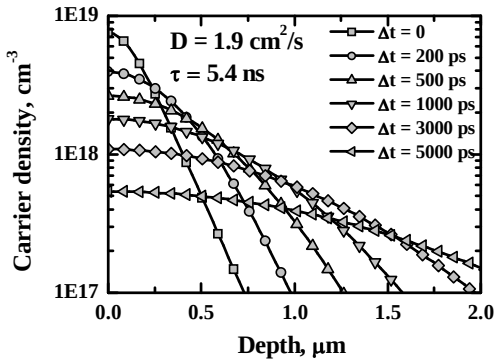

Fig.4.43. The calculated evolution of diffusion-governed carrier in-depth redistribution in thick GaN layers after photoexcitation by 25-ps duration laser pulse at 355 nm.

To get deeper insight into the temporal evolution of TRPL and LITG signals, we performed numerical modeling of carrier dynamics, assuming very nonuniform in-depth carrier profile at interband carrier photoexcitation. Two-dimensional model of carrier spatial-temporal redistribution was employed to evaluate carrier diffusion to the bulk and along the grating vector [76]. For

calculations, we used the determined values of D and τ_R for the studied samples (see Fig 4.41). The numerical data show that diffusion into the bulk rapidly dilutes the carrier plasma density generated at the surface and increases the excited layer thickness up to few μm in the time domain of measurements (Fig.4.43).

We note that both LITG and TRPL signal depend nonlinearly on carrier density, but in a different way. The diffraction depends on a probe beam phase shift, $\Phi=2\pi/\lambda\cdot\Delta nd$, which is integrated during the beam propagation through the sample, and the total accumulated value of an optical path change, $(\Delta n\cdot d)^2$, determines the diffracted beam efficiency, $\eta_{\mathrm{LITG}} \propto \Phi^2$. Since the probe beam integrates the plasma modulation over the sample depth, this makes the diffraction signal dependent on the total number of photogenerated electron-hole pairs in the sample and not on a specific density profile.

In case of TRPL, the signal is generated in a sample locally and nonlinearly, $I_{PL} \propto N^2$, and may be partially or strongly reabsorbed until it propagates through the sample. Therefore, only a limited thickness of a photoexcited layer may contribute to TRPL signal, and both the carrier spatial redistribution, their instantaneous density in the surface region, and the reabsorption effects must be explicitly considered for carrier lifetime determination. In GaN, the bandgap emission is quite strongly absorbed in the sample, thus, the measured PL signal corresponds to radiative recombination of carriers, present in a surface layer of a limited thickness. For simulation of LITG and PL decay, we used the calculated instantaneous carrier profiles $N(z,t)$ and the following relationships:

$$\eta_{FWM}(t) \propto \left[\int_0^d N(z,t)dz\right]^2 \tag{4.12}$$

$$I_{PL}(t) \propto \int_0^d N^2(z,t)\exp(-\alpha_{PL}z)dz \tag{4.13}$$

where α_{PL} is the absorption coefficient for spontaneous emission energy at 3.4 eV. Taking the value of α_{PL} = $5\cdot10^3$ cm^{-1} at its low limit[73] and the

sample-dependent D and τ_R values (see Fig.4.41), we calculated the decay curves of diffraction efficiency and TRPL decay (the solid lines in Fig.2a,b). For both samples, the data are in excellent agreement with the measured kinetics, thus confirming the origin of fast PL transients in thick HVPE layers as diffusion-governed fast carrier in-depth redistribution.

The modeling of LITG and TRPL kinetics at various D values disclose their sensitivity to the carrier redistribution due to diffusion (Fig.4.44) in high quality GaN layers. If the diffusion is not effective in the measurement time domain (1 - 2 ns), then the LITG and PL kinetics provide the same value of the carrier lifetime. The faster carrier diffusion, the more pronounced is fast PL transient. Carrier redistribution is already noticeable in PL kinetics at D value as low as $0.25\ cm^2/s$ due to nonlinear response of the PL signal to the decreased instantaneous carrier density in the surface region. We also note that even the slow decay component of PL (measured at 3 - 5 ns delay time) does not provide the real carrier lifetime as the ongoing process of diffusion to the bulk diminishes the instantaneous carrier density at the surface (see Fig.4.43). Indeed, this kind biexponential TRPL transient have been recently measured in ~5-μm thick GaN epilayers with the improved structural quality[97], but not provided the real lifetime values.

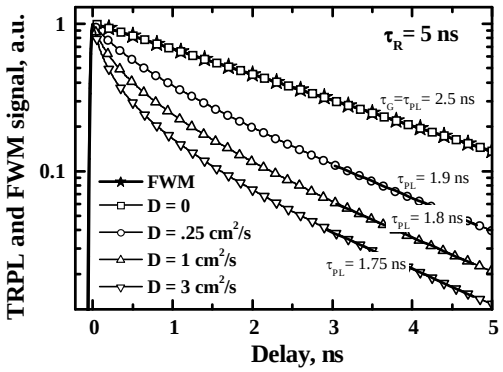

Fig. 4.44. Numerical modeling of TRPL intensity and LITG diffraction efficiency decay for the different values of diffusion coefficients.

4.4.3 Conclusions

The numerical analysis of carrier spatial-temporal redistribution allowed us to verify the origin fast TRPL transients as diffusion-governed carrier in-depth redistribution and reabsorption of a backward emission from the photoexcited layer. It was, therefore, concluded that determination of carrier lifetimes by using LITG technique in high quality and thick GaN layers is more advantageous and straightforward.

5. Carrier dynamics in InGaN layers and quantum-well structures

5.1. Investigation of InGaN epilayers

Carrier Localization versus In content

For investigation of photoelectrical, transport, and structural properties of InGaN alloys, carrier dynamics have been studied by LITG technique in $In_xGa_{1-x}N$ layers with different In content. The 50 nm thick $In_xGa_{1-x}N$ layers with In content of 8%, 10%, and 15% were grown on a sapphire substrate by low pressure MOCVD using a 1000 nm thick GaN epilayers as a buffer. The In fraction was estimated by X-ray diffraction. The samples for LITG studies were excited by the third or fourth harmonics ($h\nu = 3.5$ or 4.66 eV) of YAG:Nd laser.

At excitation by 355 or 266 nm light of the InGaN/GaN structure, the photoexcited carriers are confined in the front layer since the InGaN/GaN interface presents a potential barrier both for electrons and holes. Nevertheless, a part of the incident light penetrates into GaN buffer and creates free carriers which also contribute to light diffraction. To estimate the buffer contribution to the total LITG signal, the additional LITG experiment was performed in the buffer layer. The short carrier recombination time (~50 ps) was found in the GaN layer, while carrier lifetime in InGaN layers was by order magnitude longer (Fig.5.1).

More detailed numerical analysis of carrier dynamics in simultaneously excited InGaN and GaN layers has shown [98] that 40% of the light is absorbed in InGaN ($\alpha \sim 10^5$ cm^{-1}, $d = 50$ nm, $(1-\exp(-\alpha d)) = 40$. Nevertheless, fast carrier transfer from GaN to InGaN layer takes place in the interface region. This process, in addition to short carrier lifetime in the buffer GaN, makes the contribution of GaN layer to diffraction rapidly vanishing (in ~200 ps). This simplified analysis of the diffraction kinetics allowed to

attribute the LITG signal at delay time $\Delta t > 200$ ps, solely to carriers confined in InGaN layer.

Carrier localization effect in InGaN layers, which is known being dependent on the In content [99, 100], was studied by measuring the kinetics of LITG kinetics at several grating periods (from 3 to 10.5 μm). This allowed to determine carrier diffusion coefficient and lifetime values in InGaN layers (Fig.5.1b). We found the decrease of diffusivity of carriers from 1.5 cm^2/s to 0.9 cm^2/s with increasing In content (from 8 % to 15 %). We attributed this tendency to higher density of states which localize carriers and overall band potential fluctuation due to inhomogenous In incorporation[100, 101], which makes carriers less mobile.

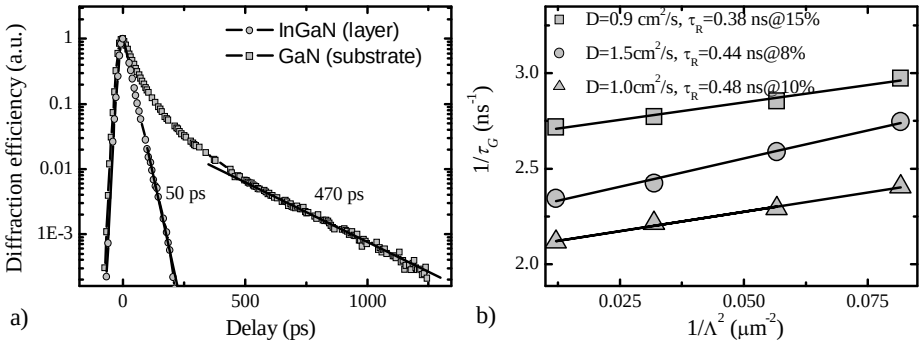

Fig. 5.1. LITG kinetics in InGaN/GaN heterostructure (x=8%) and in the GaN buffer measured at 355 nm excitation (a). Angular characteristics measured in InGaN layers with different In content used for determination of ambipolar diffusion coefficient and lifetime of photo-excited carriers (b) [A13].

We used 266 nm light (instead of 355 nm) for grating excitation in order to generate carriers mainly in InGaN layer. We performed measurements of exposure characteristics just after the excitation pulse, which provided information about stimulated recombination threshold (see Chapter 4.1) and grating decay kinetics at large grating periods which corresponds to decay of grating solely due to recombination process, and therefore provides carrier lifetime values. We found (similarly like for GaN/Si, GaN/SiC case, see Chapter 4.1) a correlation of carrier lifetime with stimulated recombination

threshold, i.e. longer carrier lifetime leads to lower stimulated recombination threshold (Fig.5.2). The sample with 10% of indium exhibited the longest carrier lifetime (280 ps) and the smallest stimulated recombination threshold (0.1 mJ/cm^2). For sample with 15% of In content 2.5 time shorter recombination time and not pronounced saturation of exposure characteristic was observed.

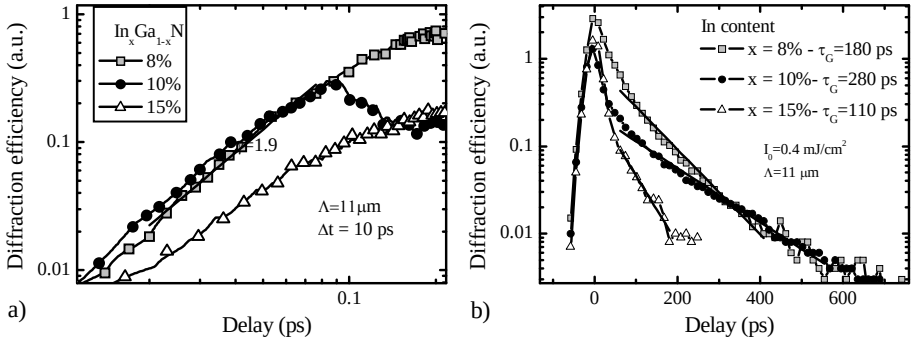

Fig.5.2. Exposure characteristics (a) and kinetics of free carrier grating (b) in InGaN layers with different In content [A13].

The stronger carrier localization (at increasing In content from 8% to 10%) prevented them from reaching nonradiative recombination centers, thus increasing the carrier lifetime. While the short carrier lifetime for sample with 15 % of In is due to poor crystalline quality which is observed for InGaN samples with indium content higher than 10% [102]. This explains well the features of exposure characteristics: it saturates only for a layer having the longest lifetime, which is advantageous for carrier accumulation. The highest intensity and lowest threshold of stimulated recombination in $In_xGa_{1-x}N$ (x = 10%) sample were confirmed by TRPL measurements conducted by S. Juršėnas et al [103].

LED efficiency droop

In the development of InGaN-based light-emitting diodes LEDs, producers encountered reduction of internal quantum efficiency of LED at high current densities, which was called as a efficiency droop problem[39]. Several carrier loss mechanisms to explain the droop phenomenon have been proposed

such as carrier leakage [40, 41], carrier delocalization [42, 43], and Auger nonradiative recombination [44].. Gardner *et al* from InGaN-LEDs producing company Lumiled also supported Auger recombination model for efficiency reduction. [37, 38]. These conclusions were based on electrical measurement of external quantum efficiency of working LEDs based quantum well InGaN structure. For investigation of Auger recombination impact, Lumiled company provided an InGaN layer for time resolved studies of carrier dynamics and determination of nonlinear recombination rates, which could directly demonstrate Auger recombination as carrier density or delay time varying recombination rate.

The 100-nm thick InGaN layer with x = 5.3% were grown on 2.3 μm GaN buffer and sapphire as a substrate. The reference sample without InGaN top layer was used to identify contribution of GaN layer to diffraction as both InGaN and GaN were excited during LITG experiment.

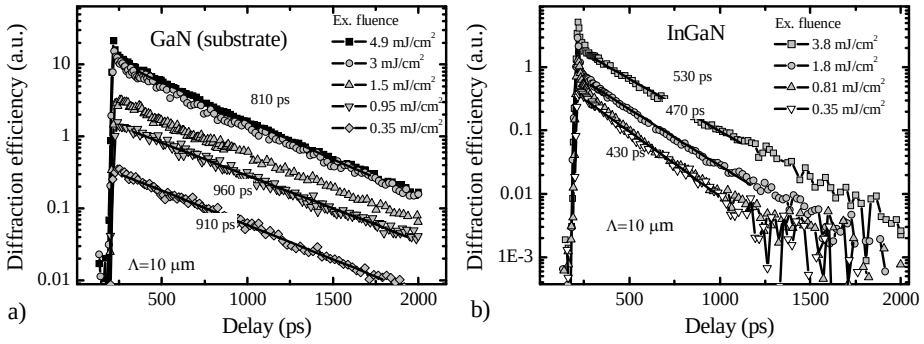

Fig.5.3. LITG kinetics measured at 355 nm excitation in InGaN/GaN (x=5%) and reference GaN layers at large grating period at different excitation fluences.

LITG kinetics at 355 nm excitation at several excitation fluences were measured in both InGaN and GaN (reference) samples (Fig.5.3). The kinetics measured in GaN were typical for standard quality GaN layers (see Chapter 4.2, Figs. 4.1, 4.3a) - the carrier lifetime was around 1 ns, the ultra-fast part at high excitation exhibited the stimulated recombination. The measurements of LITG kinetics in InGaN exhibited grating decay twice faster (~450 ps). Also the stimulated recombination threshold was lower compared to GaN since low

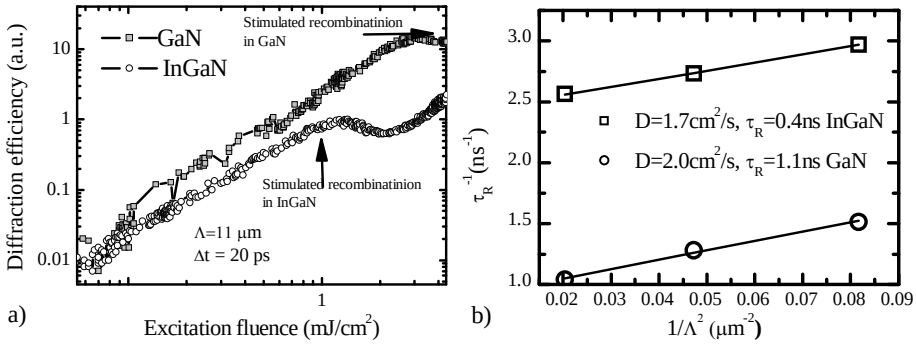

Fig. 5.4. The exposure characteristics measured in InGaN and reference GaN samples at 355 nm excitation.

excitation kinetic (0.8 mJ/cm^2) already showed fast initial part. The longer carrier lifetime in GaN and low stimulated threshold in InGaN determined situation that LITG signal at higher excitation fluences is mainly governed by carrier in GaN layer. This is clearly seen in exposure characteristics measured in both samples at 20 ps delay of the probe beam (Fig. 5.4). The EC measured in GaN exhibit single slope until excitation fluence reaches the stimulated recombination threshold, while EC measured in InGaN is more complicated. In the low excitation range, I_0 <1 mJ/cm^2, the increase of is determined by carrier generation in InGaN layer (GaN contribution is small). At around 1 mJ/cm^2 stimulated recombination in InGaN takes place and carrier density in InGaN is reduced to threshold value by stimulated recombination. At higher excitation fluences contribution of GaN buffer is seen, since carrier density in this layer increases. This explanation is also supported by measurement of kinetics. If measurement performed in a single layer structure, the all kinetics measured at excitation fluences above stimulated recombination threshold converge (Fig. 5.3a, 4.3, 4.18), since stimulated recombination exhausts inversed population to the similar carrier density. While in InGaN case, the amplitude of kinetics increases with excitation, and carriers generated in GaN buffer determine this. From this discussion two important conclusions could be made. Firstly, InGaN dynamics (for a particular sample) is observed for excitation fluences below 1 mJ/cm^2. And secondly, at these conditions the maximal possible carrier

density is created in InGaN layer. This is very important for investigation of Auger recombination, since Auger recombination should be observed at high carrier densities.

After given above considerations, only two kinetics of lowest excitation fluences (0.35 and 0.8 mJ/cm^2) can be considered as revealing carrier dynamics in InGaN layer. These two kinetics were single exponential and did not show change of recombination rate with decreasing carrier density. This shows that at room temperature, at the highest possible carrier density (~5·10^{19} cm^{-3}) obtained by optical pumping in InGaN epilayers, the Auger recombination is not contributing to carrier recombination.

The measurements at different grating periods (Fig.5.4b) provided ambipolar diffusion coefficient value of D = 1.7 cm^2/s for InGaN layer with 5% In content, which is little bit higher if compared to previously described samples with higher In content, thus indicates weaker carrier localization in this layer.

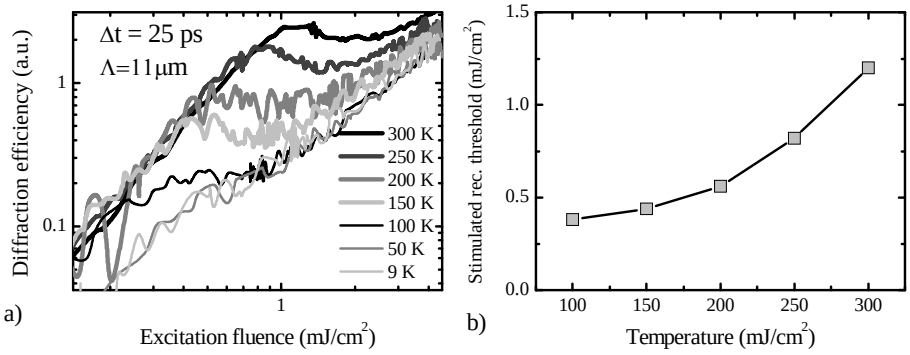

Fig.5.5. LITG exposure characteristics measured at 266 nm excitation in InGaN/GaN (x = 5%) in temperature range 9 – 300 K at probe delays Δt = 25 ps (a). The dependence of stimulated recombination threshold measured in InGaN/GaN on temperature

To get deeper understanding of recombination processes temperature dependent LITG measurements were carried out in temperature range 9 – 300 K. The 266 nm excitation was used in order to have higher absorption coefficient and in this way to achieve higher contribution to diffraction signal

from InGaN layer. Moreover, low excitation fluences (0.5 and 0.25 mJ/cm^2) were used to ensure excess carrier density below stimulated recombination onset and thus monitor the carrier dynamics in the InGaN layer.

The measured exposure characteristics (Fig.5.5a) showed that stimulated recombination threshold reduces with temperature from 1.2 at 300 K to 0.3 at 100 K. The reduction of stimulated recombination threshold with temperature (~2 times in temperature range from 300 K to 150 K) in InGaN MWQs was observed by PL [104, 105] and explained as reduction of internal quantum efficiency at high temperatures, which is also confirmed by LITG measurements described below.

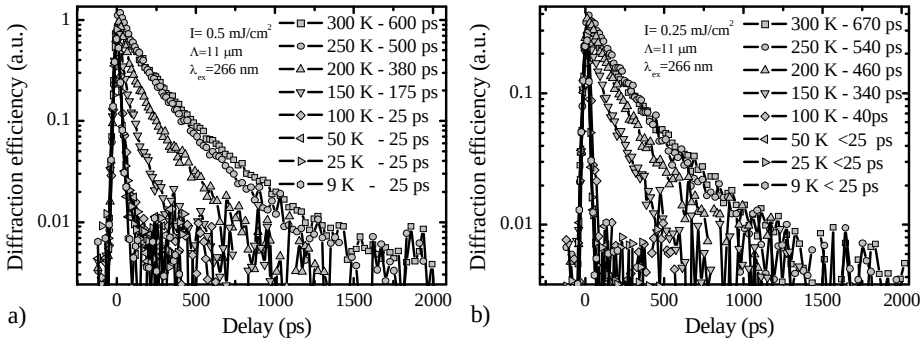

Fig.5.6. LITG kinetics measured at 266 nm excitation in InGaN/GaN (x = 5%) in temperature range 9 –300 K at different excitation fluence (a – I_0 = 0.5 mJ/cm^2 and b - I_0 = 0.25 mJ/cm^2).

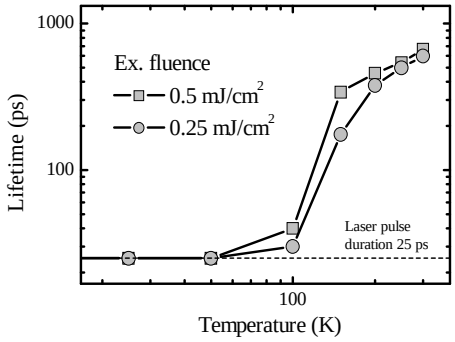

Fig.5.7. Carrier lifetime values determined by LITG experiment at two excitation fluences. The low limit of 25 ps is determined by time resolution of the LITG experimental setup, i.e. pulse duration of the laser (dashed line) .

LITG kinetics measured at 266 nm excitation in 9 – 300 K temperature range are shown in Fig.5.6. At room temperature kinetics were slightly non-exponential in measured time domain with small decrease of carrier lifetime with increasing excitation (670 ps at 0.25 mJ/cm^2 and 600 ps at 0.5 mJ/cm^2). While lowering temperature carrier lifetime decreased while below 100 K it was limited by our time resolution of the experimental setup (~25 ps) (Fig.5.7). The decrease of carrier lifetime values in high temperature region (150 – 300 K) we attributed to increase of bimolecular recombination rate, according to $B \propto T^{-3/2}$[82]. But we note that the bimolecular recombination was not a dominant recombination channel at 300 K, since carrier lifetime was determined by linear (nonradiative) recombination. The bimolecular recombination became important only at ~150 K, where non-exponential shape of kinetics and lifetime dependence on excitation were significant. The further sharp decrease of carrier lifetime was due to stimulated recombination, as stimulated recombination threshold decreased with temperature and at temperatures below <150 K became lower than used excitation fluences for LITG kinetics measurement.

In conclusion, the LITG investigation in InGaN epilayers revealed that dominant recombination channel at room temperature is nonradiative recombination at excitation densities below stimulated recombination threshold. The measurements at low temperature demonstrated impact of bimolecular recombination, which became dominant at temperatures below 150 K. The LITG kinetics did not exhibit Auger recombination features in 9 – 300K temperature range.

5.2. Investigation of InGaN MQWs

In previous sections the carrier dynamics in 50 –100 nm thick InGaN layers were described, but for industry investigation of carrier dynamics in InGaN quantum wells (QWs) is more relevant, since commercially available LEDs are based on QWs. World's leading manufacturer of MOCVD equipment for III-Nitrides growth – Aixtron company provided us two InGaN/GaN based LED structures. Five InGaN quantum wells with GaN barriers were grown on GaN buffer layer using sapphire as a substrate. Structures exhibited peaks of luminescence at 470 nm and 525 nm.

LITG experiments were carried out using 355 nm excitation beams, which excited QWs as well as GaN barriers (for resonant excitation the total thickness of InGaN layers was too small to obtain a measurable signal). Therefore important issue was to distinguish the contributions of InGaN and GaN in excess carrier dynamics. LITG kinetics measured in 525 nm LED sample when exciting from front and from back via sapphire substrate are shown in Fig. 5.8. The kinetics measured when exciting InGaN QWs was double exponential with slow component of 3.1 ns and fast component of about 200 ps. The contributions (amplitudes) of these two components varied with excitation fluence. The fast component we attributed to signal coming from GaN buffer, since 200 ps decay rate was the same as measured from the backside, i.e. in GaN buffer. In addition, the exposure characteristics of the front layer (Fig.5.9a) at high excitations exhibited features typical for LITG in GaN layer (i.e. the increasing efficiency with slope value of 2, see Fig.5.9b, and saturation due to stimulated recombination). Thus, at low excitation signal was detected from carrier localized in wells, while increased excitation saturated this signal due occupation of available states in QWs. At even higher excitations, the grating minima became also populated and in this way grating modulation ratio decreased and diffraction signal from QWs at high excitation was competed by signal from GaN buffer.

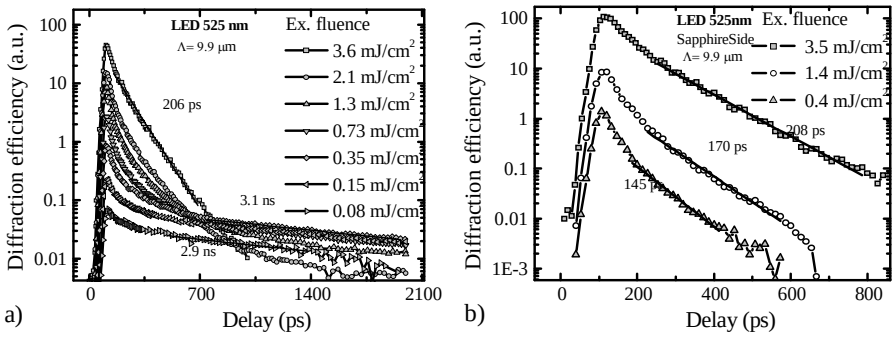

Fig.5.8. LITG kinetics measured in LED structure at 355 nm excitation from a front side (a) and backside (b).

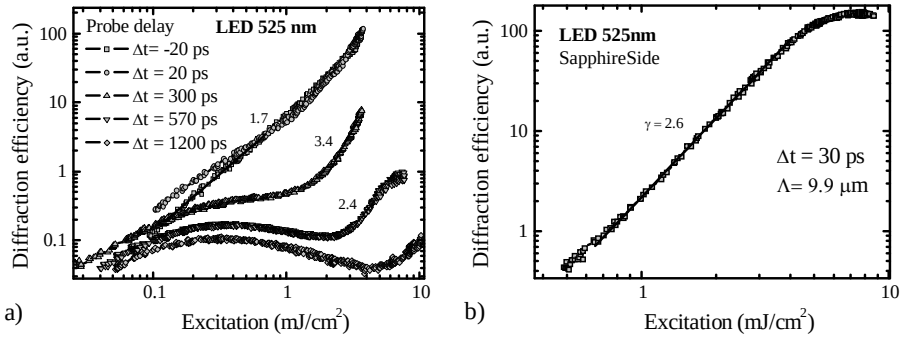

Fig.5.9. Exposure characteristics measured in LED structure exciting from a front side (a) and backside (b). Numbers indicated the slope of EC in log-log scale.

The similar results (carrier lifetime of 3.1 ns in InGaN QWs) were obtained for 470 nm LED structure (Fig.5.10), just saturation effect was noticed at low excitation fluence, which is consist with suggested model since shorter luminescence wavelength correspond to higher bandgap of InGaN layer and therefore to a shallower quantum well.

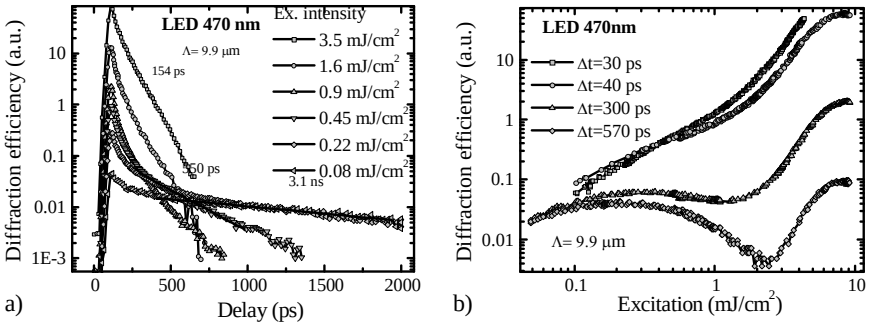

Fig. 5.10. LITG kinetics(a) and exposure charakterisctis (b) measured in LED structure at 355 nm excitation.

From this analysis two important conclusions could be made. Firstly, electronic states in InGaN QWs can be easily filled and higher optical (or electrical) injection do not provide addition carrier to QWs. This observation supports hypothesis that efficiency droop could due to carrier delocalization (or over barrier diffusion). Secondly, this investigation showed the increased carrier lifetime in InGaN QWs compared to InGaN layers. Lifetime in best quality InGaN layers was around 500 ps, while lifetime in QWs reached value of 3.1 ns. To reach deeper insight into the latter observation, we performed study of carriers dynamics in InGaN quantum well structures with different thickness of well/barrier regions[106].

InGaN MQWs with different thickness

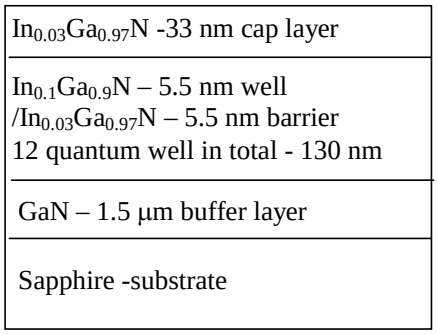

Fig. 5.11. InGaN MQWs sample structure. The other samples differs in thickness and number of quantum wells.

The multiple well structures were grown on 1.5 μm GaN buffer layer that was grown on sapphire substrates by MOCVD. The three samples had different well/barrier thickness, but constant overall thickness of active region; this was achieved by growing different quantity of QWs. The well/barrier thickness of three samples deduced from x-ray diffraction were: 12 periods of 5.5 nm/5.5 nm, 4 periods of 17 nm/17 nm, 2 periods of 34 nm/34 nm. Total thickness of well and barrier material, adding the 33 nm-thick $In_{0.03}Ga_{0.97}N$ cap layer were ~170 nm. The indium composition of the well and barrier were 10% and 3%, respectively.

The LITG experiments were carried by 355 nm excitation, which ensured band-to-band generation of carriers in wells and barriers; the exciting light also reached the GaN buffer layer. The fast relaxation of carrier to well (which take place < 1 ps time domain [107]) and quite large active layer thickness ensured that observed LITG signal was determined by carrier localized in QWs, which simplified analysis if compared to previously described cases. If to assume that some carriers generated in GaN also diffused into QWs, then d = 200 nm thick layer "provided" carriers to QWs. As absorption depth is around $1/\alpha = 100$ nm, then $1-\exp(-\alpha d) = 86$ % of carriers were generated in 200 nm thick layer.

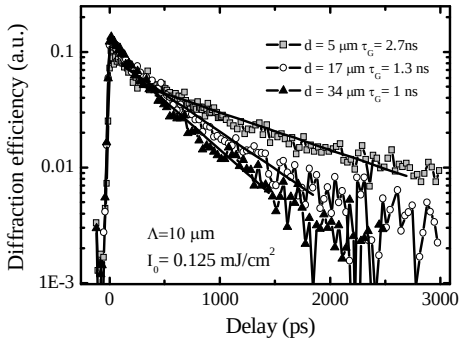

Fig.5.12. LITG kinetics in different thickness MQWs of InGaN, measured at 355 nm excitation at large grating period ($\Lambda = 10$ μm) and low excitation fluence ($I_0 = 0.125$ mJ/cm^2). The grating decay time corresponding to carrier lifetime indicated in the legend.

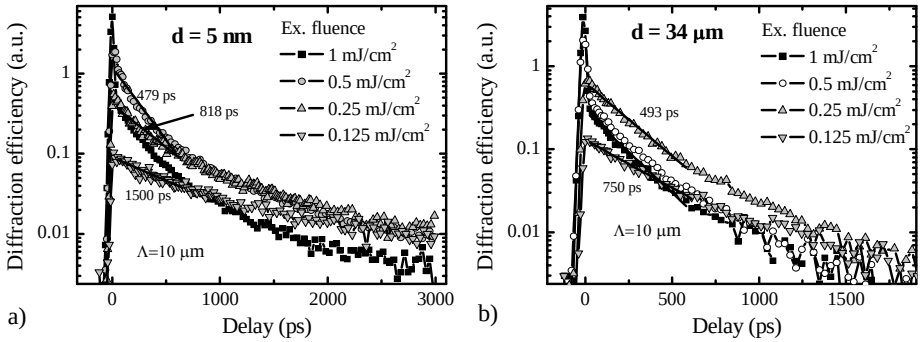

Fig. 5.13. LITG kinetics measured at 355 nm excitation in MQWs structure with QW thickness of $d = 5$ nm and $d = 34$ nm.

The LITG kinetics measured at large grating periods (Fig.5.12) showed that the carrier lifetime was the longest in the thinnest QWs (~2.7 ns at the lowest excitation) and the shortest in thickest QW (~1 ns). Also, an important feature was that kinetics were nonexponential, i.e exhibiting features of nonlinear carrier recombination (Fig. 5.13). At higher excitation fluences the non-exponential carrier recombination dynamics were even more pronounced. In Fig 5.14a grating decay times versus excitation fluence are plotted. The initial slope of –0.9 indicated nearly linear recombination rate dependence on carrier density $1/\tau \propto N$. This indicates that bimolecular recombination is a dominant recombination mechanism in these structures at high excitation. The

further growth of recombination rate (or decrease of grating decay time) at higher excitations is limited due to the onset of stimulated recombination, which suppresses the increase of carrier density. For the sample with largest QWs thickness (34 μm) the stimulated recombination threshold is the lowest 0.4 mJ/cm^2 (Fig.5.14b), therefore, the saturation of carrier recombination rate is observed at the smallest excitation fluence (0.5 mJ/cm^2, Fig.5.13a).

The reason of the variation of stimulated recombination threshold in these structures is not completely understood. But the highest value observed in sample with d = 5 nm could be related to the largest number of layers which scatter the emitted light and increase losses for the stimulated emission, thus for efficient stimulated recombination process larger inversion of population (gain) is required. Furthermore, wider well thickness is also helpful for an enhancement of the optical and electronic wavefunction confinement in the well[108]. Both effects can cause the threshold to drop, like the classical AlGaAs/GaAs system[109].Therefore, the threshold decreases with increasing well thickness.

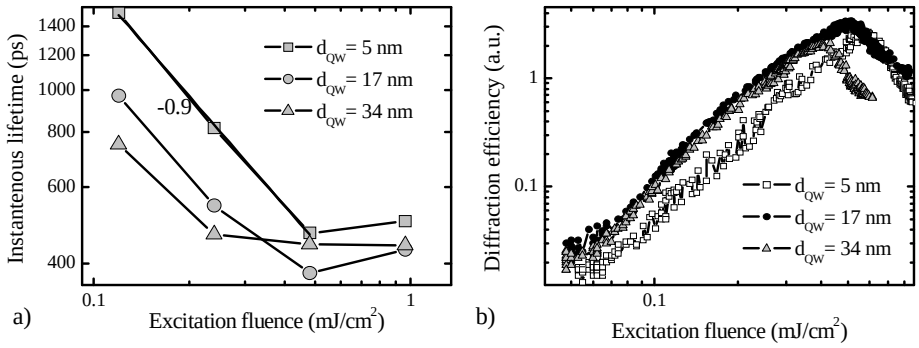

Fig.5.14. Dependence of instantaneous carrier lifetime on excitation fluence measured in different thickness InGaN MQWs structures by LITG technique (a). LITG exposure characteristics measured at 20 ps probe delay in InGaN MQWs structures (b).

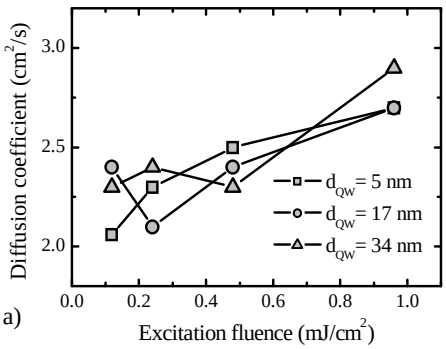

Fig.5.15. The dependence of ambipolar carrier diffusion coefficient on excitation fluence in InGaN MQWs structure with different well thickness determined by LITG measurements at different grating periods.

The measurement of LITG kinetics at different grating periods enabled us to measure ambipolar carrier diffusion coefficient in InGaN MQWs structures. The dependence of ambipolar carrier diffusion coefficient on excitation fluence is shown in Fig.5.15. The *D* value varies from ~2.2 cm^2/s at low excitation up to ~2.7 cm^2/s. The same trend was observed in GaN epilayers and explained as a Fermi pressure in degenerated electron-hole plasma in Chapter 4.3. The same model seems to be valid for InGaN MQWs structures. The initial high value of *D* is also due to high carrier density in wells, since carrier excited in 200 nm are collected by 66 nm wells which also blocks carrier diffusion into the substrate depth and allows study of in-plane diffusion at high carrier density.

For further analysis of carrier dynamics LITG measurements at low temperature and 266 nm excitation were performed in sample with longest carrier lifetime (d = 5 nm). The non-exponential, carrier density dependent low temperature LITG kinetics (Fig.5.16a) confirmed the dominant role of bimolecular recombination in sample with QW thickness of d = 5 nm. The decay rate varied with temperature with slope -1.3 (Fig.5.16b) which was approaching the pure bimolecular recombination rate with slope value of -1.5[82].

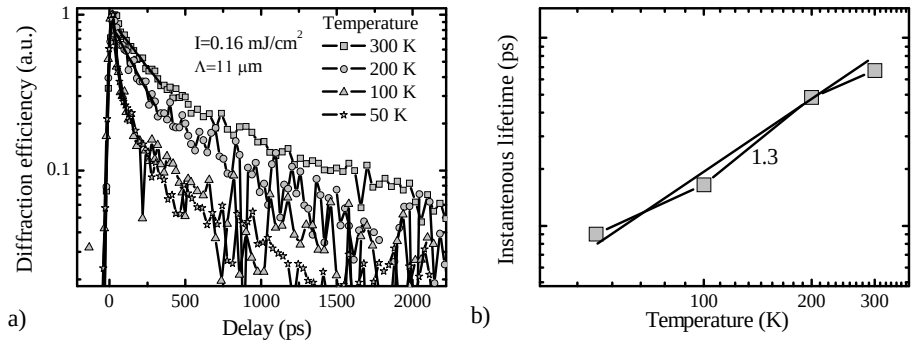

Fig. 5.16. LITG kinetics measured at 266 nm excitation in InGaN MQWs structure with d = 5 nm in temperature range 50 –300 K (a). The dependence of instantaneous carrier lifetime deduced from fitting in probe delay range of Δt = 0 – 300 ps on temperature (b).

5.3 Conclusions

The LITG measurements provided photoelectrical parameters for InGaN layers at high excitation case – D = 1-1.7 cm^2/s, τ_R = 120 – 500 ps, $L_D \approx 0.2$ μm. Low and In content dependent carrier diffusivity revealed In segregation induced carrier localization. At room temperature defect related recombination determined quite low carrier lifetime values and rejected the possibility of Auger recombination mechanism. The features of bimolecular recombination were observed only at low temperatures.

The investigation in InGaN MQWs revealed longer carrier lifetimes up to 3 ns, the pronounced bimolecular recombination at room temperature which became dominant recombination channel at lower temperatures. The determined diffusion coefficient values increased at higher carrier densities due to degeneracy of carrier distribution.

6. Carrier dynamics in synthetic diamonds

The defect-free diamond is known to exhibit the largest values of heat conductivity and carrier mobility of all the wide-bandgap semiconductors. This makes the material attractive for production of ultraviolet and ionizing radiation detectors that could operate under extreme environmental conditions. To insure the high efficiency of charge collection, a carrier diffusion length is to be maximized by reducing the density of electrically active point and extended defects, which are commonly present in diamonds as an isolated substitutional nitrogen (C-defects) or as their aggregations (A-defects and others) [110]. Standard evaluation of electronic properties by transient photoconductivity and Hall effect [48, 111] or time-of flight techniques [112] requires ohmic contacts deposition, what may impose intrinsic limitations. Microwave-reflection techniques have been recently applied to measure carrier lifetimes in natural diamonds [113] while were limited to 1 ns temporal resolution. LITG technique has been recently applied to measure the thermal diffusion coefficients of CVD diamond thin slabs

In this Chapter we report for the first time an application of a picosecond LITG technique for optical monitoring of nonequilibrium carrier dynamics HPHT and CVD diamonds. The measurements directly provided the electronic parameters (carrier lifetime, diffusion coefficient and length) in highly excited surface layer or in the bulk.

6.1 Carrier dynamics in HPHT diamonds

Samples

We investigated optical-grade mechanically polished free-standing samples of HPHT bulk crystals with thickness of 1 mm. The single-crystal diamonds were seed-grown in ISM NASU by HPHT method using constant radial and axial temperature gradients as described elsewhere [114]. The hydrogen and nitrogen concentration was determined from UV and IR optical absorption spectra.

Table 6.1. Investigated HPHT diamond samples, their type and concentration of C-centers

Samples	D8	D1	D10B	D10A
Crystal type	IIa	IIb	Ib	Ib
Concentration of C-centers, cm^{-3}	$< 10^{17}$	$< 10^{17}$	10^{17}-10^{19}	$1.3 \cdot 10^{19}$

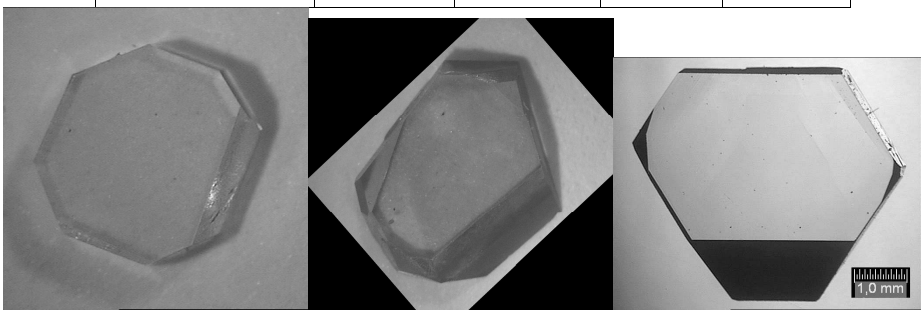

Fig. 6.1. Photos of HPHT diamond samples D8, D10A, D10B (from left to right).

Description of the investigated samples is given in Table 1. A type of the HPHT diamond crystal was determined according to its optical properties, which are related to the impurity content, mainly to nitrogen concentration. The samples have been classified using the absorption spectra features in IR, UV, and visible spectral range. The samples D8 and D1 have been assigned to the "nitrogen-free" diamonds of IIa and IIb type because of absence of characteristic absorption bands in 1000 - 1500 cm^{-1} spectral range (the optical absorption data indicated that nitrogen concentration is below 10^{17} cm^{-3}). Nevertheless, small absorption in a range from 250 to 300 nm still exists. It indicates the presence of a residual nitrogen defect states. Neutral boron acceptor concentration $[N_A - N_D]$ in semiconducting sample D1 is estimated to lie within interval from 2.3×10^{17} to 6.7×10^{17} cm^{-3}. In diamonds of Ib type (samples D10A and D10B), strong absorption at a range around 8 μm wavelength has been found due to high density ($\sim 10^{19}$ cm^{-3}) of substitutional nitrogen. Sample D10B exhibited strong non-homogeneity of defects concentration distribution across the plate.

Experimental results

In Fig.6.2, we present the kinetics of diffraction efficiency in the different types of HPHT diamond plates. For the interband excitation at 213 nm, the electron-hole plasma was created within thin excited layer of thickness $d_{eff} \sim \alpha^{-1}$ (α is coefficient of light absorption), which may vary from 3 to 10 μm [115, 116]. For the used excitation energy density (up to 5 mJ/cm^2), the nonequilibrium carrier concentration in range (1 - 5)×10^{18} cm^{-3} was reached.

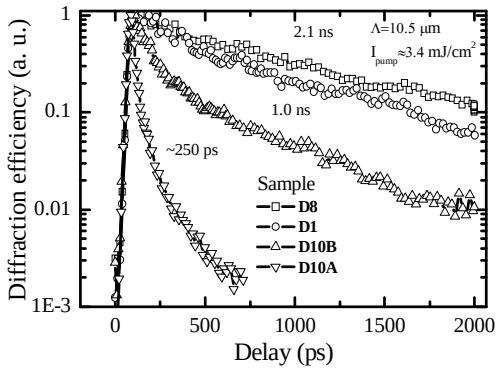

Fig.6.2. Grating decay kinetics measured in different types of HPHT diamonds at 213 nm excitation. The grating decay time τ_G values are given on the plot. For spatially nonhomogeneous sample D10B the measurements were conducted at zone #3 where nitrogen defects concentration was estimated to be about (2-3)·10^{17} cm^{-3} [A14].

The LITG kinetics at large grating (Fig.6.2) period directly indicating carrier lifetime value (since diffusive decay is much slower) showed that carrier recombination rate correlates with C-center (substitution nitrogen) concentration. The D8 and D1 samples with non-detectable C-center concentration exhibit carrier lifetime values large than 2.1 ns. The fast initial decay with τ_G = 100-300 ps was measured for the crystal D10A with high density of C-centers (1.3·10^{19} cm^{-3}).

The initial grating decay time for sample #10A directly indicated the τ_R value, as the diffusive grating decay time $\tau_D = \Lambda^2/4\pi^2 D$ = 3 ns (for the given grating period of Λ = 10.5 μm and using the determined D_a value). The fast

initial decay with τ_G = 100-300 ps for the crystal #10A (Fig. 1) correlates well with by order of magnitude higher density of C-centers (see Table 1).

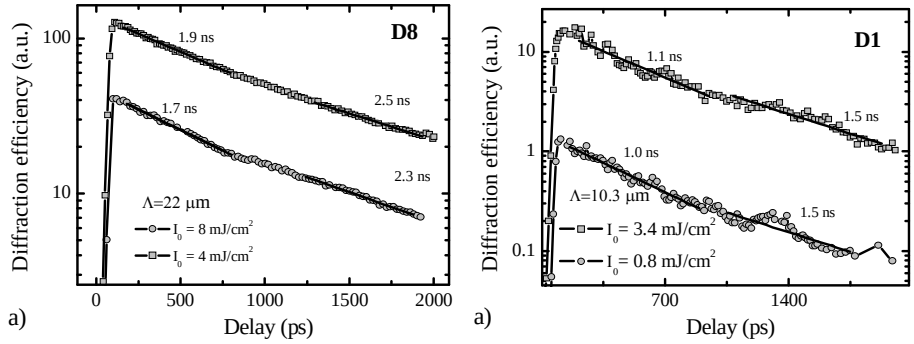

Fig.6.2. LITG kinetics measured at large grating period in HPHT "nitrogen free" diamond samples at different excitation fluences. The grating decay times are indicated in the plot.

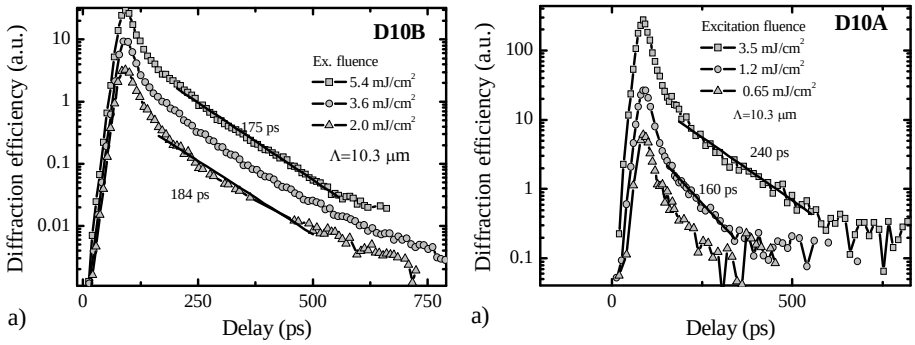

Fig.6.3. LITG kinetics measured at large grating period in HPHT diamond samples with high C-defects concentration. The grating decay times are indicated in the plot.

The diffraction kinetics in all investigated diamond are non-exponential. The kinetics measured in samples of type IIa or IIb (D1, D8 with low nitrogen defect density) are just slightly non-exponential in time domain of our investigation, i.e. grating decay time in the initial kinetic part differs slightly (~1.3 times) from decay time in the end of kinetic. While samples with higher nitrogen concentration show clear nonexponential carrier recombination dynamics (samples D10A, D10B). In general the observed nonexponential decay of LITG kinetics can be caused by several reasons – bimolecular or Auger recombination, surface recombination, saturation of centers of

nonradiative recombination or sample inhomogeneity. The Bimolecular or Auger recombination can be discarded as the main recombination mechanism since kinetics at different excitation fluences have same decay times. That means that different decay rate is not related to different carrier density, thus intrinsic mechanisms as bimolecular and Auger recombination is not plausible model.

The surface recombination also cannot explain nonexponential behavior of LITG kinetics since light penetration depth at 213 nm (~10 μm[115, 116]) is much larger than diffusion length of excited carriers ($L_D \approx 1.6$ μm, will be shown later). Therefore, surface recombination is not effective channel of recombination.

The saturation of some nonradiative recombination centers could explain why carrier dynamic is faster just after pump pulse compared to the later moments. Also the slightly slower kinetics are observed at elevated excitation fluences (see Fig.6.2a, 6.3b), what also contributes to saturation model. But this effect is too weakly pronounced in order to explain nonexponential behavior of observed kinetics.

The mostly plausible model, which explains the nonexponential carrier dynamic, is nonhomogeneous distribution of nonradiative recombination centers in the samples. This leads to situation when different sample area features different recombination time, and then all these areas are observed in one experiment the kinetic becomes nonexponential. The inhomogeneous distribution takes places in plane of the sample as well as in-depth.

We have exploited LITG technique for a homogeneity mapping of the sample D10B. The delay of the probe pulse was set to certain delay respect to pump pulses (Δt=100 ps) and sample was scanned measuring how diffraction efficiency depends on sample position. The scan of diffraction efficiency actually represents variation of carrier lifetime, since the value of diffraction efficiency at certain delay depend only on carrier lifetime. It was observed that more transparent crystal parts have high carrier lifetime, while in the dark parts (with high C defects concentration) carrier lifetime is shorter than 50 ps. These

experiments show in-plane non-homogeneity of the sample, but also in-depth variation could be very plausible.

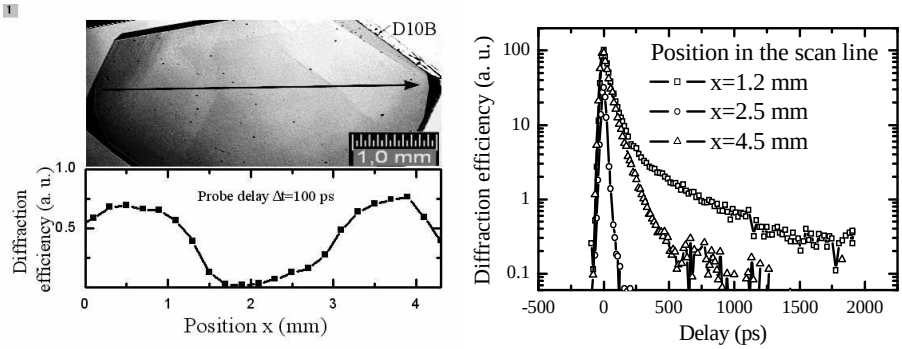

Fig.6.4. The scan of diffraction efficiency along D10B sample correspond to a variation of carrier lifetime value (a). The LITG kinetics measured at different scan positions (b).

For investigation of carrier dynamics in wider excitation range we used bulk excitation with 266 nm light (4th harmonic of YAG laser). At below band gap excitation, the carriers were created within the entire thickness of the 1 mm-thick layers, thus excited carrier density was few orders of magnitude lower (~5×10^{16} - 10^{17} cm^{-3}). For the latter case, the grating kinetics in defect-free type IIa crystal are shown in Fig. 6.5.

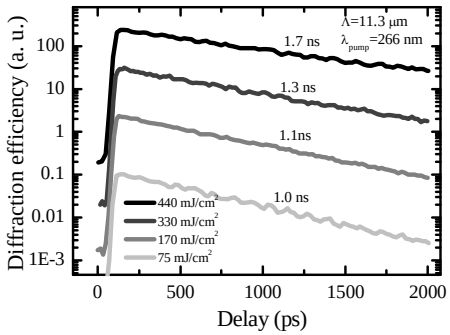

Fig.6.5. Grating decay kinetics measured in IIa type HPHT diamond sample (D8) at below bandgap excitation (λ = 266 nm) at different energy density. The τ_G values are given on the plot [A14].

The results obtained at bulk excitation revealed a gradual increase of grating decay time from 1 ns up to 1.7 ns with increasing photoexcitation

density (Fig. 6.5). We attribute this tendency to a gradual saturation of recombination centers (C-centers) which have a detrimental effect on carrier lifetime [117]. The gradual increase of carrier lifetime pointed out that the total density of recombination centers in this layer is comparable or higher than the photoexcited carrier concentration (~10^{17} cm^{-3}). As a consequence, the further increase of carrier lifetime up to 2.8 ns was observed in a case of surface excitation (i.e. at even higher carrier density $N \geq 10^{18}$ cm^{-3}). This insight supports the model of saturating recombination activity of C-centers as source of the nonexponential grating dynamics in the samples with higher nitrogen impurity density (Fig. 6.2, curves for #10A and #10B samples).

The excitation of sample D10B and D10B with 266 nm light was followed by formation of free-carrier grating and stress-strain grating, i.e. standing ultrasound wave (Fig. 6.6). Temperature grating was observed due to sudden local heating of material. Theses oscillations were observed in N10B sample due to high absorption coefficient for below bandgap excitation (due high density of impurities) and used large excitation fluence 200 mJ/cm^2.

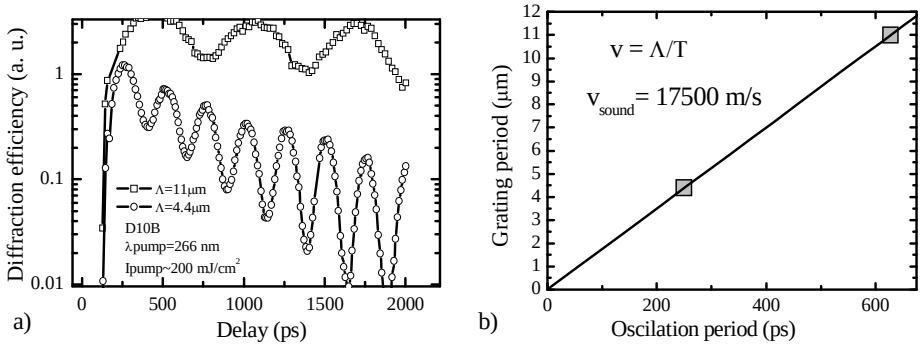

Fig.6.6. LITG kinetics measured in D10B at 266 nm excitation at large fluence 200 mJ/cm^2 (a). The determination of sound velocity in diamond (b).

For determination of ambipolar diffusion coefficient in diamond the LITG kinetics at several grating periods Λ (from 2.3 to 22 μm) were measured (Fig. 6.7a). By plotting grating decay time versus its period in appropriate way ($1/\tau_G = f(1/\Lambda^2)$), we determined the ambipolar diffusion coefficient D_a and carrier lifetime τ_R in the D8 and D10B samples (Figs. 6.7b). A linear fit

provided a value of $D_a = 9 \pm 0.2$ cm^2/s, while an intersection with ordinate axis at $1/\tau_G = 1/\tau_R$ gave the carrier lifetime $\tau_R = 2.8 \pm 0.1$ ns for IIa type diamond sample at above bandgap excitation. A similar set of data at below band gap excitation provided nearly the same D_a value (Fig 6.7b, open points), while the $\tau_R$value was slightly smaller 2.5 ns. Surprisingly, the value of diffusion coefficient in highly defected sample D10B were obtained the same as in "defect free" D8 sample – $D = 9.2$ cm^2/s, while carrier lifetime was 20 times shorter - $\tau_R = 140$ ps. The results pointed out two important features of carrier dynamics in diamond. Firstly, that even at high carrier density (of about 10^{18} cm^{-3}) the photoelectrical parameters of high quality HPHT diamond are not influenced by nonlinear recombination and diffusion. And secondly, that carrier C-centers do not influence the diffusivity of carriers.

The measured data allowed to estimate the carrier diffusion length $L_D = \sqrt{D_a \tau_R}$ of 1.6 μm for the IIa type HPHT diamond with low nitrogen density and the corresponding value of an ambipolar mobility, $\mu_a = 360$ cm^2/Vs.

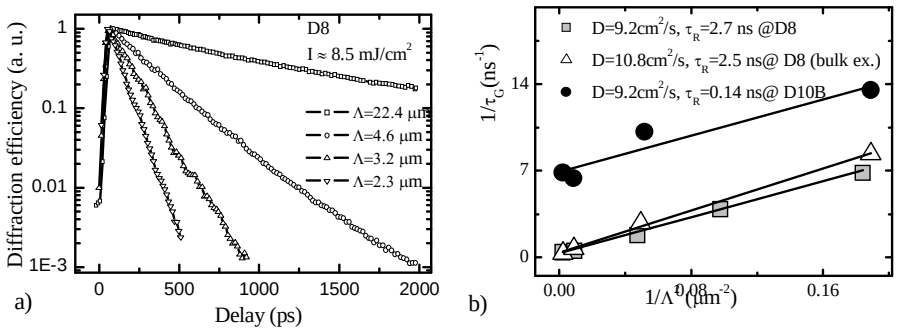

Fig.6.7. Grating decay kinetics measured at different grating periods Λ in the diamond sample D8 at interband excitation ($\lambda = 213$ nm) (a). In (b) the plot of the inverse grating time τ_G^{-1} as a function of inverse grating period Λ^{-2} for the HPHT diamond sample D8 at surface excitation (gray squares) and at bulk excitation (open triangles), and in the sample D10B (black circles). The samples exhibit the similar diffusion coefficient values, but very different carrier lifetimes [A14].

With highest quality D8 diamond sample we performed temperature studies. Using closed cycle helium cryostat LITG measurements were conducted until 10 K. Also we performed high temperature studies reaching 500 K temperature. The low temperature LITG kinetics at large grating period are shown in Fig.6.8. Almost single exponential kinetics at high temperatures become oscillating at low temperatures (T < 100K). The generation of sound wave could be related to reduced specific thermal capacitance at low temperature, therefore the laser induced thermal gradients become higher which lead to more efficient formation of strain-stress (sound) waves. Since this effect distorted free carrier kinetics, carrier diffusion coefficient and lifetime were calculated down to 100 K.

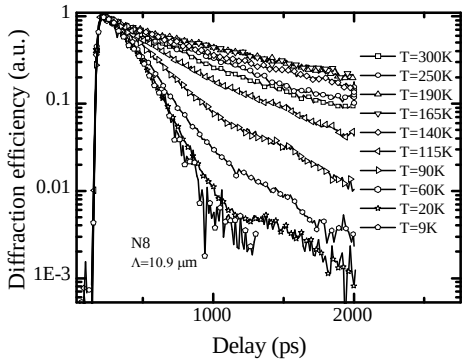

Fig.6.8. LITG kinetics measured in high quality HPHT diamond layer in temperature range of T = 9 – 300 K.

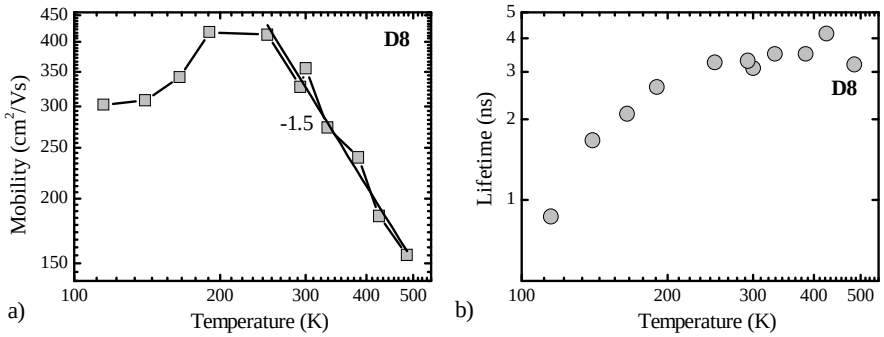

Fig.6.9. Temperature dependence of carrier mobility (a) and lifetime (b) measured in HPHT diamond layer D8.

The measured carrier mobility dependence on temperature indicate two carrier scattering mechanism in highly excited diamond. Above 220 K the slope equals to –1.5, thus shows the acoustic phonon scattering. While below 220K positive slope of $\mu = f(T)$ characteristic is determined by defect related scattering.

6.2 Carrier dynamics in CVD diamonds

The polycrystalline CVD diamond samples were grown by microwave plasma in CH_4/H_2 mixture with varying CH_4 content (from 1.5% to 5%) [67].

Table 2. Investigated polycrystalline CVD diamond samples and nitrogen related defects concentration.

Sample	D125	D112	D129	D88
Nitrogen concentration, ppm	<< 1	1.2	~ 1	4.7-8.1

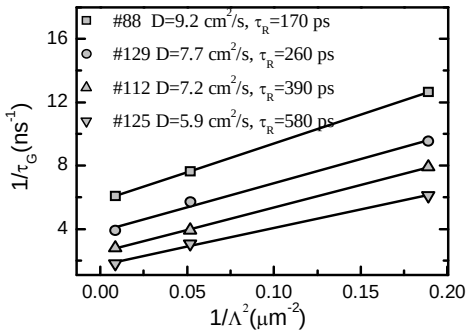

Fig.6.10. The plot of the inverse grating time τ_G^{-1} as a function of inverse grating period Λ^{-2} for the CVD grown diamond samples at surface excitation (λ = 213 nm). The determined values for the ambipolar diffusion coefficient and the carrier lifetime are shown on the plot [A14].

LITG measurements were carried out on CVD diamond slabs with different nitrogen defects concentration. The τ_G were measured for several grating periods and plotted in an appropriate way (Fig. 6.10). A linear fit according to Eq.1.25 provided the D_a and τ_R values. The D_a values in CVD

samples varied from 6 to 9 cm^2/s and were found slightly smaller if compared to those in bulk HPHT diamonds, while the carrier lifetimes were significantly smaller in CVD layers and ranged from 170 to 580 ps. The carrier recombination times correlated with the nitrogen defect concentration, similarly to HPHT diamond case, i.e. higher nitrogen concentration leads to faster carrier recombination. It is worth to note, that the given set of CVD diamonds exhibited nearly constant value of carrier diffusion length - $L_D \approx 0.5$ μm. This peculiarity is presumably caused by more efficient electron trapping and leads to $N_e < N_h$, thus the effective mobility increases, as $\mu = (N_e + N_h)/(N_e / \mu_p + N / \mu_n)$. Therefore, diffusion length value in this set of CVD samples remains nearly constant.

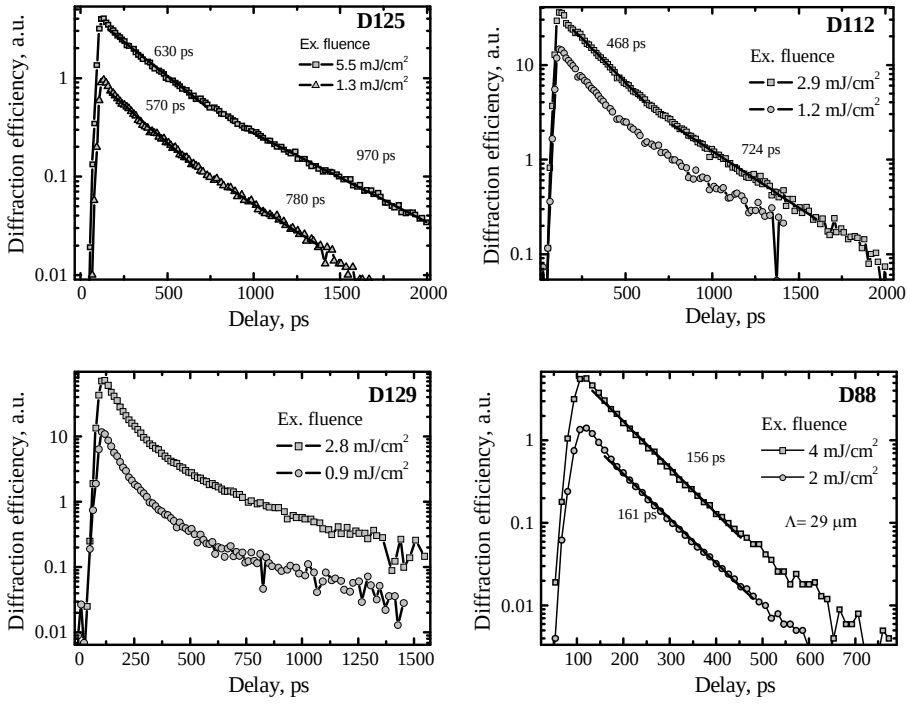

Fig.6.11. LITG kinetics in CVD diamonds with different nitrogen related defect concentration measured at larger grating period ($\Lambda = 29$ μm) at band-to-band excitation by 213 nm.

The LITG kinetics at large grating period (Fig.6.11) were non-exponential but not dependent on excitation fluence, i.e. carrier density. The same features as were

observed for HPHT diamond layers, therefore we suggest similar relaxation model for excited carriers. The nonhomogenous distribution of nitrogen related nonradiative recombination centers defines carrier dynamics in CVD diamonds.

Recently LITG investigation were also carried out on high quality single-crystal diamond layers grown by using the microwave plasma enhanced chemical vapor deposition technique (MWPE-CVD) on (100) Ib orientated HPHT diamond substrates (Sample A14060s). For the growth details see Ref. [118]. The high material quality was confirmed by time of light technique, which provided near 100% charge collecting efficiency for this sample.

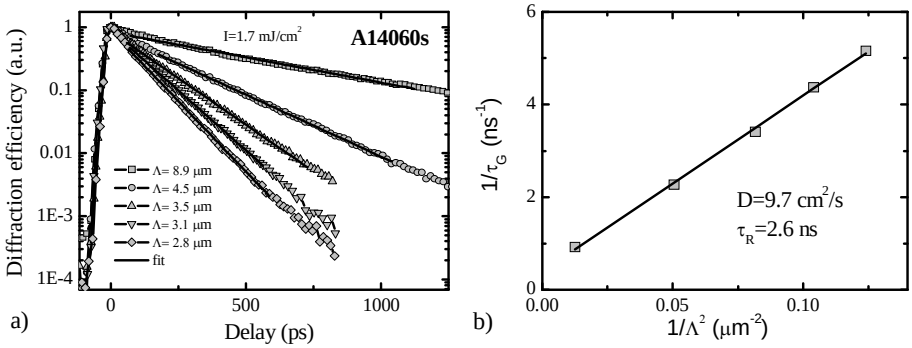

Fig.6.12. Grating decay kinetics measured at different grating periods Λ in the single crystal CVD diamond layer A14060s at interband excitation (λ = 213 nm) (a). In (b) the plot of the inverse grating time τ_G^{-1} as a function of inverse grating period Λ^{-2} for determination of carrier diffusion coefficient and lifetime.

The Fig.6.12. shows single exponential LITG kinetics measured at interband excitation (213 nm) used for determination carrier lifetime and diffusion coefficient in single crystal CVD diamond layer. The obtained values of D = 9.7 cm^2/s and τ_R=2.6 ns are very similar to values obtained for high quality HPHT IIa layers. Firstly, this indicates the high material quality (i.e. low defect density) of CVD samples. Secondly, the same values of photoelectrical parameters obtained for different technology grown diamond suggest that theses values should be intrinsic materials parameters not affected by defects.

The temperatures studies for CVD samples showed the same tendencies as HPHT sample D8. The carrier mobility dependence on temperature exhibited the positive and negative slope values, although the absolute values of mobility in T = 100 –150 K range were about twice larger in A14060 compared to D8 case. The carrier lifetime values are almost constant till 150 K, when start to decrease also similarly like in D8. At temperatures lower than ~60 K the diffraction on ultrasound grating is detected.

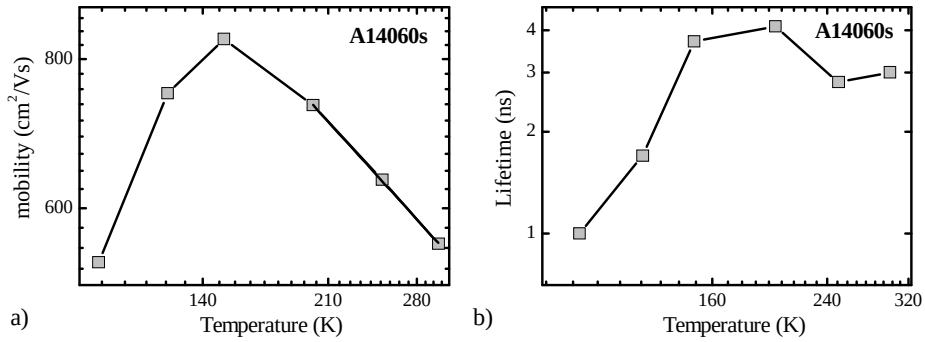

Fig.6.13. Temperature dependence of carrier mobility (a) and lifetime (b) measured in single crystal CVD layer A14060s.

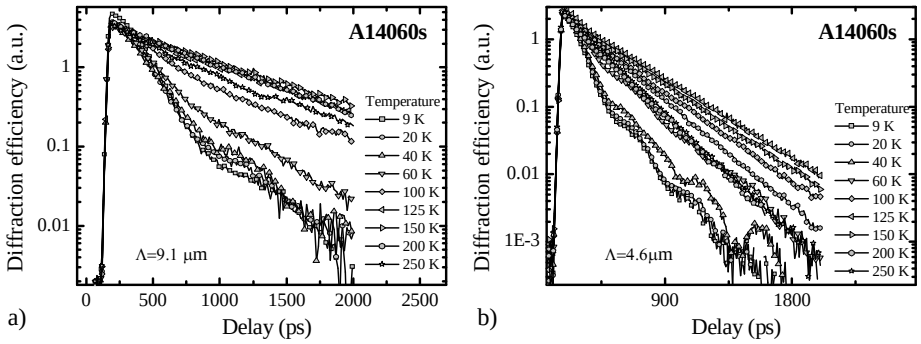

Fig.6.4. LITG kinetics measured in single crystal CVD layer A14060s in temperature range of T = 9 – 300 K at band-to-band excitation (213 nm) at two different grating periods Λ = 9.1 μm (a) and Λ = 4.6 μm (b).

6.3 Conclusions

We demonstrated a novel all-optical way to monitor carrier lifetime, diffusion coefficient, and diffusion length in HPHT and CVD diamonds. The

correlation between the transient grating decay time and concentration of nitrogen defects pointed out that nitrogen-related defects act as the main centers of nonradiative recombination. The nonhomogenous distribution, and saturation of defects defects determined non-exponential carrier recombination kinetics. The similar values of carrier diffusion coefficient $D \approx 9.4$ cm^2/s and lifetime τ_R = 2.7 ns were deduced for high quality single crystal HPHT and CVD diamonds. The determined by optical mean dependence of carrier mobility on temperature showed that the scattering by acoustic phonons is a dominant mechanism at room temperature.

7. Concluding Summary

1. A novel heterodyne detection scheme for LITG technique was presented. The heterodyning was achieved by coherently mixing the picosecond pulses of diffracted and scattered light. A phase difference between theses fields is controlled by moving HBS along its grating vector. LITG signal decay kinetics, recorded at two HBS positions corresponding for phase difference of π, allow to measure separately Δn^2 and Δn kinetics, which is impossible in the convenient transient grating setup. This approach was employed to study a competition of coexisting free carrier and thermal optical nonlinearities in CVD grown diamond films.

2. The LITG measurements in numerous GaN layers with different dislocation revealed clear dependence of carrier lifetime on dislocation density, thus pointing out that dislocations acts as main carrier recombination centers. The strong dependence of carrier lifetime versus TDD ($\tau_R \propto (N_{TD})^{-0.5}$) at large dislocation densities ($N_{TD} > 10^8$ cm^{-2}) is weakened by dominance of bimolecular recombination in samples with low TDD at high carrier densities. The dislocation governed carrier lifetime in these samples were deduced by low excitation measurement via below bandgap excitation or discriminated by numerical modeling, and could be approximated by function: $\tau_R[ns] = 2.6 \cdot 10^4 / \sqrt{N_{TD}[cm^{-2}]}$

3. LITG measurements in GaN layers in temperature range of T = 9 – 300 K and subsequent numerical modeling of carrier dynamics allowed to determine directly the values of the bimolecular recombination coefficient ($B = 2 \cdot 10^{-11}$ cm^3/s) and its temperature dependence ($B \propto T^{-3/2}$), to separate impacts of radiative and nonradiative recombination. The measurements of diffusion coefficient in wide temperature range allowed to identify that scattering by the acoustic phonons is dominant mechanism in all temperature range.

4. LITG experiments provided increasing carrier diffusion coefficient values in GaN layers from $D = 1.5\ cm^2/s$ at low carrier densities ($N<5\cdot10^{18}\ cm^{-3}$) to $D = 4.1\ cm^2/s$ at around $5\cdot10^{19}\ cm^{-3}$. Using numerical modeling of carrier dynamics the increase of diffusion coefficient at high carrier density was explained as a Fermi pressure at degenerate carrier plasma. The low temperature measurements confirmed the suggested model. Moreover, this finding shows that the main mechanism responsible for diffusion coefficient variation in samples with different dislocation density is carrier lifetime induced variation of excess carrier density during LITG experiment, but not a dislocation induced scattering.

5.The numerical analysis of carrier spatial-temporal redistribution allowed us to verify the origin fast TRPL transients measured in GaN layers as diffusion-governed carrier in-depth redistribution and reabsorption of a backward emission from the photoexcited layer. It was, therefore, concluded that determination of carrier lifetimes by using LITG technique in high quality and thick GaN layers is more advantageous and straightforward.

6. The LITG measurements provided photoelectrical parameters for InGaN layers at high excitation case – D = 1-1.7 cm^2/s, τ_R = 120 – 500 ps, $L_D \approx 0.2$ μm. Low and In content dependent carrier diffusivity revealed In segregation induced carrier localization. At room temperature defect related recombination determined quite low carrier lifetime values and rejected the possibility of Auger recombination mechanism. The features of bimolecular recombination were observed only at low temperatures.

The investigation in InGaN MQWs revealed longer carrier lifetimes up to 3 ns, the pronounced bimolecular recombination at room temperature which became dominant recombination channel at lower temperatures. The determined diffusion coefficient values increased at higher carrier densities due to degeneracy of carrier distribution.

7. A novel all-optical way to monitor carrier lifetime, diffusion coefficient, and diffusion length in HPHT and CVD diamonds was demonstrated. The similar values of carrier diffusion coefficient $D \approx 9.4\ cm^2/s$

and lifetime τ_R = 2.7 ns were deduced for high quality single crystal HPHT and CVD diamonds The correlation between the carrier lifetime and concentration of nitrogen defects pointed out that nitrogen-related defects act as the main centers of nonradiative recombination. The determined by optical mean dependence of carrier mobility on temperature showed that the scattering by acoustic phonons is a dominant mechanism at room temperature.

References

[1] B. Monemar, P. P. Paskov, J. P. Bergman, A. A. Toropov, T. V. Shubina, T. Malinauskas, and A. Usui, Phys. Status Solidi B, **245**, 1723 (2008).

[2] S. Juršėnas, S. Miasojedovas, and A. Žukauskas, J. Cryst. Growth, **281**, 161 (2005).

[3] S. F. Chichibu, A. Uedono, T. Onuma, T. Sota, B. A. Haskell, S. P. DenBaars, J. S. Speck, and S. Nakamura, Appl. Phys. Lett., **86** (2005).

[4] E. Kuokstis, G. Tamulaitis, K. Liu, M. S. Shur, J. W. Li, J. W. Yang, and M. A. Khan, Appl. Phys. Lett., **90** (2007).

[5] X. G. Zhang, D. H. Rich, J. T. Kobayashi, N. P. Kobayashi, and P. D. Dapkus, Wide-Bandgap Semiconductors for High Power, High Frequency and High Temperature, **512**, 193 (1998).

[6] M. Albrecht, J. L. Weyher, B. Lucznik, I. Grzegory, and S. Porowski, Appl. Phys. Lett., **92** (2008).

[7] M. Albrecht, H. P. Strunk, J. L. Weyher, I. Grzegory, S. Porowski, and T. Wosinski, J. Appl. Phys., **92**, 2000 (2002).

[8] C. K. Choi, B. D. Little, Y. H. Kwon, J. B. Lam, J. J. Song, Y. C. Chang, S. Keller, U. K. Mishra, and S. P. DenBaars, Phys. Rev. B, **6319**, art. no. (2001).

[9] E. Gaubas, S. Juršėnas, R. Tomasiunas, J. Vaitkus, A. Žukauskas, A. Blue, M. Rahman, and K. M. Smith, Nuclear Instruments & Methods in Physics Research Section a-Accelerators Spectrometers Detectors and Associated Equipment, **546**, 247 (2005).

[10] E. Gaubas, P. Pobedinskas, J. Vaitkus, A. Uleckas, A. Žukauskas, A. Blue, M. Rahman, K. M. Smith, E. Aujol, B. Beaumont, J. P. Faurie, and P. Gibart, Nuclear Instruments & Methods in Physics Research Section a-Accelerators Spectrometers Detectors and Associated Equipment, **552**, 82 (2005).

[11] K. Okamoto, K. Inoue, Y. Kawakami, S. Fujita, M. Terazima, A. Tsujimura, and I. Kidoguchi, Rev. Sci. Instrum., **74**, 575 (2003).

[12] J. Mickevicius, R. Aleksiejūnas, M. S. Shur, S. Sakalauskas, G. Tamulaitis, Q. Fareed, and R. Gaska, Appl. Phys. Lett., **86** (2005).

[13] Y. Kawakami, Z. G. Peng, Y. Narukawa, S. Fujita, S. Fujita, and S. Nakamura, Appl. Phys. Lett., **69**, 1414 (1996).

[14] C. I. Harris and B. Monemar, Appl. Phys. Lett., **67**, 840 (1995).

[15] Y. Zhong, K. S. Wong, W. Zhang, and D. C. Look, Appl. Phys. Lett., **89** (2006).

[16] E. I. Rashba and G. E. Gurgenishvili, Sov. Phys.-Solid State, **4**, 759 (1962).

[17] G. Pozina, J. P. Bergman, T. Paskova, and B. Monemar, Appl. Phys. Lett., **75**, 4124 (1999).

[18] K. P. Korona, R. Doradzinski, M. Palczewska, M. Pietras, M. Kaminska, and J. Kuhl, Physica Status Solidi B-Basic Research, **235**, 40 (2003).
[19] F. Binet, J. Y. Duboz, J. Off, and F. Scholz, Phys. Rev. B, **60**, 4715 (1999).
[20] H. K. Kwon, C. J. Eiting, D. J. H. Lambert, M. M. Wong, R. D. Dupuis, Z. Liliental-Weber, and M. Benamara, Appl. Phys. Lett., **77**, 2503 (2000).
[21] G. E. Bunea, W. D. Herzog, M. S. Unlu, B. B. Goldberg, and R. J. Molnar, Appl. Phys. Lett., **75**, 838 (1999).
[22] S. Juršėnas, S. Miasojedovas, G. Kurilcik, A. Žukauskas, and P. R. Hageman, Physica Status Solidi a-Applied Research, **201**, 199 (2004).
[23] A. V. Sampath, G. A. Garrett, C. J. Collins, P. Boyd, J. Choe, P. G. Newman, H. Shen, M. Wraback, R. J. Molnar, and J. Caissie, Journal of Vacuum Science & Technology B, **22**, 1487 (2004).
[24] S. F. Chichibu, H. Marchand, M. S. Minsky, S. Keller, P. T. Fini, J. P. Ibbetson, S. B. Fleischer, J. S. Speck, J. E. Bowers, E. Hu, U. K. Mishra, S. P. DenBaars, T. Deguchi, T. Soto, and S. Nakamura, Appl. Phys. Lett., **74**, 1460 (1999).
[25] T. Izumi, Y. Narukawa, K. Okamoto, Y. Kawakami, S. Fujita, and S. Nakamura, Journal of Luminescence, **87-9**, 1196 (2000).
[26] J. Xie, U. Ozgur, Y. Fu, X. Ni, H. Morkoc, C. K. Inoki, T. S. Kuan, J. V. Foreman, and H. O. Everitt, Appl. Phys. Lett., **90** (2007).
[27] J. Xie, Y. Fu, U. Ozgur, Y. T. Moon, F. Yun, H. Morkoc, H. O. Everitt, A. Sagar, R. M. Feenstra, C. K. Inoki, T. S. Kuan, L. Zhou, and D. J. Smith, Gallium Nitride Materials and Devices, **6121**, B1210 (2006).
[28] J. Xie, U. Ozgur, Y. Fu, X. Ni, H. Morkoc, C. K. Inoki, T. S. Kuan, V. Foreman, and H. O. Everitt, Gallium Nitride Materials and Devices II, **6473**, 47304 (2007).
[29] S. Juršėnas, S. Miasojedovas, A. Žukauskas, B. Lucznik, I. Grzegory, and T. Suski, Appl. Phys. Lett., **89** (2006).
[30] S. Chichibu, T. Azuhata, T. Sota, and S. Nakamura, Appl. Phys. Lett., **69**, 4188 (1996).
[31] E. Kuokstis, J. W. Yang, G. Simin, M. A. Khan, R. Gaska, and M. S. Shur, Appl. Phys. Lett., **80**, 977 (2002).
[32] S. Chichibu, T. Sota, K. Wada, and S. Nakamura, Journal of Vacuum Science & Technology B, **16**, 2204 (1998).
[33] Y. Narukawa, S. Saijou, Y. Kawakami, S. Fujita, T. Mukai, and S. Nakamura, Appl. Phys. Lett., **74**, 558 (1999).
[34] C. Netzel, R. Doloca, S. Lahmann, U. Rossow, and A. Hangleiter, Phys. Status Solidi C, **0**, 324 (2002).
[35] A. Satake, Y. Masumoto, T. Miyajima, T. Asatsuma, and M. Ikeda, Phys. Rev. B, **60**, 16660 (1999).
[36] B. Monemar, J. P. Bergman, J. Dalfors, G. Pozina, B. E. Sernelius, P. O. Holtz, H. Amano, and I. Akasaki, J. Nitride Semicond. Res., **4**, 16 (1999).

[37] Y. C. Shen, G. O. Mueller, S. Watanabe, N. F. Gardner, A. Munkholm, and M. R. Krames, Appl. Phys. Lett., **91** (2007).
[38] N. F. Gardner, G. O. Muller, Y. C. Shen, G. Chen, S. Watanabe, W. Gotz, and M. R. Krames, Appl. Phys. Lett., **91** (2007).
[39] G. Chen, G. Craven, A. Kim, A. Munkholm, S. Watanabe, A. Camras, W. Gotz, and F. Steranka, Phys. Status Solidi A, **2005**, 1086 (2009).
[40] M. H. Kim, M. F. Schubert, Q. Dai, J. K. Kim, E. F. Schubert, J. Piprek, and Y. Park, Appl. Phys. Lett., **91** (2007).
[41] K. J. Vampola, M. Iza, S. Keller, S. P. DenBaars, and S. Nakamura, Appl. Phys. Lett., **94** (2009).
[42] B. Monemar and B. E. Sernelius, Appl. Phys. Lett., **91** (2007).
[43] Y. Yang, X. A. Cao, and C. H. Yan, Ieee Transactions on Electron Devices, **55**, 1771 (2008).
[44] K. A. Bulashevich and K. S. Y., Phys. Status Solidi C, **5**, 2066 (2008).
[45] P. J. Dean, E. C. Lightowlers, and D. R. Wight, Phys. Rev., **140**, A352 (1965).
[46] A. T. Collins, M. Kamo, and Y. Sato, Condens. Matter, **1**, 4029 (1989).
[47] H. Watanabe, K. Hayashi, D. Takeuchi, S. Yamanaka, H. Okushi, and K. Kajimura, Appl. Phys. Lett., **73**, 981 (1998).
[48] J. Hammersberg, J. Isberg, E. Johansson, T. Lundstrom, O. Hjortstam, and H. Bernhoff, Diamond Relat. Mater., **10**, 574 (2001).
[49] S. Salvatori, M. C. Rossi, and F. GAlluzzi, Carbon, **37**, 811 (1999).
[50] A. Fujii, K. Takiyama, R. Maki, and T. Fujita, Journal of Luminescence, **94**, 355 (2001).
[51] M. Chiorboli, M. G. Donato, G. Faggio, M. Marinelli, G. Messina, E. Milani, R. Potenza, S. Santangelo, M. Scoccia, C. Tuve, and G. V. Rinati, Diamond Relat. Mater., **15**, 1976 (2006).
[52] Y. Oshiki, J. H. Kaneko, F. Fujita, A. Homma, H. Watanabe, K. Meguro, Y. Yamamoto, T. Imai, K. Sato, K. Tsuji, S. Kawamura, and M. Furusaka, Diamond Relat. Mater., **17**, 833 (2008).
[53] H. J. Eichler, P. Gunter, and D. W. Pohl, (Springer, Berlin, 1986).
[54] K. Jarašiūnas and J. Vaitkus, Phys. Stat. Sol., **44**, 793 (1977).
[55] K. Jarašiūnas and H. J. Gerritsen, Appl. Phys. Lett., **33**, 190 (1978).
[56] O. W. Kading, H. Skurk, A. A. Maznev, and E. Matthias, Applied Physics a-Materials Science & Processing, **61**, 253 (1995).
[57] H. J. Eichler and H. Stahl, Opt. Commun., **6**, 239 (1972).
[58] R. C. Lind, D. G. Steel, M. B. Klein, R. L. Abrams, C. R. Giuliano, and R. K. Jain, Appl. Phys. Lett., **34**, 147 (1979).
[59] M. D. Fayer, IEEE J. Quantum Electron., **QW-22**, 1437 (1986).
[60] P. Hess, Phys. Today, **55**, 42 (2002).
[61] T. A. Rogers, A. A. Maznev, M. J. Banet, and K. A. Nelson, Annu. Rev. Mater. Sci., **30**, 117 (2000).
[62] B. V. Zeghbroeck, *Principles of semiconductor devices*, 2004).
[63] P. Grivickas, (KTH, Stochholm, 2004), Vol. PhD thesis.
[64] H. J. Eichler and F. Massman, J. Appl. Phys., **53**, 3237 (1982).

[65] A. A. Maznev, K. A. Nelson, and T. A. Rogers, Optics Letters, **23**, 1319 (1998).
[66] K. Jarašiūnas, R. Aleksiejūnas, T. Malinauskas, V. Gudelis, T. Tamulevicius, S. Tamulevicius, A. Guobiene, A. Usikov, V. Dmitriev, and H. J. Gerritsen, Rev. Sci. Instrum., **78** (2007).
[67] V. G. Ralchenko, A. A. Smolin, V. I. Konov, K. F. Sergeichev, I. A. Sychov, I. I. Vlasov, V. V. Migulin, S. V. Voronina, and A. V. Khomich, Diamond Relat. Mater., **6**, 417 (1997).
[68] T. Malinauskas, K. Jarašiūnas, E. Ivakin, V. Ralchenko, A. Gontar, and S. Ivakhnenko, Diamond Relat. Mater., **17**, 1212 (2008).
[69] T. Wang, T. Shirahama, H. B. Sun, H. X. Wang, J. Bai, S. Sakai, and H. Misawa, Appl. Phys. Lett., **76**, 2220 (2000).
[70] S. Haffouz, B. Beaumont, P. Vennegues, and P. Gibart, Phys. Status Solidi A, **176**, 677 (1999).
[71] P. Vennegues, B. Beaumont, S. Haffouz, M. Vaille, and P. Gibart, J. Cryst. Growth, **187**, 167 (1998).
[72] H. Lahreche, P. Vennegues, B. Beaumont, and P. Gibart, J. Cryst. Growth, **205**, 245 (1999).
[73] G. P. Yablonskii, A. L. Gurskii, V. N. Pavlovskii, E. V. Lutsenko, V. Z. Zubialevich, T. S. Shulga, A. I. Stognij, H. Kalisch, A. Szymakowski, R. H. Jansen, A. Alam, B. Schineller, and M. Heuken, J. Cryst. Growth, **275**, e1733 (2005).
[74] A. Kakanakova-Georgieva, U. Forsberg, C. Hallin, P. O. A. Persson, L. Storasta, G. Pozina, J. Birch, L. Hultman, and E. Janzen, Silicon Carbide and Related Materials - 2002, **433-4**, 991 (2002).
[75] A. L. Gurskii, in *NATO Science Series II*, edited by M. S. Shur and A. Žukauskas (Kluwer Acad. Publ., 2004), Vol. 144, p. 199.
[76] R. Aleksiejūnas, M. Sudzius, T. Malinauskas, J. Vaitkus, K. Jarašiūnas, and S. Sakai, Appl. Phys. Lett., **83**, 1157 (2003).
[77] G. Tamulaitis, J. Mickevicius, M. S. Shur, Q. Fareed, J. Zhang, and R. Gaska, Phys. Status Solidi C, **3**, 1923 (2006).
[78] E. V. Lutsenko, A. L. Gurskii, V. N. Pavlovskii, G. P. Yablonskii, T. Malinauskas, K. Jarašiūnas, B. Schineller, and M. Heuken, Physica Status Solidi C - Current Topics in Solid State Physics, Vol 3, No 6, **3**, 1935 (2006).
[79] K. Jarašiūnas, T. Malinauskas, A. Kadys, R. Aleksiejūnas, M. Sudzius, S. Miasojedovas, S. Juršėnas, A. Žukauskas, D. Gogova, A. Kakanakova-Georgieva, E. Janzen, H. Larsson, B. Monemar, P. Gibart, and B. Beaumont, Phys. Status Solidi C, **2**, 1006 (2005).
[80] D. Gogova, A. Kasic, H. Larsson, C. Hemmingsson, B. Monemar, F. Tuomisto, K. Saarinen, L. Dobos, B. Pecz, P. Gibart, and B. Beaumont, J. Appl. Phys., **96**, 799 (2004).
[81] B. Beaumont, J. P. Faurie, E. Aujol, and P. Gibart, in *Proc. NATO ARW on UV solid state light emitters and devices*, edited by M. S. Shur and A. Žukauskas (Kluwer Acad. Publ., 2004), Vol. 144, p. 189.
[82] A. Dmitriev and A. Oruzheinikov, J. Appl. Phys., **86**, 3241 (1999).

[83] S. M. Sze, *Physics of Semiconductor Devices* (A Wiley-Interscience publication, 1981).
[84] C. A. Hoffman, K. Jarašiūnas, H. J. Gerritsen, and A. V. Nurmikko, Appl. Phys. Lett., **33**, 536 (1978).
[85] O. Brandt, H. J. Wunsche, H. Yang, R. Klann, J. R. Mullhauser, and K. H. Ploog, J. Cryst. Growth, **190**, 790 (1998).
[86] J. S. Im, A. Moritz, F. Steuber, V. Harle, F. Scholz, and A. Hangleiter, Appl. Phys. Lett., **70**, 631 (1997).
[87] T. Malinauskas, R. Aleksiejūnas, K. Jarašiūnas, B. Beaumont, P. Gibart, A. Kakanakova-Georgieva, E. Janzen, D. Gogova, B. Monemar, and M. Heuken, J. Cryst. Growth, **300**, 223 (2007).
[88] K. Jarašiūnas, T. Malinauskas, R. Aleksiejūnas, M. Sudzius, E. Frayssinet, B. Beaumont, J. P. Faurie, and P. Gibart, Phys. Status Solidi A, **202**, 566 (2005).
[89] T. Malinauskas, K. Jarašiūnas, R. Aleksiejūnas, D. Gogova, B. Monemar, B. Beaumont, and P. Gibart, Phys. Status Solidi B, **243**, 1426 (2006).
[90] R. Ziebold, T. Witte, M. Hubner, and R. G. Ulbrich, Phys. Rev. B, **61**, 16610 (2000).
[91] P. Bruckner, F. Habel, and F. Scholz, Phys. Status Solidi C, **3**, 1471 (2006).
[92] H. M. Driel, Phys. Rev. B, **35**, 8166 (1987).
[93] H. M. Ng, D. Doppalapudi, T. D. Moustakas, N. G. Weimann, and L. F. Eastman, Appl. Phys. Lett., **73**, 821 (1998).
[94] B. Gil, *Group III Nitride Semiconductor compounds: Physics and Applications* (Oxford Univ. Press, 1998).
[95] S. Juršėnas, N. Kurilcik, G. Kurilcik, A. Žukauskas, P. Prystawko, M. Leszcynski, T. Suski, P. Perlin, I. Grzegory, and S. Porowski, Appl. Phys. Lett., **78**, 3776 (2001).
[96] S. Juršėnas, S. Miasojedovas, G. Kurilcik, A. Žukauskas, and P. R. Hageman, Appl. Phys. Lett., **83**, 66 (2003).
[97] U. Ozgur, Y. Fu, Y. T. Moon, F. Yun, H. Morkoc, and H. O. Everitt, J. Appl. Phys., **97** (2005).
[98] R. Aleksiejūnas, M. Sudzius, V. Gudelis, T. Malinauskas, K. Jarašiūnas, Q. Fareed, R. Gaska, M. S. Shur, J. Zhang, J. Yang, E. Kuokstis, and M. A. Khan, 5Th International Conference on Nitride Semiconductors (Icns-5), Proceedings, 2686 (2003).
[99] K. Kazlauskas, (Vilnius University, Vilnius, 2004), Vol. PhD thesis.
[100] S. F. Chichibu, T. Azuhata, T. Sota, T. Mukai, and S. Nakamura, J. Appl. Phys., **88**, 5153 (2000).
[101] M.-Y. Ryu, E. Kuokstis, C. Q. Chen, J. W. Yang, G. Simin, M. Asif Khan, G. G. Sim, and P. W. Yu, Solid State Communications, **126**, 329 (2003).
[102] F. A. Ponce, S. Srinivasan, A. Bell, L. Geng, R. Liu, M. Stevens, J. Cai, H. Omiya, H. Marui, and S. Tanaka, Phys. Status Solidi B, **240**, 273 (2003).

[103] K. Jarašiūnas, R. Aleksiejūnas, T. Malinauskas, M. Sudzius, S. Miasojedovas, S. Juršėnas, A. Žukauskas, R. Gaska, J. Zhang, M. S. Shur, J. W. Yang, E. Kuokstis, and M. A. Khan, Physica Status Solidi a-Applications and Materials Science, **202**, 820 (2005).
[104] S. Bidnyk, T. J. Schmidt, Y. H. Cho, G. H. Gainer, J. J. Song, S. Keller, U. K. Mishra, and S. P. DenBaars, Appl. Phys. Lett., **72**, 1623 (1998).
[105] I. P. Marko, E. V. Lutsenko, V. N. Pavlovskii, G. P. Yablonskii, O. Schon, H. Protzmann, M. Lunenburger, M. Heuken, B. Schineller, and K. Heime, Physica Status Solidi B-Basic Research, **216**, 491 (1999).
[106] M. Nomura, M. Arita, Y. Arakawa, S. Ashihara, S. Kako, M. Nishioka, T. Shimura, and K. Kuroda, J. Appl. Phys., **94**, 6468 (2003).
[107] U. Ozgur, H. O. Everitt, S. Keller, and S. P. DenBaars, Appl. Phys. Lett., **82**, 1416 (2003).
[108] T. Wang, P. J. Parbrook, M. A. Whitehead, W. H. Fan, and A. M. Fox, J. Cryst. Growth, **273**, 48 (2004).
[109] W. X. Zou, J. L. Merz, and L. A. Coldren, J. Appl. Phys., **72**, 5047 (1992).
[110] I. Kiflawi and J. Bruley, Diamond Relat. Mater., **9**, 87 (2000).
[111] C. E. Nebel, Semiconductor Science and Technology, **18**, S1 (2003).
[112] J. Isberg, J. Hammersberg, E. Johansson, T. Wikstrom, D. J. Twitchen, A. J. Whitehead, S. E. Coe, and G. A. Scarsbrook, Science, **297**, 1670 (2002).
[113] S. V. Garnov, A. I. Ritus, S. M. Klimentov, S. M. Pimenov, V. I. Konov, S. Gloor, W. Luthy, and H. P. Weber, Appl. Phys. Lett., **74**, 1731 (1999).
[114] N. V. Novikov, T. A. Nachalna, S. Ivakhnenko, O. A. Zanevsky, I. S. Belousov, V. G. Malogolovets, G. A. Podzyarei, and L. A. Romanko, Diamond Relat. Mater., **12**, 1990 (2003).
[115] J. Isberg, J. Hammersberg, D. J. Twitchen, and A. Whitehead, Diamond Relat. Mater., **13**, 320 (2004).
[116] Y. Oshiki, J. H. Kaneko, F. Fujita, K. Hayashi, K. Meguro, A. Homma, S. Kawamura, Y. Yokota, Y. Yamamoto, K. Kobashi, T. Imai, T. Sawamura, and M. Furusaka, Diamond Relat. Mater., **15**, 1508 (2006).
[117] B. Marczewska, I. Kupriyanov, Y. Pal'yanov, T. Nowak, P. Olko, M. Rebisz, and M. P. R. Waligorski, Diamond Relat. Mater., **16**, 191 (2007).
[118] W. Deferme, G. Tanasa, J. Amir, K. Haenen, M. Nesladek, and C. F. J. Flipse, Diamond Relat. Mater., **15**, 687 (2006).